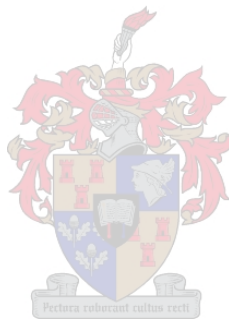


Experimental Investigation of a Gimbal in the Frequency Domain

by
Michen Christian Haller

*Thesis presented in partial fulfilment of the requirements for the degree
of Master of Engineering (Mechatronic) in the Faculty of Engineering at
Stellenbosch University*



Supervisor: Dr. Willie Smit
Co-supervisor: Dr. Annie Bekker

April 2019

DECLARATION

By Submitting this thesis electronically, I declare that the entirety of the work contained therein is my own, that I am the sole author thereof (save to the extent explicitly otherwise stated), that reproduction and publication thereof by Stellenbosch University will not infringe any third party rights and that I have not previously in its entirety or in part submitted it for obtaining any qualification.

April 2019

Copyright © 2019 Stellenbosch University

All rights reserved

Abstract

When it comes to renewable energies, the reduction of initial investment costs help make these generation methods a more viable option for governments, or private companies. For Concentrated Solar Power (CSP) plants, a particular example of this would be the initial investment costs associated with the heliostats. Heliostat foundation preparation and heliostat structure quality need to be of a high standard for a heliostat to remain within its calibration parameters for long periods of time. If calibrations, inspections and cleaning of these heliostats can be done more regularly, the time for which the heliostat needs to maintain its calibration parameters is reduced, thereby reducing foundation preparation costs and heliostat manufacturing costs.

At the University of Stellenbosch, the Solar Thermal Energy Research Group (STERG) is investigating the use of automated drones to perform inspections, calibrations and cleaning of heliostats. In order to attach sensors to the drone, a gimbal is used. This isolates the sensor from the drone's rotations. Gimbal dynamic performance data, which is relevant to design engineers, is not readily available. In this thesis, the pitch responses of a two-axis gimbal to pitch and roll disturbances are measured for varying disturbance frequencies and amplitudes, without vibration isolation pads.

In addition to producing the gimbal performance data, it is found that the largest gains observed occurred in region where no structural natural frequencies were found. It is suspected that the knocking of the gimbal Inertial Measurement Unit (IMU) cable, which is connected to the device-mount IMU, is the source of these peak responses. The responses to pitch and roll actuations differed significantly, with the largest reponse attenuation observed for pitch actuations between 31 Hz and 46 Hz. It is also found that the gimbal is sensitive to frame vibrations, especially at frame natural frequencies, which highlights the need for vibration isolation pads during use. It is recommended that further research be conducted in the frequency domain for roll and yaw responses. In addition, it is recommended that the efficacy of gimbal vibration isolation pads, for blade pass frequencies, be investigated. Lastly, it is recommended that a more detailed analysis of the gain attenuation observed for the responses to pitch actuations, be conducted.

Uittreksel

In die hernubare energie bedryf, help die vermindering van aanvanklike beleggingskoste om hernubare kragvoorsieningsmetodes 'n lewensvatbare opsie te maak vir regerings en privaatmaatskappye. Wat betref gekonsentreerde-sonkragaanlegte, is 'n spesifieke voorbeeld hiervan die aanvanklike beleggingskoste van heliostate. Die voorbereiding van die fondamente van heliostate en heliostaatstrukture moet van 'n hoë standaard wees, ten einde te verseker dat die heliostaat vir lang tye binne die gekalibreerde parameters sal bly. Indien die kalibrering, die inspeksie en die skoonmaak van hierdie heliostate meer gereeld gedoen kan word, sal dit die tydsduur verminder waar die heliostaat binne sy gekalibreerdeparameters moet bly, asook die koste verbonde aan die voorbereiding van fondamente en vervaardiging van heliostate.

By die Universiteit van Stellenbosch ondersoek die Sontermiese-energieonavorsingsgroep (STERG) die gebruik van selfaangedrewe hommeltuie om die inspeksies, kalibrerings en skoonmaak van die heliostate uit te voer. Ten einde sensors aan die hommeltuig te kan vasheg, word 'n kompasbeuel (gimbal) gebruik. Die kompasbeuel isoleer die hommeltuig se bewegings van die sensor. Volledige inligting oor die werksverrigting van die kompasbeuel, wat relevant is vir ontwerpingenieurs, is nie gereedelik beskikbaar nie. In hierdie tesis word 'n tweemas-kompasbeuel, sonder vibrasie-isoleringskussinkies, se responsie met betrekking tot helling- en rolversteurings gemeet vir verskillende versteuringsfrekwensies en -amplitudes.

Bykomend tot die verskaffing van die gimbal-prestasiedata, is daar gevind dat die grootste aanwinste wat waargeneem kon word, plaasgevind het waar geen strukturele natuurlike frekwensies was nie. Daar word vermoed dat die beweging van die gimbal se traagheidsmeterkabel (Inertial Measurement Unit - IMU), wat gekoppel is aan die toestelraam (device-mount IMU), die bron van hierdie piek gedrag was. Die responsies op helling- en rolversteurings het aansienlik verskil, met die grootste attenuasie in die responsie op hellingsteuring tussen 31 Hz en 46 Hz. Daar is ook bevind dat die kompasbeuel sensitief is vir vibrasies in die raamwerk, veral by natuurlike frekwensies van die raamwerk. Dit toon duidelik die behoefte aan vibrasie-isoleringskussinkies. Daar word aanbeveel dat verdere frekwensiedomeinmetings gedoen behoort te word op rol- en gierresponsies. Daar word verder aanbeveel dat die doeltreffendheid van die kompasbeuelvibrasie-isoleringskussinkies in die besonder ook vir frekwensies, veroorsaak deur lemrotering, ondersoek moet word. Laastens word aanbeveel dat 'n meer gedetailleerde analise van die aanwinstenuasie, waargeneem by die responsies op hellingsteurings, uitgevoer behoort te word.

Acknowledgements

I would like to thank my parents, brother and girlfriend for their love, support and encouragement, without whom this project and its completion would not have been possible.

I would like to thank Dr. Smit for giving me the opportunity to do my masters with him, for his thought provoking advice, for the time that he always made available and his patience.

I would like to thank Dr. Bekker for her advice, insight and keen interest she brought to the project.

I would also like to thank Jurgens Gouws, Dr. Hannes Swart, Brendon Nickerson, Nicholas J. Minnaar, Prof. Kristiaan Schreve and Dr. Danie Els for the discussions and debates over the results, which were invaluable in overcoming the many challenges faced in this project.

Lastly, I would like to thank the technical staff of the Mechanical and Mechatronic department for their patience and eagerness whenever advice, or help, was needed.

Table of Contents

1	Introduction.....	1
1.1	Background.....	1
1.2	Thesis Objectives	5
1.3	Investigation Plan.....	5
1.4	Thesis Outline.....	5
2	Literature Review	6
2.1	Two Axis Motorised Gimbals.....	6
2.2	Brushless Direct Current Motors and Sub-pole Accuracy	7
2.3	Camera Calibration	8
2.4	Subpixel Point Triangulation.....	11
2.5	The Fourier Transform	12
2.6	Frequency Domain Performance Measurements.....	14
2.7	Monte Carlo Simulations.....	17
2.8	Measurement Uncertainty Propagation and Determination	18
3	Gimbal Base Actuation.....	23
3.1	Drone Hover Performance.....	23
3.2	Gimbal Base Actuation System	25
4	Measurement System.....	28
4.1	Measurement Systems and Devices Considered.....	28
4.2	Linear System Assumption.....	31
4.3	Measuring the Gimbal Base Actuation	31
4.4	Measuring Gimbal Device Mount Responses	32
4.5	Laser Dot Displacement Measurement	38
4.6	Achievable Camera Angular Resolution.....	42
4.7	Laser Dot Displacement Tracking Verification Experiments	43
4.8	Final Measurement Processing and Uncertainty.....	48
5	Preliminary Tests.....	50
5.1	Determination of Support Frame Natural Frequencies	50
5.2	Unwanted Support Frame Displacement.....	53
5.3	Actuation Plate Yawing.....	56

5.4	Gimbal Response Tests	57
5.4.1	Assumptions.....	57
5.4.2	Expected Results	58
5.4.3	Experiment Setups and Procedure	58
5.4.4	Pitch Actuation Gimbal Response Results and Discussions	61
5.4.5	Roll Actuation Gimbal Response Results and Discussions.....	63
5.5	Preliminary Tests Summation.....	64
6	Final Experiments.....	66
6.1	Assumptions, Expected Results and Experimental Procedure	66
6.2	Experiment Observations for Pitch Actuators	66
6.3	Experiment Observations for Roll Actuators.....	67
6.4	Pitch Actuation Results and Discussions	68
6.4.1	The Gain Resonances at the System Natural Frequencies	69
6.4.2	The 32.0 Hz Resonance and the Gain Increase towards 60.0 Hz ..	70
6.4.3	The 11.0 Hz to 17.0 Hz Gain Attenuation.....	70
6.4.4	The 32.0 Hz to 49.0 Hz Gain Attenuation.....	72
6.4.5	Gain Sample Calculation.....	73
6.5	Roll Actuation Results and Discussions.....	77
7	Conclusions and Recommendations.....	80
A.	Drawings and Dimensions	A.1
B.	Tracking Algorithm Verification Setup Parameters.....	B.1
B.1	Camera Calibration Pattern.....	B.1
B.2	Verification Test Plan.....	B.2
B.3	Camera Setup for Verification Tests.....	B.3
B.4	Accelerometer Sensitivities	B.4
C.	Initial Camera Position for Angular Resolution.....	C.1
D.	Gimbal Actuation and Gimbal Response Tracking Error and Uncertainty Analyses.....	D.1
D.1	Actuation System Error Sources and Resulting Uncertainty Contributions.....	D.1
D.1.1	Displacement Profile Assumption.....	D.2

D.1.2	New Camera Position Error.....	D.3
D.1.3	Reference Laser Bore Sight Error	D.4
D.1.4	Support Frame Constant Pitch Error	D.6
D.1.5	Support Frame and Actuation Plate Constant Roll Error	D.7
D.1.6	Support Frame Constant Yaw Error and Reference Laser Distance to Target Error	D.8
D.1.7	Actuation Uncertainty Summation.....	D.9
D.2	Gimbal System Error Sources and Resulting Uncertainty Contributions.....	D.10
D.2.1	Displacement Profile Assumption.....	D.10
D.2.2	New Camera Position Error.....	D.11
D.2.3	Gimbal Laser Bore Sight Error	D.12
D.2.4	Camera Synchronization.....	D.13
D.2.5	Response Uncertainty Summation	D.14
D.3	Monte Carlo Error Simulations Analysis	D.14
E.	Support Structure Natural Frequency Tests	E.1
F.	Gimbal Pitch Response Gain Plots for Pitch Actuations.....	F.1
G.	Gimbal Pitch Response Gain Plots for Roll Actuations	G.1
8	References.....	122

Figure 1. The Solucar PS10 solar power plant in Spain..... 1

Figure 2. Drone and mounted two-axis motorised gimbal (Left). A close-up of a two-axis motorised gimbal with a mounted camera (Right). 3

Figure 3. A box model of the drone and gimbal, showing the drone and gimbal axis systems, where the positive x-axis direction points toward the front of the drone (Left).. 3

Figure 4. An example of a two-axis gimbal..... 7

Figure 5. An example of a six-stator pole, two-rotor pole brushless direct current (BLDC) motor (Texas Instruments, 2013). 7

Figure 6. The pinhole camera model (MathWorks, 2016) 9

Figure 7. Camera calibration board origin after being processed by the Matlab camera calibrator application..... 9

Figure 8. Two examples of radial lens distortion.....10

Figure 9. Tangential distortion example showing what lens/sensor misalignment causes tangential distortion (MathWorks, 2018).10

Figure 10. The undistorting of the datum photo of the calibration board11

Figure 11. The Hanning window and the respective scaling factors for each sample in a data set.....13

Figure 12. An example of the effect of a Hanning window of a 1 Hz data set.....14

Figure 13. The FFT of the drone's pitch angle during a hover test.24

Figure 14. The zoomed FFT of the drones pitch angle during hover.....24

Figure 15. A Photograph of the current IMP 2-Axis BLDC gimbal supplied by RC Timer (RC Timer, 2017).....26

Figure 16. A box and line diagram of the actuation plate and shaker. Together, these two components would actuate the gimbal.....26

Figure 17. Main support stand, support frame, shaker and actuation plate.....27

Figure 18. The reference laser in a clasp.29

Figure 19. Side photograph of the reference laser in its clamp29

Figure 20. A Positon Sensitive Photodiode.30

Figure 21. The 5mW, class 3a laser that was mounted to the gimbal device mount.30

Figure 22. A box and line example of the gimbal base actuation system.32

Figure 23. Device mount laser holder.33

Figure 24. An example of ideal gimbal operation when swung forward..34

Figure 25. An example of ideal gimbal operation when swung backward.	34
Figure 26. An example of a non-ideal operation scenario of the gimbal forward swing.....	35
Figure 27. An example of a non-ideal operation scenario of the gimbal backswing.	35
Figure 28. An example of a peak-to-peak gimbal base rotation,	37
Figure 29. The expected reference laser and gimbal laser dot displacement vs time.....	38
Figure 30. The defocused FP-LR-635-1-C-F laser dot.	39
Figure 31. An example of the process of trying to find the same position in the defocused reference laser between two different positions	40
Figure 32. Laser dot centroid tracking simulations on a Gaussian simulated dot with normally distributed, but varying image pixel intensity.....	41
Figure 33. An example of the process used in finding an initial guess at the focused laser centroid using the Matlab functions "regionprops" and "imfindcircles".	42
Figure 34. An example of the correlation between the angular subpixel resolution and the image subpixel resolution.....	43
Figure 35. The laser dot tracking accuracy verification experiment setup for the 2000fps tests.....	44
Figure 36. An example of the grouping of the smaller laser dot displacement steps.	45
Figure 37. 2000fps, 1280 pixel algorithm accuracy verification test example data for the x-axis displacements.	46
Figure 38. Accelerometers 1, 2 and 3 mounted to the upper beam.....	50
Figure 39. Accelerometers 5 and 6 mounted to the actuation plate	51
Figure 40. The FRF of the first modal hammer tests..	52
Figure 41. The FRF of the first modal hammer test.....	52
Figure 42. An example of the displacement of the upper beam of the support frame.....	54
Figure 43. The magnetically attached Inductive Displacement Transducer (IDT).....	55
Figure 44. The reference laser dot x-axis co-ordinate vs. time.....	56
Figure 45. The gimbal, the gimbal frame, the gimbal base, the gimbal motor and the actuation plate.	57

Figure 46. The monitoring camera for the gimbal laser, with the gimbal laser target surface in the foreground.	59
Figure 47. The monitoring camera for the reference laser, with the reference laser target surface.	60
Figure 48. Gimbal laser-monitoring camera with the gimbal laser target surface on the right of the image.	60
Figure 49. The gimbal's pitch response gain plot for pitch actuations.	61
Figure 50. The gimbal pitch response to pitch actuations at 17.5 Hz.	62
Figure 51. An example of the gimbal losing control for the largest roll actuations at 40.0 Hz.	63
Figure 52. The gimbal's pitch response gain plot for the smallest and largest roll actuations.	64
Figure 53. The gimbal and device mount, with the loose grub screw on the pitch motor shaft.	65
Figure 54. The gimbal response gains to the three different pitch actuation sizes.	68
Figure 55. The gimbal response gains to the three different pitch actuation sizes with uncertainty bounds.	69
Figure 56. A time domain example of the gimbal's responses to the largest pitch inputs versus time at 13.0 Hz.	71
Figure 57. A time domain example of the gimbal's responses to the largest pitch inputs versus time at 35.0 Hz.	72
Figure 58. The gimbal response gain, input and outputs versus frequency, for the largest pitch actuations.	73
Figure 59. The absolute gimbal response to the largest absolute disturbance at 32 Hz.	74
Figure 60. The gimbal response gains to the three different roll actuation sizes.	78
Figure 61. The gimbal response gains to the three different roll actuation sizes with uncertainty bounds.	79
Figure 62. Actuation plate dimensions and material.	A.1
Figure 63. Actuation plate bush dimensions and material.	A.2
Figure 64. Gimbal attaching block dimensions and material.	A.3
Figure 65. Reference-laser-clamp dimensions and material.	A.4
Figure 66. Actuation assembly.	A.5
Figure 67. Gimbal laser clamp dimensions and material.	A.6

Figure 68. Calibration board pattern. B.1

Figure 69. The camera Field of View (FOV) C.1

Figure 70. The theoretical camera sub-pixel angular resolution for the image
y-axis at 2000fps. C.4

Figure 71. The theoretical camera sub-pixel angular resolution for the image
y-axis at 10 000fps. C.4

Figure 72. An example of an angled camera pixel distribution. C.5

Figure 73. The error flowchart for the reference laser. D.2

Figure 74. An example of laser bore sight error. D.5

Figure 75. An example of the equilibrium error introduced to the reference
laser displacement, if the support frame has a pitch pose error. D.6

Figure 76. An example of a negative support frame roll offset angle. D.8

Figure 77. The error flowchart for the gimbal laser. D.10

Figure 78. An example of the effect of the gimbal laser bore sight error, in
combination with device mount roll. D.12

Figure 79. Histogram of the difference between the measured and true
actuation angle from the Monte Carlo simulations for pitch actuations. D.15

Figure 80. Histogram of the difference between the measured and true
gimbal response angle from the Monte Carlo simulations for pitch
actuations. D.16

Figure 81. The FRF of the upper beam of the support frame for the second
modal hammer test. E.1

Figure 82. The FRF for the actuation plate for the second modal hammer test. . E.1

Figure 83. The power spectral density over time for accelerometer 5 on the
actuator plate. E.2

Figure 84. The power spectral density over time for accelerometer 2 on the
actuator plate. E.2

Figure 85. The acceleration vs time plots of accelerometers 4, 5 and 6. E.3

Figure 86. The zoomed acceleration vs time plots of accelerometers 4, 5 and 6. E.3

Figure 87. The response gain, with corresponding uncertainties, for the
smallest pitch actuations. F.1

Figure 88. The response gain, with corresponding uncertainties, for the middle
pitch actuations. F.1

Figure 89. The response gain, with corresponding uncertainties, for the largest
pitch actuations. F.2

Figure 90. The response gain, with corresponding uncertainties, for the smallest roll actuations.G.1

Figure 91. The response gain, with corresponding uncertainties, for the middle roll actuations.G.1

Figure 92. The response gain, with corresponding uncertainties, for the largest roll actuations.G.2

Table 1. Algorithm accuracy verification test results	47
Table 2. The results of the two modal hammer tests on the upper beam of the support frame..	53
Table 3. The results of the two modal hammer tests on the actuation plate.....	53
Table 4. The gimbal gain resonances and corresponding support structure and actuation plate natural frequencies for pitch actuations.	70
Table 5. The gimbal gain resonances and corresponding support structure and actuation plate natural frequencies for roll actuations.....	79
Table 6. Laser dot tracking algorithm accuracy verification test plan.....	B.2
Table 7. Laser dot tracking algorithm accuracy verification test system setup parameters.....	B.3
Table 8. Support frame and actuation plate mounted accelerometers' sensitivities.....	B.4
Table 9. Monte Carlo input variable ranges 1	D.17
Table 10. Monte Carlo input variable ranges 2.....	D.18

Nomenclature

Acronyms

BLDC	Brushless Direct Current
CSP	Concentrated Solar Power
CCW	Counter Clockwise
CW	Clockwise
DAQ	Data Acquisition
DFT	Discrete Fourier Transform
FFT	Fast Fourier Transform
FOV	Field of View
FPS	Frames per Second
FRF	Frequency Response Function
FT	Fourier Transform
IDT	Inductive Displacement Transducer
IFT	Inverse Fourier Transform
IMU	Inertial Measurement Unit
LT	Laplace Transform
PSD	Position Sensitive Photodiode
RSS	Root Sum Squares
SISO	Single Input Single Output
STERG	Solar Thermal Energy Research Group
TTL	Transistor-Transistor Logic
UAV	Unmanned Aerial Vehicle

Variables

A	Plant Output Signal Amplitude ... []
A_{Value}	First Measured Value..... []
B	Controller Output Signal Amplitude []
$b_{inc.}$	Inclinometer Correlated Systematic Standard Deviation ... [deg]
$B_{measurement}$	Systematic Uncertainty []
B_{Value}	Second Measured Value []
b_R	Result Systematic Standard Deviation..... []
$b_{\overline{Reference_Camera_Distance}}$	Systematic Standard Deviation of Reference Laser Camera Distance to Target Error [deg]
$b_{\overline{Response_Camera_Distance}}$	Systematic Standard Deviation of Gimbal Laser Camera Distance to Target Error [deg]
b_{r_f}	Systematic Standard Deviation of Range Finder Measurement Errors [mm]
$b_{Reference_Reprojection}$	Systematic Uncertainty for New Reference Laser Camera Position [deg]
$b_{Response_Reprojection}$	Systematic Uncertainty of Gimbal Laser Camera Distance to Target Error..... [deg]
$b_{\bar{x}}$	Systematic Uncertainty of a Measurement..... []
C	Coherence []
$D_{Camera_@fps}$	Distance of Camera to Target Surface [mm]

$D_{\text{Camera_@ 10 000fps}}$	Distance of Camera Monitoring Reference Laser to Reference Laser Target Surface..... [mm]
$D_{\text{Camera_@ 2000fps}}$	Distance of Camera Monitoring Gimbal Laser to Gimbal Laser Target Surface [mm]
D_{Gimbal}	Distance from Centre of Rotation of Gimbal Laser to the Gimbal Laser Target Surface..... [mm]
D_{laser}	Distance of Given Laser Centre of Rotation to Corresponding Laser Target Surface [mm]
$D_{\text{Reference}}$	Distance from the Centre of Rotation of the Reference Laser to the Reference Laser Target Surface [mm]
$d_{\text{diff_gimbal}}$	Mean Algorithm Gimbal Laser Displacement Difference [mm]
$d_{\text{diff_ref}}$	Mean Algorithm Reference Laser Displacement Difference [mm]
d_{gimbal}	Gimbal Vertical Displacement.... [mm]
d_{Observed}	Observed Laser Dot Displacement..... [mm]
$d_{\text{Reference_Observed}}$	Observed Reference Laser Dot Displacement..... [mm]
f	Frequency..... [Hz]
G	Gain []
H	Field of View Diagonal Distance [pixels]
H	Number of Correlated Errors []

h	Current Error []
$I_{\text{Intensity}}$	Pixel Intensity Value []
$Image_Res$	Image Resolution at Pixel Level . [pixels/mm]
$Image_Res_{\text{sub-pixel@fps}}$	Sub-pixel Image Resolution at Specific Frame Rate..... [mm]
K_b	Number of Independent Systematic Standard Deviations.. []
K_s	Number of Independent Random Sample Standard Deviations []
K_{sb}	Largest Number Between K_s and K_b []
K_u	Number of Independent Uncertainties []
k	Current Uncertainty Number []
L	Distance to Gimbal Centre of Gravity [mm]
$L_{\text{variables}}$	Number of Independent Variables []
M	Plant Signal Gain..... []
N	Number of Measurements..... []
$No\#. \text{Pixels}$	Number of Image Axis Pixels..... [pixels]
$No\#. X - \text{Axis Pixels}$	Number of Image X-Axis Pixels. [pixels]
$No\#. Y - \text{Axis Pixels}$	Number of Image Y-Axis Pixels. [pixels]
n	Power Multiplied with Relative Uncertainty..... []
$n_{\text{measurement points}}$	Number of Measurement Points for a Given Response Gain Definition []
n_{samples}	Number of Test Samples..... []

P	Probability..... [%]
$P_{\text{Gimbal_Back}}$	Position of Gimbal Laser Dot for Gimbal Back Swing [mm]
$P_{\text{Gimbal_Forward}}$	Position of Gimbal Laser Dot for Gimbal Forward Swing [mm]
$P_{\text{Gimbal_Max}}$	Peak Position of Gimbal Laser Dot [mm]
$P_{\text{Gimbal_Mean}}$	Average Position of Gimbal Laser Dot..... [mm]
$P_{\text{Reference_Max}}$	Peak Position of Reference Laser Dot [mm]
$P_{\text{Reference_Mean}}$	Average Position of Reference Laser Dot..... [mm]
$Q(\omega)$	Complex Frequency Response Function []
R_x	Output Autocorrelation Function []
R_{xf}	Output Cross-Correlation Function []
S_f	Input Spectral Density []
S_R	Result Sample Standard Deviation..... []
$\overline{S_{\text{Reference_Assumption}}}$	Reference Laser Dot Displacement Profile Assumption Sample Standard Deviation..... [mm]
$S_{\text{Reference_Bore_Sight}}$	Bore Sight Error Sample Standard Deviation [deg]
$\overline{S_{\text{Response_Assumption}}}$	Gimbal Laser dot Displacement Profile Assumption Sample Standard Deviation..... [mm]

$S_{\text{Response_Bore_Sight}}$	Gimbal Laser Bore Sight Error Sample Standard Deviation..... [deg]
$S(f)$	Forward Fourier Transform []
S_x	Output Spectral Density..... []
S_{xf}	Output Cross-Spectral Density.... []
S_x	Sample Standard Deviation..... []
$S_{\bar{x}}$	Random Sample Standard Deviation..... []
$S_{\bar{x}_i}$	Random Sample Standard Deviation for Variable i..... []
T	Time Period..... [s]
t	Time..... [s]
$t_{v,P}$	Student t Variable..... []
$u_{\text{Actuation}}$	Uncertainty of the Actuation Angle..... [deg]
u_{Final}	Final Measurement Uncertainty.. []
u_x	Independent Uncertainty Component..... []
u_{Response}	Uncertainty of Response Angle... [deg]
$u_{\text{Reference_Assumption}}$	Uncertainty Introduced by Reference Laser Displacement Profile Assumption..... [deg]
$u_{\text{Reference_Bore_Sight}}$	Uncertainty Introduced by Reference Laser Bore Sight Error [deg]
$u_{\text{Reference_Camera_Distance}}$	Uncertainty Introduced by Reference Laser Camera to Target Surface Distance Error..... [deg]

$u_{\text{Reference_Distance}}$	Uncertainty Introduced by Error in Distance from Reference Laser Centre of Rotation to Target Surface [deg]
$u_{\text{Reference_Inclinometer}}$	Uncertainty Introduced by Laser Inclinometer Error [deg]
$u_{\text{Reference_Reprojection}}$	Uncertainty Introduced by Repositioned Camera Calibration [deg]
$u_{\text{Reference_Verification}}$	Uncertainty Introduced by Algorithm Accuracy Verification Tests..... [deg]
$u_{\text{Response_Assumption}}$	Uncertainty Introduced by Gimbal Laser Displacement Profile Assumption..... [deg]
$u_{\text{Response_Bore_Sight}}$	Uncertainty Introduced by Gimbal Laser Bore Sight Error ... [deg]
$u_{\text{Response_Camera_Distance}}$	Uncertainty Introduced by Gimbal Laser Camera to Target Surface Distance Error..... [deg]
$u_{\text{Response_Reprojection}}$	Uncertainty Introduced by Repositioned Camera Calibration [deg]
v_b	Systematic Standard Deviation Degree of Freedom []
v_R	Result Degree of Freedom []
v_s	Random Sample Standard Deviation Degree of Freedom..... []
X	X-Axis..... []
Y	Y-Axis..... []
Z	Z-Axis []
X_{Drone}	Drone X-Axis []

X_{Gimbal}	Gimbal X-Axis []
x_{centroid}	Barycentre X-Axis Co-ordinate .. [pixels]
$x(t)$	Inverse Fourier Transform []
$x_{\text{co-ordinate } ij}$	Co-ordinate of image Pixel [pixels]
Y_{Drone}	Drone Y-Axis []
Y_{Gimbal}	Gimbal Y-Axis []
y_{centroid}	Barycentre Y-Axis Co-ordinate .. [pixels]
$y_{\text{co-ordinate } ij}$	Co-ordinate of Image Pixel [pixels]
Z_{Drone}	Drone Z-Axis []
Z_{Gimbal}	Gimbal Z-Axis []
$\alpha_{\text{Inital_Guess}}$	Initial Angular Accuracy Guess .. [mrad]
β	Field of View [deg]
Δ	Absolute Uncertainty []
$\delta D_{\text{Reference}}$	Change in Reference Laser Distance to Target [mm]
$\delta d_{\text{wall_left}}$	Change in Reference Laser Distance to Target from Left Side of Support Frame [mm]
$\overline{\delta \text{Displacement_Difference}}_{\text{Reference}}$	Change in Reference Laser Dot Displacement [mm]
$\overline{\delta \text{Displacement_Difference}}_{\text{Response}}$	Change in Gimbal Laser Dot Displacement [mm]
$\overline{\delta \text{Displacement_Resoution}}_{\text{Camera}}$	Change in-image Resolution [pixels/mm]
$\delta D_{\text{Camera_Right_Distance}}$	Change in Distance from Camera to Target Surface Right Measurement [mm]
$\delta D_{\text{Camera_Left_Distance}}$	Change in Distance from Camera to Target Surface Left Measurement [mm]

δR	Change in Result Value []
δx_i	Change in Variable i's Value []
$\delta \theta_{\text{Frame}}$	Change in Frame Pitch Angle [deg]
$\delta \phi_{\text{Frame}}$	Change in Frame Roll Angle [deg]
$\delta \psi_{\text{Reference_Bore_Sight}}$	Change in Bore Sight Error..... [mrad]
$\delta \psi_{\text{Response_Bore_Sight}}$	Change in Bore Sight Error..... [mrad]
ϵ	Relative Uncertainty [%]
γ	Yaw..... [deg]
γ_{Drone}	Drone Yaw [deg]
Θ	Pitch Rotation Matrix []
θ	Pitch [deg]
$\theta_{\text{Actuation}}$	Actuation Angle [deg]
$\theta_{\text{Backswing_Error}}$	Gimbal Angular Response Error when Swung Away from the Gimbal Laser Target Surface [deg]
$\theta_{\text{Disp_Bore_Sight}}$	Sensitivity Index Bore Sight Error..... [deg/mrad]
θ_{Drone}	Drone Pitch [deg]
$\theta_{\text{Frontswing_Error}}$	Gimbal Angular Response Error when Swung Towards Gimbal Laser Target Surface..... [deg]
θ_{pitch}	Sensitivity Index to Inclinometer Pitch Error..... [mm/deg]
$\theta_{\text{R_D1}}$	Sensitivity Index for Reference Laser Distance to Target Measurement 1 [deg/mm]
$\theta_{\text{R_D2}}$	Sensitivity Index for Reference Laser Distance to Target Measurement 2 [deg/mm]

θ_{rf_1}	Sensitivity Index for Range Finder Measurement 1 [deg/mm]
θ_{rf_2}	Sensitivity Index for Range Finder Measurement 2 [deg/mm]
θ_{roll}	Sensitivity Index to Inclinometer Roll Error [mm/deg]
θ_{x_i}	Sensitivity Index for Variable i ... []
Φ	Roll Rotation Matrix..... []
ϕ_{Drone}	Drone Roll..... [deg]
σ_{phase}	Plant Output Signal Phase..... [deg]
$\psi_{Reference_Bore_Sight}$	Reference Laser Bore Sight Error [mrad]
$\psi_{Response_Bore_Sight}$	Gimbal Laser Bore Sight Error ... [mrad]
ω_{input}	Controller Output Signal Frequency..... [rad/s]

Superscripts

n	Power []
n_i	Number of Image Y-Axis Pixels. [pixels]
n_j	Number of Image X-Axis Pixels. [pixels]

Subscripts

De-trended	De-trended Data []
ij	Image Co-ordinate of a Pixel [pixels]
sub – pixel@fps	Sub-pixel Accuracy at Given Frame Rate []
@fps	Given Frame Rate..... [fps]

1 Introduction

The focus of this study is to experimentally investigate a two-axis gimbal for varying gimbal frame disturbance frequencies and amplitudes. The aim is to produce disturbance rejection performance data in the frequency domain. Such data is used when designing, or evaluating, a measurement system that uses a gimbal for sensor, or measurement device, orientation under non-static gimbal-base conditions. To establish the context of this study, this chapter covers the project background, followed by the project objectives. The investigation plan that was followed throughout the project is then discussed, with the chapter concluding with the thesis outline.

1.1 Background

At the University of Stellenbosch, the Solar Thermal Energy Research Group (STERG) focuses on research that improves the performance of Concentrated Solar Power (CSP) plants, as seen in Figure 1, and that reduces their initial investment and maintenance costs.



Figure 1. The Solucar PS10 solar power plant in Spain, with the heliostat field in the foreground and the central tower receiver in the background (Fedkin & Dutton, 2012).

Until now, heliostat maintenance, such as heliostat cleaning, has been done using manual labour and machines, while heliostat calibration has been automated. Although each method is effective, each one comes at a cost.

Manual labour is time-consuming, such as when a technician needs to perform a visual inspection, and when cleaning or maintenance of each heliostat has to be done. Although automation removes the need for manual calibration and results in higher accuracy and more consistent calibrations, it comes at a higher financial cost. A 50 MW CSP plant, such as Khi Solar One, requires over 4000 heliostats, where one to two heliostats can be calibrated per calibration target (Abengoa Solar, 2016).

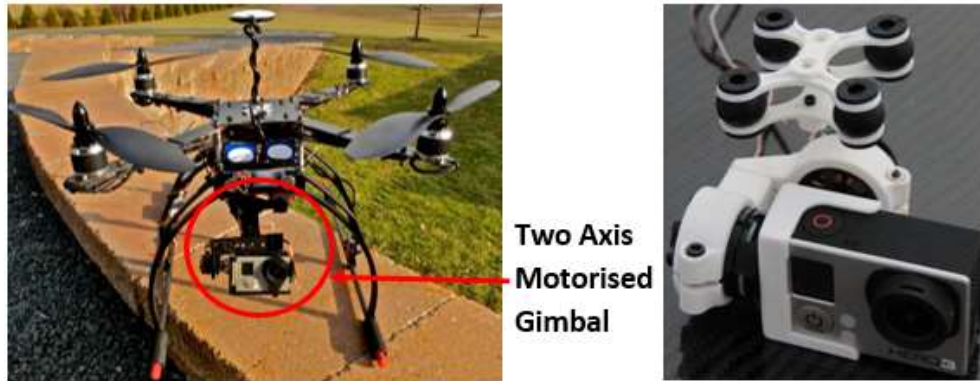
As the calibration process takes a few minutes, the time taken to cycle back to a calibrated heliostat can take weeks, if not months. Therefore, a heliostat needs to be able to operate within the calibration tolerances for months at a time in order to be effective. This requires the heliostat and its foundations to be sturdy, which can be costly. If each heliostat can be calibrated every few days, rather than every few months, the time that the heliostat needs to remain within the operational tolerances is reduced, thereby reducing the manufacturing costs of the heliostat and its foundations.

To achieve this and maintain calibration accuracy and consistency, STERG is investigating the use of automated drones to perform the inspections, calibrations and cleaning of heliostats. The research specifically focuses on the calibration of heliostats using a drone's hovering position to perform the calibration. STERG has been performing drone focused research to investigate and improve the feasibility of using drones in CSP plants, such as in obstacle avoidance (Van Breda, 2016) (Coetzee, 2017), position tracking accuracy (Potgieter, 2016), (Lock, 2016) (Minnaar, 2017) and state estimation (Minnaar, 2017).

Similar to helicopters, drones are under-actuated, which means that there are fewer actuators than degrees of freedom. This means that it is difficult, if not impossible, to achieve particular movements with the actuators present. In the case of the drone, the motors provide good control for roll, pitch, yaw and vertical translation. However, there is not a set of motors to provide direct thrust for horizontal translations, therefore the drone must rotate in order to split the motor thrust between providing horizontal thrust and lift thrust.

These rotations would be necessary if a drone is hovering and attempting to maintain a fixed position, and can be problematic when taking measurements or photographs. Although drones do yaw, their control of this yaw is superior to their control of their horizontal translation, as no pitch or roll rotations are required to achieve this. Thus, to direct a sensor, or camera, in yaw the drone is used. Therefore, a two-axis motorised gimbal, as seen in Figure 2, is used to isolate the camera, or sensor, from the pitch and roll rotations.

For drones and gimbals to be able to perform measurement and inspection tasks, the accuracies and limitations in the combined system need to be understood. Unlike drones, dynamic performance data for gimbals is not readily available. Specifically, performance data for gimbals subjected to combined rotations and translations, such as those seen for gimbals attached and operated underneath drones, as seen in Figure 3, is not available.



**Two Axis
Motorised
Gimbal**

Figure 2. Drone and mounted two-axis motorised gimbal (Left). A close-up of a two-axis motorised gimbal with a mounted camera (Right) (FSMultirotors, 2014). The purpose of the gimbal is to reduce the effect that drone disturbances have on sensor, or camera, performance. Note that these are just examples, and not the gimbal used for this thesis, or the drone used by STERG.

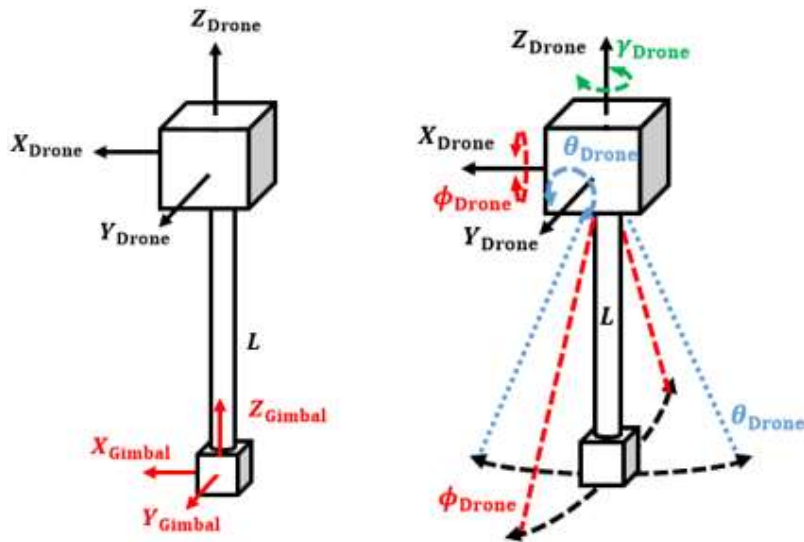


Figure 3. A box model of the drone and gimbal, showing the drone and gimbal axis systems, where the positive x-axis direction points toward the front of the drone (Left). The red, dashed line and blue, dotted line indicate the drone roll and pitch rotations respectively. They also show how the gimbal is both rotated and translated during the drone rotations (Right). Note that the green rotation showed about the z-axis of the drone is the drone yaw.

The reason that gimbal performance data is not readily available is that general commercial use of gimbals focuses on the stabilisation of video and camera images, such as for the film industry. Since the clients are not interested in the detailed gimbal performance, there has been no need to publish the gimbal performance results.

If gimbal research was performed, it focused on gimbal performance under static base conditions, such as in precision mirror control (Optical Surfaces, 2018), or Unmanned Aerial Vehicle (UAV) communications (Harris, Sluss Jr., Refai, 2005). If research of the gimbal in the frequency domain was done, it was either for military applications, and therefore not available to the public, or not the main focus of the research, and therefore did not produce significant insight into gimbal performance.

Some gimbal simulation performance data has been published, though, by Jia, Nandikolla, Haggart, Volk and Tazartes (2017). The research produced simulated gimbal performance data under a fixed, sinusoidal disturbance condition of 10° and 0.07955 Hz, including system friction, low-level vibration and structural resonance (Jia, et al., 2017). The study investigated the effect of sensor quality on system performance under ideal and non-ideal structural and environmental conditions. The focus was centred on the effect of sensor quality change and not on the frequency and amplitude of the disturbance, structural and environmental inputs. Therefore, limited gimbal performance data was published.

One of the measures of performance for a gimbal is in its ability to counter angular disturbances, such as drone rolling. Therefore, the angle by which the gimbal amplifies, or attenuates, the angular disturbance. For gimbals, the effectiveness of this ability will vary with the disturbance frequency. When quantifying this in the frequency domain, the gimbal's response gain and phase describe the gimbal's effectiveness for each disturbance frequency.

When a gimbal has to isolate a measurement system sensor from angular disturbances, the gimbal's attenuation of angular-disturbances becomes its most important function. In other words, the gimbal's ability to operate within the required angular accuracy limits becomes most important. Therefore, between the gain and phase of the gimbal's responses, the gain becomes the most important of the two.

In addition to drone angular disturbances, gimbals are subjected to high frequency vibrations, which are transferred through the drone frame. Sources of these high frequency vibrations include the drone blades and their blade pass frequencies. To reduce the effect of these vibrations on the drone controller and gimbal, manufacturers supply drones and gimbals with vibration isolation pads. Therefore, the purpose of the vibration isolation pads is to filter out high frequency vibrations, or disturbances, to the gimbal.

This thesis investigates a gimbal's peak responses for varying angular-disturbance frequencies and amplitudes. The aim of the study is to gather information about the gain of a gimbal's response. Therefore, the data should ideally be limited to the response of the gimbal itself. As gimbal vibration isolation pads alter the conditions the gimbal is subjected to, the gimbal used in the study is not used with vibration isolation pads.

Since very little published work on dynamic gimbal pitch performance is available, the thesis scope is limited to the investigation of a single axis of response, namely

gimbal pitch. In addition, the types of disturbances that will be investigated are steady state, sinusoidal disturbances.

1.2 Thesis Objectives

In order to gain insight into how the performance of the gimbal pitch response would be affected by drone rotations and vibrations during drone hovering, the following objectives had to be achieved:

1. Recording of accurate gimbal pitch response data for varying pitch and roll disturbance frequencies and amplitudes.
2. Presenting and analysing the results in the frequency domain to draw conclusions about the gimbal's performance.

1.3 Investigation Plan

The project's main focus was to produce accurate and reliable data, which would be able to provide clear insight into gimbal response for a range of disturbances. The investigation was divided into four stages:

1. Measuring of a drone's movements during hovering to find the frequency range in which the gimbal has to be effective.
2. Designing and building a measurement system that can measure very small rotations, in the order of milliradians, of a gimbal.
3. Designing and building a system that will disturb the gimbal in the same way the drone would.
4. Testing the gimbal performance in pitch, to disturbances in pitch and roll separately.

1.4 Thesis Outline

Chapter 2 covers the thesis literature review, while chapter 3 discusses the conceptualization and design of the disturbance system and experimental setup. Chapter 4 discusses the conceptualization and design of the system that captures and measures the gimbal disturbances and responses. Chapter 5 covers the preliminary tests and their results, followed by chapter 6 containing the discussion of the results of the final experiments of the gimbal responses to pitch disturbances and roll disturbances. Chapter 7 contains the conclusions and recommendations.

Appendix A contains the dimensions of the rotating assembly, which the gimbal was attached to. Appendix B contains the camera calibration pattern, the tracking algorithm verification test plan and setup parameters for these tests. Appendix C contains camera distance-to-target surface calculations for the required angular resolution. Appendix D contains the error and uncertainty propagation analysis, while Appendix E contains the graphed results of the structure natural frequency experiments.

Appendix F contains the gimbal response gain plots to the pitch actuations, while Appendix G contains the gimbal response gain plots to roll actuations.

2 Literature Review

In this chapter the background literature and theory is reviewed. Section 2.1 discusses gimbals and how they work, while section 2.2 covers the motors which operate on the gimbal. Section 2.3 discusses camera calibration, which is applied in measuring features in images and is used in measuring the gimbal actuations and responses. Section 2.4 covers subpixel accuracy and how it improves measurements made from images. Section 2.5 discusses the Fourier Transform and the analysis of signals in the frequency domain, while section 2.6 discusses frequency domain performance measurements. Section 2.7 discusses the Monte Carlo Simulation, which is used in evaluating the uncertainty introduced by certain operating assumptions. Finally, section 2.8 discusses the methods and rules for determining the uncertainty in measurements.

2.1 Two Axis Motorised Gimbals

Two-axis motorised gimbals are devices, which maintain the specific pitch and roll pose of their device mount, as seen in Figure 4. An important factor in their operation is the positioning of their centre of mass. For the gimbal to be able to operate, its centre of mass must be in line with all the gimbal's axes of rotation. Motors are mounted on the axes of rotation and are used to maintain the desired pose.

To measure the angular displacement of the gimbal base and device mount, Inertial Measurement Units (IMU) are mounted to each. Each IMU consists of three gyroscopes and three accelerometers, whose measurements are combined by means of sensor fusion to measure the angular displacement from an initial reference, which is established during gimbal calibration. The accelerometers are used to establish the orientation of each IMU during calibration and operation by comparing a known IMU axis direction with the measured direction of gravity.

In the calibration process, the control system operating the two-axis gimbal is set to maintain the specific roll and pitch angles that the two IMUs are detecting, with the direction of gravity being used as reference. Thus, the gimbal control system will try to maintain a device mount pose that is parallel to the initial reference pose determined during calibration. When operating at low rotation speeds, the most significant force to which the accelerometers is subjected to is due to gravity. However, at higher speeds tangential and radial accelerations taint the determined direction of the force of gravity, thereby altering the accelerometer's determination of the IMU's pose.

Note, in this thesis, the entire device, as seen in Figure 4, is defined as the gimbal, while the device mount, or mounting surface, connected to the rolling axis is defined as the device mount.



Figure 4. An example of a two-axis gimbal and the structures that correspond to a gyroscope (FSMultirotors, 2014).

It is possible for the gimbal to operate with one IMU, but control is improved when a device mount IMU and gimbal base IMU are used in tandem (Basecam Electronics, 2017).

2.2 Brushless Direct Current Motors and Sub-pole Accuracy

The motors used in order to adjust the gimbal pose are Brushless Direct Current (BLDC) motors, which actuate each gimbal axis. BLDC motors use combinations of two or more activated electromagnets, or poles in the motor stator to induce a torque on the permanent magnet motor rotor. In this way, the rotor can be “stepped” clockwise or anti-clockwise, by deactivating and activating consecutive stator pole pairs, see Figure 5. The polarity of each stator pole is determined by the direction that the current is sent through their coils.

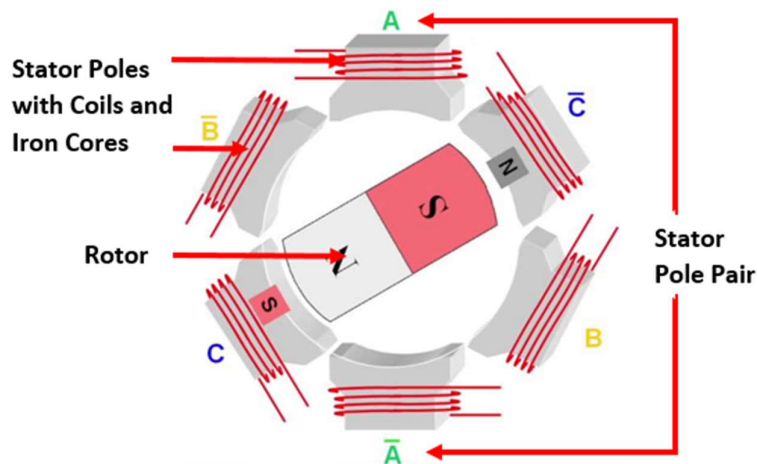


Figure 5. An example of a six-stator pole, two-rotor pole brushless direct current (BLDC) motor (Texas Instruments, 2013).

By using specific combinations of activated pole pairs around the stator, the rotor can be rotated to positions in between stator poles and, depending on the number of poles in the stator, can result in a high degree of angular accuracy. As the angular resolution of the motor is governed by the number of poles it has, it implies then that the higher the number of poles in the stator, the smaller the angle between each stator pole and mid-pole position, and therefore the higher the degree of angular accuracy that can be achieved. It is understood that purpose-built gimbals, under static base conditions, can achieve angular accuracies well below 0.005° (Harris, et al., 2005).

2.3 Camera Calibration

Cameras are used to capture and record object dynamics that would normally not be observable by the human eye, such as high frequency responses, dynamics of structures, or high speed movements of in-image features. Concerning the latter, these displacements can be measured in pixels and converted to world co-ordinate units, given that the transform from the camera co-ordinate system and the world co-ordinate system is determined.

In order to determine the transform, the camera's intrinsic and extrinsic parameters need to be determined, discussed below, which are determined through a camera calibration. The calibration determines the camera lens and image sensor parameters, which allow for the position triangulation, in millimetres, of objects within an image. In Matlab, the "Computer Vision System Toolbox™" is used to perform these calibrations and provides some of the more advanced image-processing functions (MathWorks, 2016).

The algorithm uses the lens distortion model and the pinhole camera model, as seen in Figure 6, to perform the camera calibrations. The pinhole model does not account for lens distortion, as a pinhole camera does not have a lens. However, it does allow for the estimation of the camera's intrinsic and extrinsic parameters.

The extrinsic parameters represent the rotations and translations, or the transformation matrix, required to move the co-ordinate system from the world co-ordinate system to that which is relative to the camera co-ordinate system, or vice versa. The intrinsic parameters represent the projection of the camera co-ordinate system onto the two-dimensional co-ordinate system of the image plane and so, represent the transform from the camera's co-ordinate system to the image plane co-ordinate system (MathWorks, 2016).

Together these allow for the determination of the homography which, similar to the rotation matrices of the Euler angles, perform a transformation, or mapping, of co-ordinates from one co-ordinate system to another. Therefore, the homography allows for the determination of the co-ordinates of an in-image feature, relative to an in-image plane origin, as seen in Figure 7, in terms of millimetres instead of pixels.

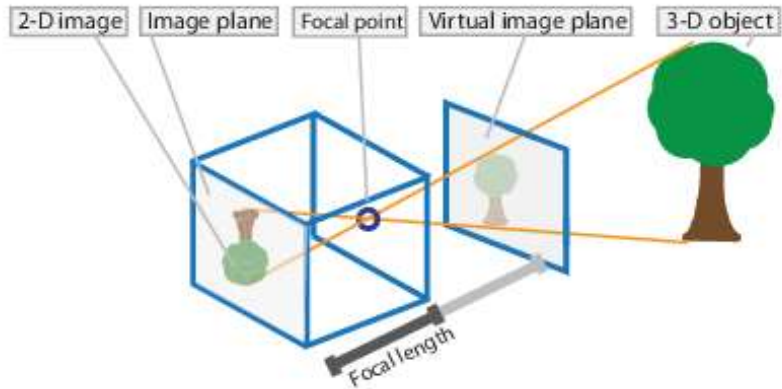


Figure 6. The pinhole camera model (MathWorks, 2016)

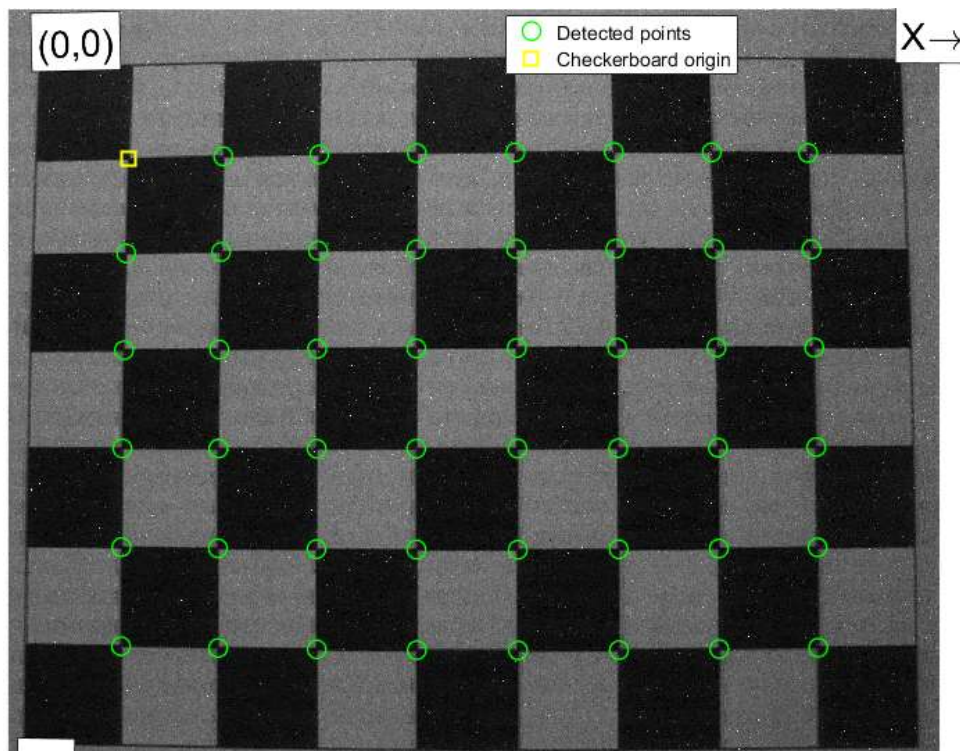


Figure 7. Camera calibration board origin after being processed by the Matlab camera calibrator application. The position of the yellow box in the top left corner, indicates the position of the origin. The position of the origin is determined by the application and is defined by the dimensions of the calibration board. The long and short sides of the rectangle made by the green circles, which are the detected corners of the calibration board, determine which is the x-axis and which the y-axis, respectively. Note that the positive y-axis is shown to be downwards.

The lens distortion model of the camera allows for the estimation of the radial and tangential distortion parameters. Radial distortion occurs when light enters the lens

near its rim, thus incorrectly bending the incoming light and warping the image, as seen in the example in Figure 8. Tangential distortion occurs when the image plane and the lens are not parallel, and therefore light is again incorrectly bent, as can be seen in the example in Figure 9 (MathWorks, 2016). Once the distortions are determined, they can be removed from the image, as seen in Figure 10, thus removing their negative effects.

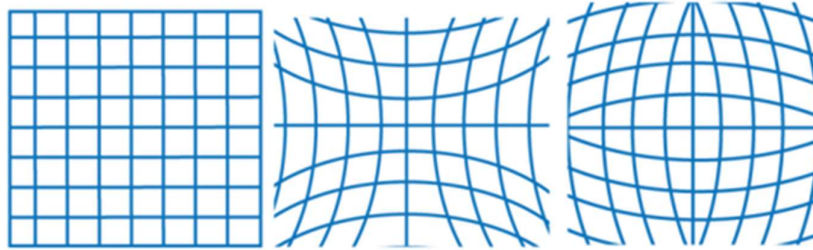


Figure 8. Two examples of radial lens distortion. Most left is the original, undistorted pattern. In the middle is the example of negative radial distortion and on the right is the example of positive radial distortion (MathWorks, 2018).

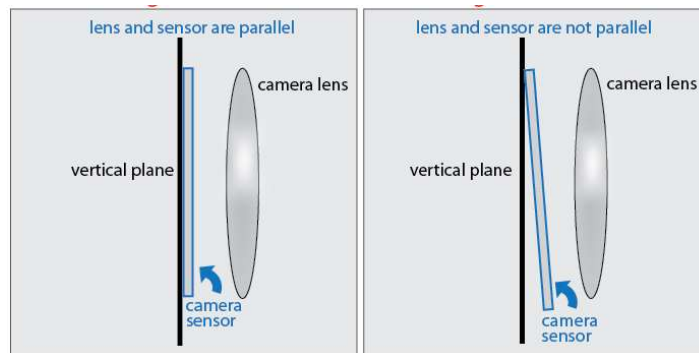


Figure 9. Tangential distortion example showing what lens/sensor misalignment causes tangential distortion (MathWorks, 2018).



Figure 10. The undistorting of the datum photo of the calibration board. The image on the left is the original photograph, while the image on the right is the undistorted photograph. Note that the calibration board lines on the left are slightly bowed, whereas in the undistorted image on the right, these lines have been straightened (Mathworks, 2014).

2.4 Subpixel Point Triangulation

In triangulating the position of a feature in an image, the most accurate co-ordinates that can be obtained, using pixel level accuracy alone, will be to the centre of a pixel nearest to the centroid of the feature. The reason for this is that the image is broken into discrete data, pixels, where within each pixel the image data is uniform.

Each pixel contains information of the combination of red, green and blue light that makes up the colour in that pixel as well as the intensity of these three colours. If a photograph is taken in greyscale only the intensity, or darkness, of the shade of the pixels changes throughout the image. In finding the centroid of an in-image feature these properties can be used in a method known as the Barycentre method, which determines the centroid of a feature in the image on a sub-pixel level.

The Barycentre is used in astronomy, or astrophysics, where it is the mass weighted centroid of orbit of the two, or more, orbiting bodies. If image pixels are used in the same way, the pixels that contain an in-image feature can be used to determine the weighted x and y centroid co-ordinates of an in-image feature using equations (1) and (2) (Song, Wu, Guo and Li, 2013). The terms n_i and n_j refer to the total number of pixels in the image y-axis and x-axis respectively.

For this method to be effective, though, the background, or unwanted in-image data, must be removed. Thus, two pixel intensity bounds are determined for the information in the images that is not needed, or not of concern. If the pixel intensity value falls outside of the bound, the pixel value is set to 0, otherwise the x and y co-ordinates of the pixel are stored, and the product of the pixel co-ordinates and its intensity is stored. The Barycentre's accuracy ranges between 0.5-0.2 of a pixel if a high-quality camera is used (Song, et al., 2013).

$$x_{\text{centroid}} = \frac{\sum_i^{n-i} \sum_j^{n-j} (I_{\text{Intensity}_{ij}} x_{\text{co-ordinate}_{ij}})}{\sum_i^{n-i} \sum_j^{n-j} (I_{\text{Intensity}_{ij}})} \quad (1)$$

$$y_{\text{centroid}} = \frac{\sum_i^{n-i} \sum_j^{n-j} (I_{\text{Intensity}_{ij}} y_{\text{co-ordinate}_{ij}})}{\sum_i^{n-i} \sum_j^{n-j} (I_{\text{Intensity}_{ij}})} \quad (2)$$

2.5 The Fourier Transform

Any signal, or waveform, that exists in the physical world can be replicated by summing sine waves at the correct frequencies, phase and amplitudes (Agilent Technologies, 2000). Baron Jean Baptiste Fourier showed that if a signal could be viewed in the frequency domain, one would be able to see the individual sine wave frequencies and their specific amplitudes, which make up the final signal (Inman, 2014).

This mathematical process, which transforms a given signal from a time-dependent function into a frequency-dependent function, is known as the Fourier Transform (FT). Equation (3) represents the forward Fourier transform, from a time-dependent to a frequency-dependent function, whereas equation (4) represents the Inverse Fourier Transform (IFT) (Inman, 2014).

$$S(f) = \int_{-\infty}^{\infty} x(t) e^{-j2\pi ft} dt \quad (3)$$

$$x(t) = \int_{-\infty}^{\infty} S(f) e^{j2\pi ft} df \quad (4)$$

The advantage of this transform is that it allows the user to identify erroneous results in their data, or noise in their sampled signal. In this way, the user can get a clearer idea of what is occurring in the system that is being monitored, and take steps to address the problems, or remove the introduced noise in the measurements.

The FT is continuous and therefore causes problems when computation of the transform must be computed from digitally captured data, or when digital devices are being used. Therefore, the Discrete Fourier Transform (DFT) is used, which

gives an approximation of the true FT of the given signal by means of the use of numerical integration (Agilent Technologies, 2000).

For large numbers of samples, the computation time of the DFT becomes a problem, and so the Fast Fourier Transform (FFT) was developed, which uses the assumption that the number of samples taken is a power of two, which allows for faster computation time (Agilent Technologies, 2000).

A critical point here is that by taking a finite set of data, it is assumed that the signal repeats the set of data in the exact same way for infinity. Therefore, if the length of the data set in time is not a multiple of the signal's period, discontinuities are introduced by the assumption above (Figiola & Beasley, 2011), (National Instruments, 2016). The result of this is that false high frequency components are introduced by the FFT (Agilent Technologies, 2000).

To remove this, windowing of the data is used (Inman, 2014). A window is a set of scaling values which are used to alter a given set of data values, as seen in Figure 11. The start and the end of the window drives the data values to zero, while the scaling values in-between gradually build to a scaling value of 1. The example below was used in scaling a 10 s sample, 1 Hz signal, as seen in Figure 12. Note that the window size was set to be the length of the entire data set. The smooth increase and decrease of the scaling values are required, to ensure that no additional discontinuities are introduced.

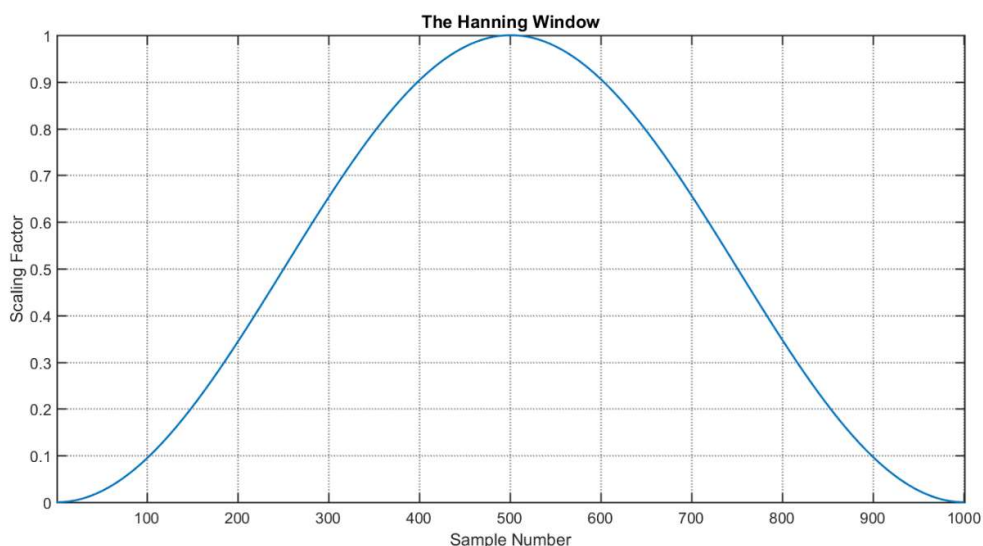


Figure 11. The Hanning window and the respective scaling factors for each sample in a data set.

A draw back of windowing is that the data is altered. Therefore, dynamics are introduced into the signal, which translate to incorrect signal components in the FFT. By making the window size smaller, overlapping the windows and averaging the FFTs of each window, these affects can be reduced. When done this, though,

there is a risk of losing significant frequency resolution, as the number of data points used in determining the FFT becomes smaller. Therefore, the window type, size and overlapping must be balanced for the type of dynamics that are of interest in the data.

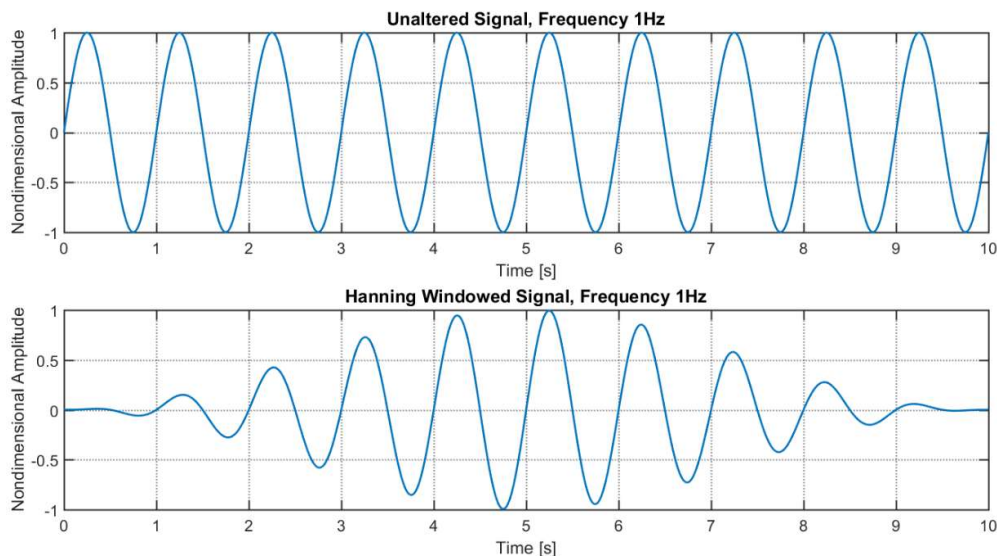


Figure 12. An example of the effect of a Hanning window of a 1 Hz data set. Note, the window length is the full length of the data set.

In the Fourier analysis of accelerometer signals, which exhibit a linear relationship between the analogue voltage signal they produce and the acceleration to which they are subjected, users are able to determine what accelerations are occurring, where in the frequency spectrum, and at what amplitude.

Because no device, or system, is free of signal noise, or interference, the acceleration signal that is produced by the accelerometer contains signal noise which affects the accuracy of the signal and other post-acquisition signal processing processes which are more sensitive to signal noise. By using FFT of the acceleration signal, the user can distinguish between signal noise, expected signals, and those that were not expected.

2.6 Frequency Domain Performance Measurements

Just as systems' performances can be evaluated and quantified in the time domain, so they can be evaluated and quantified in the frequency domain. In quantifying a system's performance in the frequency domain, the response of the system over a range of input frequencies is determined. This gives an indication of the transfer function, which describes the system's responses for a given input.

When working with mechanical systems, the vibrations the system generates, for an input force and frequency, can be of great importance. Phenomena such as

resonance can cause damage, or affect performance, and as such, the frequencies at which this occurs need to be determined.

As vibrations are accelerations, the relationship is one that is between the input force and the output acceleration. This relationship is known as the Frequency Response Function (FRF) and is the relationship between the spectral densities of the output and the input, as seen in equation (5). S_x is the spectral density of the output, and is determined by the Fourier Transform of the autocorrelation function, R_x , of the output, as seen in equations (6) and (7) respectively (Inman, 2014). Note that the input spectral density and autocorrelation function for the input, are determined in the same manner as in equations (6) and (7), but using the input force. The FRF is comprised of complex numbers and describes the magnitude and phase of a structure's response to harmonic excitation (Inman, 2014). The response magnitude is synonymous to the system gain, which can be plotted over the frequency range of interest.

$$S_x = |Q(\omega)|^2 S_f \quad (5)$$

$$S_x = \frac{1}{2\pi} \int_{-\infty}^{\infty} R_x e^{-j\omega\tau} d\tau \quad (6)$$

$$R_x = \lim_{T \rightarrow \infty} \frac{1}{T} \int_0^T x(t) x(t + \tau) dt \quad (7)$$

The accuracy of an FRF measurement is determined by means of calculation of the coherence function, as seen in equation (8). The coherence is determined by using the spectral density and cross-spectral density functions, which can also be used to determine the FRF. Equation (9) shows how the output spectral density can be determined by the product of the FRF and the cross-spectral density. The cross spectral density, S_{xf} , is the Fourier Transform of the cross-correlation, R_{xf} , as seen in equations (10) and (11), respectively. Note that the input's cross-spectral density is determined using equations (10) and (11), but with the input force.

$$C = \frac{|S_{xf}|^2}{S_{xx} S_{ff}} \quad (8)$$

$$S_x = Q(\omega) S_{xf} \quad (9)$$

$$S_{xf} = \frac{1}{2\pi} \int_{-\infty}^{\infty} R_{xf} e^{-j\omega\tau} d\tau \quad (10)$$

$$R_{xf} = \lim_{T \rightarrow \infty} \frac{1}{T} \int_0^T x(t) f(t + \tau) dt \quad (11)$$

As the output and input each have their own spectral and cross-spectral densities, the ratio of their FRFs can be used to check the consistency and accuracy of the FRF used. Therefore, for a linear system, the same response will be seen for both FRFs, resulting in a coherence equal to one. For a non-linear system, or noisy signal, however, the responses will differ between the two functions, resulting in a low coherence (Inman, 2014).

Therefore, the coherence assumes a value between zero and one, where the closer the coherence is to one, the more trustworthy the corresponding FRF will be at that frequency. Low correlation values indicate noise, non-linearity, or insufficient excitation to measure a meaningful response (Inman, 2014).

In control systems, the performance of a controller can be evaluated based on the time domain, or frequency domain, responses. A system's frequency domain performance indicates how a system will perform for specific reference and disturbance frequencies. It is used to describe the dynamics of the system being investigated at specific frequencies.

For Single Input Single Output (SISO) systems the Bode plot is used to represent the frequency domain response of the system (Franklin, Powel, Naeini, 2010). The Bode plot assumes that the plant is a linear time invariant system. Thus, the assumption is that the system is subjected to a steady state sinusoid, as seen in equation (12), and responds with the same frequency, but with a different magnitude and phase, as seen in equation (13).

$$u(t) = B \cdot \sin(\omega_{\text{input}} t) \quad (12)$$

$$y(t) = A \cdot \sin(\omega_{\text{input}} t + \sigma_{\text{phase}}) \quad (13)$$

The phase difference between the two signals corresponds to a time difference between two corresponding points from each signal, such as the peak amplitudes. The phase difference is as a result of dynamics within the plant, which either give the response signal a phase gain, positive phase difference, or phase lag, which would give the response signal a negative phase difference with respect to the input signal. Positive phase difference implies that the signal in question leads the input signal in the time domain, whereas negative phase difference implies that the signal in question lags behind the input signal in the time domain.

The amplitude difference is also as a result of the plant's dynamics and is referred to as the plant's signal gain. It is the magnitude ratio by which the plant amplifies, or attenuates, the input signal at a specific frequency ω , see equation (14) (Franklin, et al., 2010).

$$A = B M \quad (14)$$

The advantage of describing a system's response in this way is that critical frequencies, such as natural frequencies or break frequencies, are clearly visible and can be taken into account during the design of the plant and controller. A limitation of this method, though, is that it can only be used with SISO systems which exhibit linear responses. Thus, if the response is not sinusoidal, the bode plot cannot be used.

2.7 Monte Carlo Simulations

When multiple, independent variables affect a result and the effects of the different combinations need to be determined, or modelled, the Monte Carlo simulation can be used.

The Monte Carlo simulation is a tool that is used in modelling, by means of large numbers of iterations, to investigate the result of multiple system input variables with significant uncertainty (Kleyner & O'Connor, 2012). The simulations are performed by randomly selecting the system inputs and the corresponding variables affecting them, from their respective distributions. Depending on the system information available, the distributions will be uniformly distributed, or normally distributed. Therefore, through random selection of the input variable values and the dynamics that affect them, a random system output can be produced. By iteratively repeating this process, nearly all the possible variable input combinations and variations can be evaluated in a relatively short period of time.

Under a uniform distribution all the values of a variable have an equal selection probability, and therefore suits system simulations where information on variable means and standard deviations are incomplete, or simply non-existent. The use of variable values, randomly selected from a normal distribution, are suited to

simulations where system operational data, such as input variables' means and standard deviations, are available, or can be defined beforehand.

In this thesis, Monte Carlo simulations are used in determining the limits of two assumptions used in measuring gimbals inputs and responses, in addition to the measurement uncertainties they introduce.

2.8 Measurement Uncertainty Propagation and Determination

When performing any measurement there is an error, or tolerance, associated with the device and system being used and therefore the resulting measurement. When a series of measurements are made, these errors propagate and add up, affecting the final uncertainty of the result significantly and thus need to be taken into account.

When dealing with independent variables for a specific measurement, the resulting uncertainty u_x , for a specific probability P , can be determined using equation (15). $b_{\bar{x}}$, equation (16), is the systematic standard uncertainty of a particular measurement, whereas $s_{\bar{x}}$, equation (17), is the random sample standard deviation of the sample standard deviation, s_x , for N measurements. The systematic standard uncertainty is a one standard deviation estimate of the systematic uncertainty, $B_{\text{measurement}}$, that is constant for repeated measurements and constant operating conditions, such as equipment tolerance. Random sample standard deviation, on the other hand, is the standard deviation of the set of measurements of a variable, divided by the square root of the number of data points used in determining the standard deviation.

The term $t_{v,P}$ is the student's t variable, which represents a precision interval given the probability P and variable degrees of freedom v (Figiola & Beasley, 2011). The degrees of freedom of a value is the number of data points minus the number of parameters used in determining the value. When multiple individual measurement uncertainties interact, the uncertainty of the result is determined using the root-sum-squares, or RSS, method combining all the uncertainties, as seen in equation (18) (Figiola & Beasley, 2011). Note that K_u is the number of uncertainties.

$$u_x = t_{v,P} \cdot \sqrt{b_{\bar{x}}^2 + s_{\bar{x}}^2} \quad (15)$$

$$b_{\bar{x}} = \frac{\pm B_{\text{measurement}}}{t_{v,P}} \quad (16)$$

$$s_{\bar{x}} = \frac{s_x}{\sqrt{N}} \quad (17)$$

$$u_{\text{Final}} = \sqrt{\sum_{k=1}^{K_u} (u_x)_k^2} \quad (18)$$

If a variable is affected by more than one set of systematic and random standard deviations, the individual standard deviations are combined to produce the combined systematic and random standard deviation equations, see equations (19) and (20) respectively. Equation (21) is then used to determine the degree of freedom to determine the t value and equation (15) is used again to determine the combined uncertainty of the variable (Figiola & Beasley, 2011). Note that K_b is the number of elements of the final systematic standard deviation, K_s is the number of elements of the final random sample standard deviation and K_{sb} is the largest of the two numbers K_b and K_s . If K_b and K_s are not equivalent, the components for which no systematic, or random sample, standard deviations exist, are set to zero.

$$b_{\text{Final}} = \sqrt{\sum_{k=1}^{K_b} (b_{\bar{x}})_k^2} \quad (19)$$

$$s_{\text{Final}} = \sqrt{\sum_{k=1}^{K_s} (s_{\bar{x}})_k^2} \quad (20)$$

$$v = \frac{\left(\sum_{k=1}^{K_{sb}} (s_{\bar{x}}^2)_k + (b_{\bar{x}}^2)_k \right)^2}{\sum_{k=1}^{K_{sb}} \left((s_{\bar{x}}^4)_k / v_k \right) + \sum_{k=1}^{K_{sb}} \left((b_{\bar{x}}^4)_k / v_k \right)} \quad (21)$$

Since results are functions of multiple independent measured variables, each variable uncertainty has a functional relationship with the result value. This functional relationship is known as the sensitivity index, see equation (22). This index describes the relationship between each variable uncertainty and the result. If the result is a function of multiple variables, it implies then that the systematic and

random uncertainties are also functions of multiple variables, see equations (23) and (24) respectively. The same holds for determining the degree of freedom, especially if the number of measurements made for each variable are not the same, which is accounted for in determining the degree of freedom in equation (25) (Figiola & Beasley, 2011). Note that $L_{\text{variables}}$ is the number of independent variables.

$$\theta_{x_i} = \frac{\delta R}{\delta x_i} \quad (22)$$

$$b_R = \sqrt{\sum_{i=1}^{L_{\text{variables}}} [\theta_{x_i} b_{\bar{x}_i}]^2} \quad (23)$$

$$s_R = \sqrt{\sum_{i=1}^{L_{\text{variables}}} [\theta_{x_i} s_{\bar{x}_i}]^2} \quad (24)$$

$$v_R = \frac{\left(\sum_{i=1}^{L_{\text{variables}}} \left((\theta_i s_{\bar{x}_i})^2 + (\theta_i b_{\bar{x}_i})^2\right)\right)^2}{\sum_{i=1}^{L_{\text{variables}}} \left(\frac{(\theta_i s_{\bar{x}_i})^4}{v_{s_i}}\right) + \sum_{i=1}^{L_{\text{variables}}} \left(\frac{(\theta_i b_{\bar{x}_i})^4}{v_{b_i}}\right)} \quad (25)$$

For correlated errors, such as cases where the same measurement device is used to measure two different variables, equations (26) and (28) are used to account for the effect on the systematic and random uncertainties respectively. The last variables in equations (26) and (28), $b_{\bar{x}_i \bar{x}_j}$ and $s_{\bar{x}_i \bar{x}_j}$ respectively, are known as the co-variance for each error, and account for the number of errors that are correlated. These co-variances are determined using equations (27) and (29) respectively (Figiola & Beasley, 2011). Note that $L_{\text{variables}}$ refers to the number of independent variables, H refers to the number of errors that are correlated between the variables and h refers to the current error.

$$b_R = \sqrt{\sum_{i=1}^{L_{\text{variables}}} (\theta_i b_{\bar{x}_i})^2 + \sum_{i=1}^{L_{\text{variables}}-1} \sum_{j=i+1}^{L_{\text{variables}}} \theta_i \theta_j b_{\bar{x}_i \bar{x}_j}} \quad (26)$$

$$b_{\bar{x}_i \bar{x}_j} = \sum_{h=1}^H (b_{\bar{x}_i})_h \cdot (b_{\bar{x}_j})_h \quad (27)$$

$$s_R = \sqrt{\sum_{i=1}^{L_{\text{variables}}} (\theta_i s_{\bar{x}_i})^2 + \sum_{i=1}^{L_{\text{variables}}-1} \sum_{j=i+1}^{L_{\text{variables}}} \theta_i \theta_j s_{\bar{x}_i \bar{x}_j}} \quad (28)$$

$$s_{\bar{x}_i \bar{x}_j} = \sum_{h=1}^H (s_{\bar{x}_i})_h \cdot (s_{\bar{x}_j})_h \quad (29)$$

When determining the uncertainty of a measurement it can be represented as an absolute uncertainty, which has the same units as the measurand, or as a relative uncertainty, which is unitless and is a fraction of the measurand (Figiola & Beasley, 2011). An example of absolute uncertainty can be found in equation (30) where the uncertainty of a mass measurement is given, while an example of relative uncertainty of the same mass is given in equation (31) (Ellison & Williams, 2012).

$$m = 4.4 \text{ kg} \pm 0.2 \text{ kg} \quad (30)$$

$$m = 4.4 \text{ kg} \pm 4.5\%, \frac{0.2 \text{ kg}}{4.4 \text{ kg}} \cdot 100\% = 4.5\%, \quad (31)$$

Depending on their relationship, when adding, or subtracting measurands the absolute uncertainties can be added, such as in equation (32) where Δ is the absolute uncertainty of the corresponding measurand (Ellison & Williams, 2012).

$$\begin{aligned} (A_{\text{Value}} \pm \Delta A_{\text{Value}}) + (B_{\text{Value}} \pm \Delta B_{\text{Value}}) \\ = (A_{\text{Value}} + B_{\text{Value}}) \pm (\Delta A_{\text{Value}} + \Delta B_{\text{Value}}) \end{aligned} \quad (32)$$

When multiplying and dividing measurands, their relative uncertainties are added, as in equation (33), where ϵ is the relative uncertainty of the corresponding measurand (Ellison & Williams, 2012). When a measurand is raised to a power, the relative uncertainty is used and is multiplied by the power, as in equation (34) (Ellison & Williams, 2012).

$$\begin{aligned} (A_{\text{Value}} \pm \epsilon_{A_{\text{Value}}}) (B_{\text{Value}} \pm \epsilon_{B_{\text{Value}}}) \\ = (A_{\text{Value}} B_{\text{Value}}) \pm (\epsilon_{A_{\text{Value}}} + \epsilon_{B_{\text{Value}}}) \end{aligned} \quad (33)$$

$$(A_{\text{Value}} \pm \epsilon_{A_{\text{Value}}})^n = (A_{\text{Value}}^n \pm n \epsilon_{A_{\text{Value}}}) \quad (34)$$

If a measurand is multiplied by a constant, the absolute uncertainty is multiplied by this constant, whereas the relative uncertainty is not, as in equations (35) and (36) respectively (Ellison & Williams, 2012).

$$c (A_{\text{Value}} \pm \Delta A_{\text{Value}}) = c A_{\text{Value}} \pm c (\Delta A_{\text{Value}}) \quad (35)$$

$$c (A_{\text{Value}} \pm \epsilon_{A_{\text{Value}}}) = c A_{\text{Value}} \pm \epsilon_{A_{\text{Value}}} \quad (36)$$

3 Gimbal Base Actuation

The focus of the investigation was to record accurate gimbal response data for varying frequency and amplitude, gimbal base pitch, and roll actuations. When a drone hovers, pitch and roll are primarily used to maintain position. This means that a gimbal mounted below the drone is subjected to a combination of rotations and translations. The actuations of the gimbal base had to mimic this, but for a single axis rotation at a time, such as drone pitch.

3.1 Drone Hover Performance

Drone hover performance data was processed and analysed in the frequency domain to determine the most significant frequencies and amplitudes for pitch and roll during drone hover. The raw data was taken from a series of flight tests for an undergraduate project (Botha, 2017), where the drone was manually flown indoors. The flight data that used was from a 16 s hover, after take-off.

Figure 13 is the FFT of the drone's pitching rotations during hover. The figure indicates that for low frequencies, below 10.0 Hz, increasingly larger pitching rotations are observed, which are due to the user control inputs, which were infrequent, but resulted in large rotations. Figure 14 is the zoomed FFT of the drone pitching rotations, where rotations in the order of 100 times smaller are observed. The amplitude range for the pitch rotations above 10.0 Hz were determined to be less than 0.07° . The drone roll rotations were nearly identical in magnitude and frequency content to the drone's pitch rotation FFTs. The peak roll magnitude was determined to be less than 0.08° above 10.0 Hz.

The drone that was used had an S500 frame, four EMAX, MT3506 – 650 KV motors and a 3DR PX4 Pixhawk controller. The recorded data indicated that 12 x 3.8 R blades were attached to the drone, with the motors being supplied with 14.25 V at 9 A. Following the motor specifications for the given drone blades' lengths, applied voltage and current, the drone motor specifications indicated that the expected motor speed is 5420 rpm (EMAX, 2018). Given that there are two blades per motor and assuming that the motors are rotating in phase and at a constant speed, the blade pass frequency that was expected to be observed was 180.7 Hz. However, the Pixhawk sensor sample rate was 250.0 Hz, therefore there would be an issue with signal aliasing. Therefore, at this motor speed and sensor sample rate, the blade pass frequency would appear to be 69.3 Hz.

The rotation speed of drone motors varies with drone load, throttle position and manoeuvres that are being done, such as rolling. Therefore, the motor speed was expected to be in the region of 5420 rpm to 9262.5 rpm, the latter being the no-load speed (Chapman, 2012). This corresponded to a blade pass frequency range of 69.3 Hz to 66.3 Hz due to aliasing. It must also be noted that for this sample rate, a motor speed of 9000 rpm corresponds to a measured vibration frequency of 75.0 Hz.

It must also be noted that the Pixhawk was mounted onto the same vibration isolation pads that the gimbal is mounted onto when slung underneath the drone.

Thus, the vibrations that are observed, although small, are still being observed by a device that is on isolation pads.

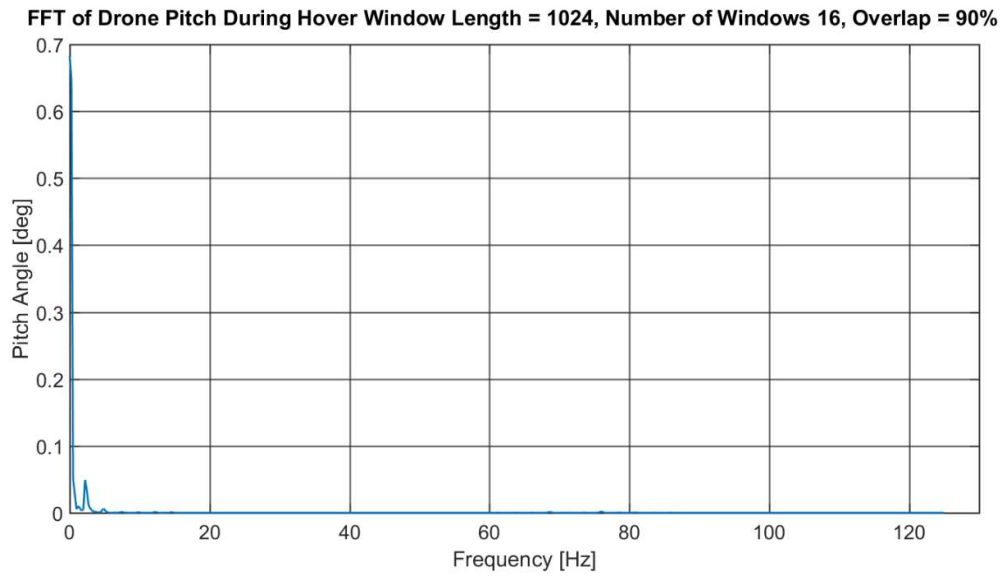


Figure 13. The FFT of the drone's pitch angle during a hover test.

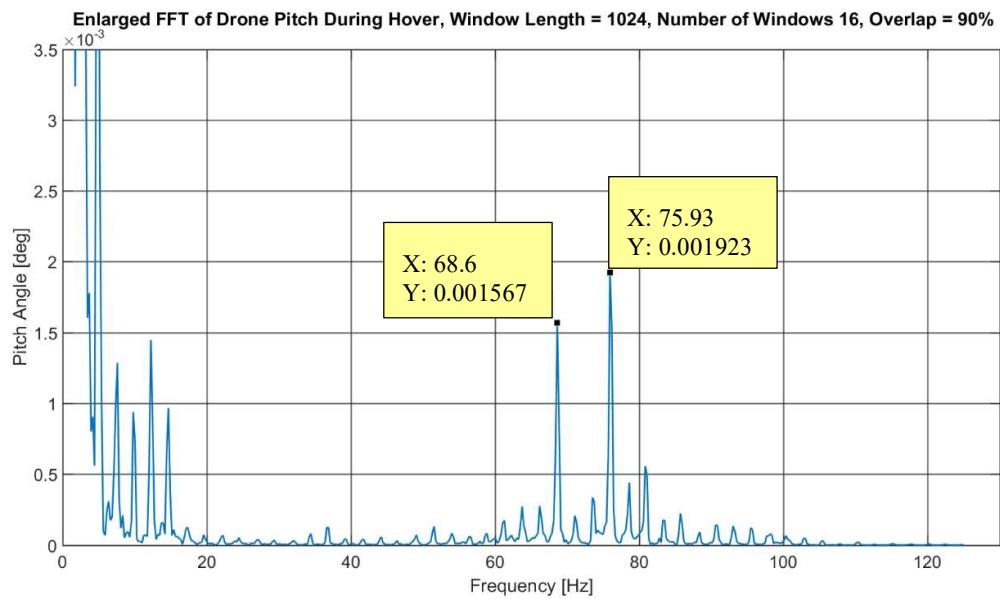


Figure 14. The zoomed FFT of the drones pitch angle during hover.

The frequency range that would be investigated was limited to range from 10.0 Hz to 200.0 Hz. The lower frequency limit was due to the actuation system, discussed in section 3.2, while the upper limit was due to the highest sample rate of the measurement system at 2.0 kHz, which will be discussed in chapter 4.

3.2 Gimbal Base Actuation System

To produce the gimbal angular responses, a system had to be designed which could actuate the gimbal base at different frequencies and amplitudes, in a manner similar to a drone rotating on one axis. The structure had to be rigid enough to prevent the disturbance frame from introducing support structure oscillations into the measured gimbal responses.

The aim was to see the gimbal's progression from a region of good performance, into a region of poor performance. This meant the starting frequency would need to be relatively low, between 5.0 Hz to 10.0 Hz. With the observations of possible structural and blade pass frequencies from section 3.1, the aim was to investigate up to a range of 200.0 Hz.

From these requirements, it was clear that the most accurate way of producing the actuation frequencies and large enough actuation range was by using a shaker. Other displacement methods of actuation were investigated, such as using electric motors for angular oscillations. However, shakers were a more established method of actuation, especially where precise actuation frequencies were required. Therefore, the shaker that was selected was a type 4806, Brüel & Kjær shaker (Brüel & Kjær, 2014).

The gimbal was an IMP BLDC 2-Axis gimbal, with GBM 2804 019-100T BLDC motors, supplied by RC Timer (RC Timer, 2017). The only change to the gimbal frame structure was the lengthening of the horizontal mounting arm to 100 mm, as indicated in Figure 15. Note that the gimbal shown in Figure 15 is the updated model, as the gimbal that was used was purchased for a previous project and is not manufactured anymore. Critically, though, the motors are still the same. The gimbal controller was a BaseCam Electronics SimpleBGC 32-bit controller with gimbal and gimbal frame IMUs (BaseCam, 2014). It must be noted that the weight of the gimbal was 150 g, excluding the device mount load.

The gimbal was allowed to respond in both roll and pitch simultaneously at all times. Preventing the gimbal motors from rotating meant altering the gimbal's frame, or operation. This would have interfered with and altered the gimbal's true performance. As the aim of the study was to investigate the gimbal's true responses, altering its operation was not an option.

As stated above, the gimbal needed to be actuated in a manner similar to the actuations produced by a drone. Therefore, the gimbal needed to be located below the centre of rotation, as it would when mounted under a drone. An actuating plate was designed, as seen in Figure 16, to which the gimbal and shaker would be connected to. The plate would be fastened to a shaft, passing through the centre of rotation in Figure 16. Two bearings, mounted to a support frame, would then allow

the shaft and actuation plate assembly to rotate about the centre of rotation, indicated in Figure 16. The gimbal would then be mounted below the centre of rotation on the actuation plate. The distance L is the distance from the centre of mass of the gimbal, to the mounting point on the drone. This distance was measured and found to be 205 mm.

The 122.5 mm distance from the centre of rotation, to the shaker-actuation plate connecting point, is a minimum distance. If the shaker was mounted closer to the centre of rotation, the gimbal would knock the shaker for the largest shaker peak-to-peak displacement of 8 mm (Bruel & Kjaer, 2014).



Figure 15. A Photograph of the current IMP 2-Axis BLDC gimbal supplied by RC Timer (RC Timer, 2017).

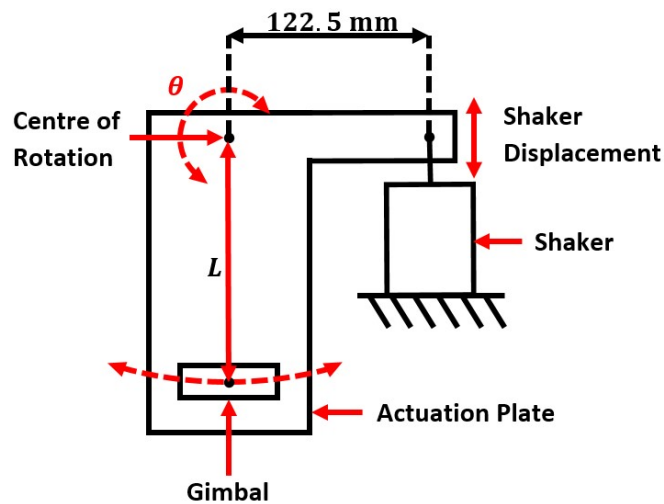


Figure 16. A box and line diagram of the actuation plate and shaker. Together, these two components would actuate the gimbal.

The equation, which describes the gimbal's vertical displacement, can be found in equation (37). Note, the angle theta is the angle of rotation of the actuation plate, and the displacement of the gimbal is measured from the position where the centre of gravity of the gimbal is below and in line with the centre of rotation.

A support frame was manufactured and mounted to a main support stand, which could be bolted down, as seen in Figure 17. The actuation plate and gimbal could then be mounted to this support frame. The additional component mounted at the top of the actuation plate is part of the input measurement system, and is discussed in chapter 4.

$$d_{\text{gimbal}} = L (1 - \cos \theta) \quad (37)$$

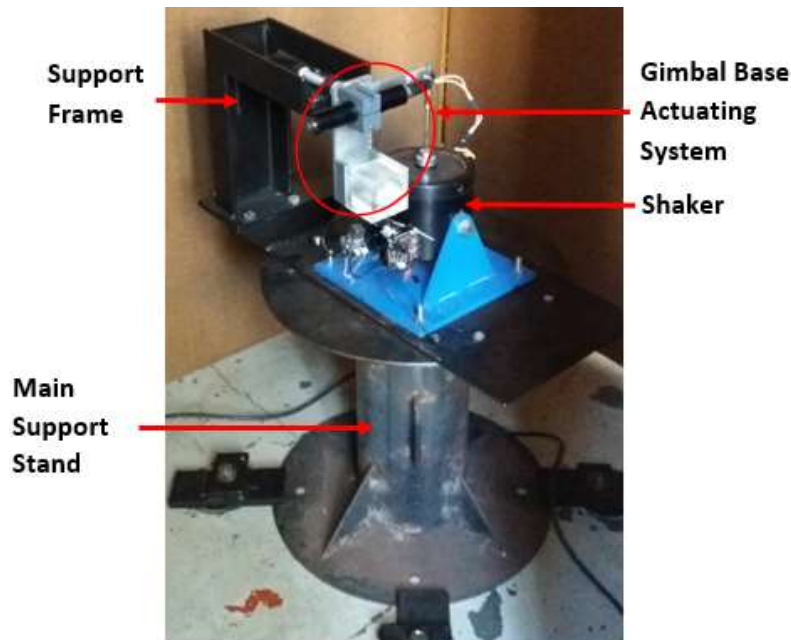


Figure 17. Main support stand, support frame, shaker and actuation plate.

More detailed photographs of the actuation system, gimbal and setup can be found in sections 4.1, 5.1, 5.2, 5.3 and 5.4.3. The technical drawings and masses of the rotating actuation assembly and components can be found in Appendix A.

4 Measurement System

This chapter covers the design of the system that measures the gimbal base actuations and gimbal responses. Because of the nature of the experiments that were to be carried out, the measurement system had to be able to track high-frequency gimbal base actuations and the corresponding gimbal responses, while maintaining a high degree of accuracy.

4.1 Measurement Systems and Devices Considered

The goal, during the process of deciding on and designing the measurement system, was to find a way of producing accurate measurements that were reliable and repeatable. In addition, the measurement system had to be robust.

To measure the actuation angle, rotary encoders were considered. However, it was determined that it would be simpler to use a system that could measure the displacement of the actuation plate arm, which was connected to the shaker. The actuation angle could then be inferred, by using the known distance from the measurement point, to the centre of rotation.

Two methods to infer the angular displacements and responses of the gimbal were considered. The first, was to use accelerometers, mounted on key locations of the actuation structure and gimbal. Integration in the frequency domain could then be used to infer the angular displacements of the actuation structure and responses of the gimbal. The second method, was to use lasers mounted to the actuating structure and gimbal. The displacement of the laser dots could be measured and used to infer the angular displacements and gimbal responses.

For the first method, the shaker displacement and actuation plate rotation could be inferred by mounting an accelerometer above the shaker. As stated above, this could be achieved through frequency domain integration of the acceleration data. The gimbal, however, is not limited to a single axis of rotation. Therefore, there was a possibility that the gimbal accelerometer's orientation could be altered from the required measurement direction. If the accelerometer's roll orientation was slightly altered, the inferred gimbal pitch rotation would be incorrect. The device mount, which is shown in Figure 18, was connected to the roll motor. Therefore, there was a high likelihood that the accelerometer roll orientation would be altered.

Therefore, when compared to measuring the displacement of laser dots, the accelerometer measurement system was deemed to be less robust.

For the second method, lasers were mounted to the actuating structure and gimbal, as seen in Figure 18 and Figure 19. To measure the displacement of each laser dot, a Position Sensitive Photodiode (PSD) was considered, as seen in Figure 20 (Thorlabs, 2017). A PSD determines the position of a laser dot on its surface, using the voltage potentials of light-sensitive components within the PSD. Due to purchase and import costs, as well as the time delay for importing, the use of a PSD system was not viable.

Note, the reference laser in Figure 18 is mounted over the actuation centre of rotation. The ballast weight on top of the gimbal laser holder was necessary to shift the mass centre of the gimbal in line with all the motors' axes of rotation and the gimbal's fixed yaw axis of rotation.

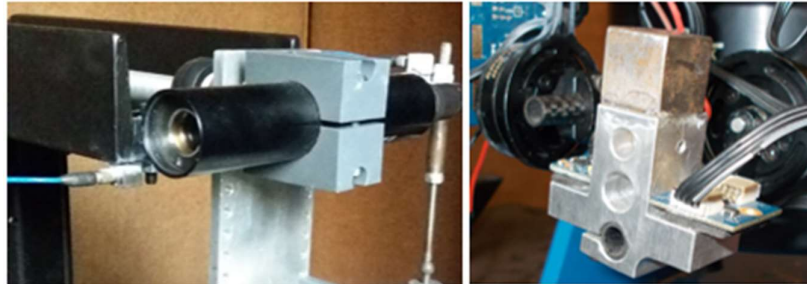


Figure 18. The reference laser in a clasp, mounted over the actuation centre of rotation (Left) and device mount laser holder with ballast block on top (Right).

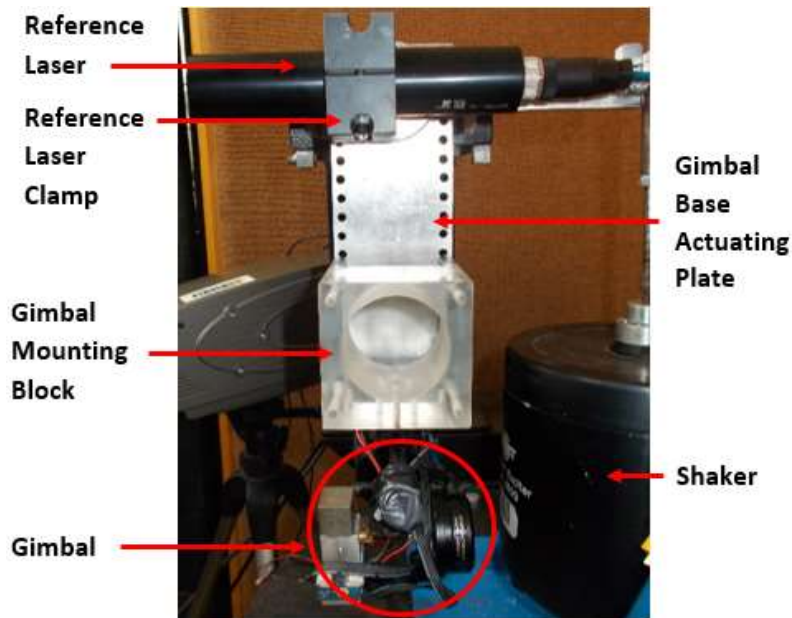


Figure 19. Side photograph of the reference laser in its clamp, the gimbal base actuation plate, the plastic block which connects the gimbal to the actuation plate, the gimbal and the shaker.

Two Olympus iSpeed 3 TR cameras and laser target surfaces were used instead to capture the laser dots' displacements for post processing. Although each camera would only be monitoring a single laser, they would be triggered by the same signal. Functions written in Matlab, discussed in section 4.5, would then be used to track

each laser dot's displacement between images, and infer the corresponding gimbal base actuations and gimbal responses. The delay between the two cameras storing their first images and the uncertainty this introduces is discussed in section 5.4.1.

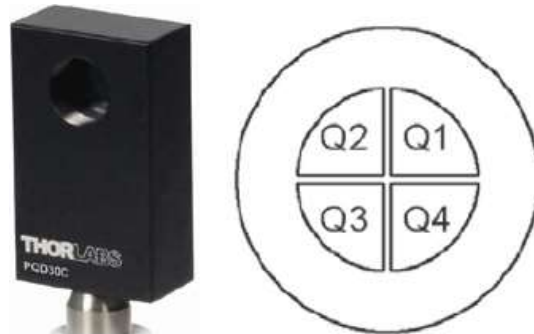


Figure 20. A Position Sensitive Photodiode, or PSD, (Left) and the quadrants of the PSD used in determining the centroid of a laser dot on the surface of the photodiode (Right) (Thorlabs, 2017).

The laser that was mounted to the actuation plate was the 5 mW, 635 nm wavelength, 3mRad maximum bore sight error, FP-LR-635-5-C-F laser from Laser Components, with an adjustable focus up to 200 m (Laser Components (UK), 2017). Due to weight and size limitations, the laser mounted to the gimbal had to be small, so a 5 mW class 3a red laser was used, as seen in Figure 21, which had a 0.5 mrad - 1 mrad bore sight error.

The technical drawing and mass of the device mount laser holder, can be found in Appendix A. As stated in section 3.2, the mass of the gimbal, without the device mount, is 150 g.



Figure 21. The 5mW, class 3a laser that was mounted to the gimbal device mount.

4.2 Linear System Assumption

A crucial part of the measuring of the gimbal's performance was the assumption of the type of systems the gimbal and actuation system were. By the equation which defined the gimbal actuation, as seen in equation (37) in section 3.2, it was clear the actuation was nonlinear. The gimbal operation was known to be nonlinear by its operation. Motor friction, flexure of the gimbal frame and IMU resolution, to name a few, would cause the gimbal to respond in a nonlinear way (Johansson, 2012).

The modelling of nonlinear systems, as Linear Time Invariant (LTI) systems, has been used by control systems engineers in the design of robust controllers (Mäkilä, 2006), (Pintelon, et al., 2013). By designing for the worst-case scenario, the effect of the inaccuracies of the LTI modelling of a nonlinear system can be reduced. An example of this is the IMP BLDC 2-Axis gimbal, which is controlled with a PID controller, which is based on a linearized model of the gimbal.

Therefore, based on the large number of variables that affect the gimbal's performance and the complexity of their interactions, the gimbal and actuation system were assumed to approximate a LTI system. By doing this, though, it was understood that any nonlinear dynamics would not be adequately reflected in the results.

However, similar to robust controller design and as stated in section 1.1, the focus is on capturing the peak gimbal responses. This corresponds to the worst-case scenario, where the gimbal constantly responds with the largest measured amplitude. Therefore, when the nonlinearities are compared to this response, it is assumed they do not need to be taken into account.

4.3 Measuring the Gimbal Base Actuation

The gimbal base actuation plate, discussed in section 3.2, rotates when the gimbal base is being actuated. By mounting a reference laser over the centre of rotation, as seen in Figure 18, the rotations can be projected onto a target surface and converted into a linear laser dot displacement, see Figure 22.

By capturing this linear displacement with a high-speed camera, the displacements can be used to infer the actuation angle by using the right angle triangle rule, see equation (38), and assuming that:

1. the measured distance from the target surface to the centre of rotation of the reference laser is exact.
2. at the equilibrium position, the reference laser beam is perpendicular to the target surface.
3. the reference laser pitches by an equal angle for both up and down swings.

The result of these assumptions can be found in Figure 22, where the angular actuation between measurement points in time, is inferred by the displacement of the laser dot.

The term “equilibrium” in point 2 is referring to the position of the laser dot when the laser and laser beam are horizontal. Therefore, in Figure 22, this is the black dotted line and its contact point on the target surface.

The sources of error and uncertainty, including the above assumptions, in the system, and their effects on the accuracy in the determination of the actuation angle, are discussed in Appendix D. The distance $D_{\text{Reference}}$ at the end of section 4.7.

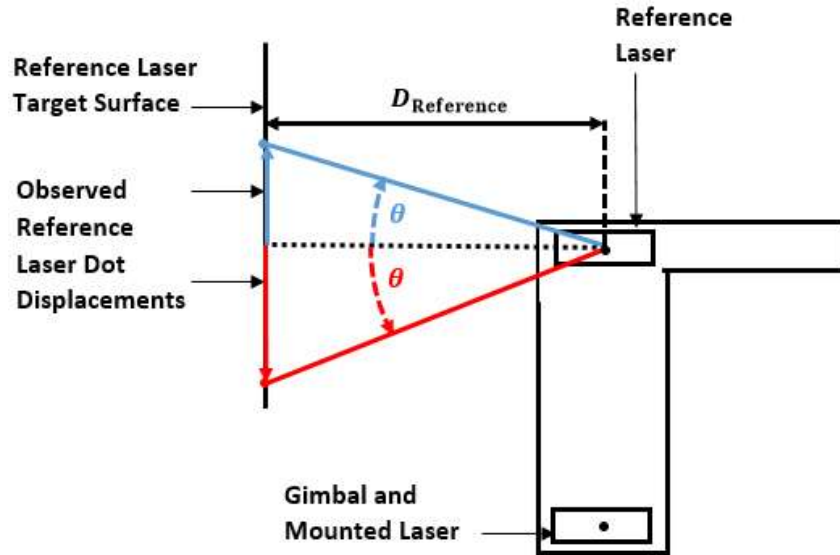


Figure 22. A box and line example of the gimbal base actuation system, with the reference laser mounted on the centre of rotation.

$$\theta_{\text{Actuation}} = \tan^{-1} \left(\frac{P_{\text{Reference_Max}} - P_{\text{Reference_Mean}}}{D_{\text{Reference}}} \right) \quad (38)$$

4.4 Measuring Gimbal Device Mount Responses

Gimbal performance is determined by its ability to reject varying frequency and amplitude, gimbal base disturbances, such as drone pitching or rolling. Therefore, by how much the gimbal amplifies, or attenuates, the effect of the disturbances on the gimbal base.

If a gimbal is operating ideally, it will counter the rotations to which its base is being subjected to exactly. Real-world gimbals, however, are prone to sensor drift and angular resolution errors, which prevent the device mount from counter-rotating by the same angle as the gimbal base rotation. This property can be used to measure how the gimbal performance degrades by comparing the actual response, to the expected ideal case scenario.

The gimbal laser was fastened in a laser holder, which was clamped to the gimbal device mount, see Figure 23. By placing the laser in a strategic position, such as in the upper laser hole as seen in Figure 23; the gimbal's roll responses would not directly affect the position of the laser dot. The reason being that the upper laser hole was designed to be in line with the axis of rotation of the roll motor. Thus, the only laser movement, as a result of the gimbal roll, would be from laser bore sight error. Laser bore sight error is the misalignment of the laser beam and the laser barrel centre axis, and is discussed in Appendix D.1.7.

Note, in Figure 23 there is a 26 g, mild steel block on top of the gimbal laser holder, which was needed to balance the gimbal.

A third hole was added below the upper laser hole to reduce the weight of the laser mount and to make it simpler to balance the gimbal, while the lower hole was to be used as a clasp to anchor the device mount laser holder to the device mount.

The gimbal base actuation plate, discussed in section 3.2, rotates and translates the gimbal between two peak positions. As shown in section 3.2 this displacement would cause the gimbal laser dot to have a small displacement, if the gimbal is operating ideally.

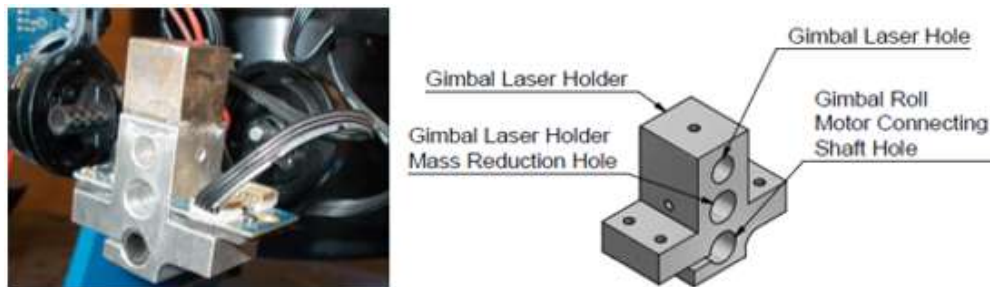


Figure 23. Device mount laser holder (Left) with IMU mounted on the right side and magnetometer mounted on the left side. Device mount with feature labels (Right).

Figure 24 and Figure 25 are examples of ideal gimbal operation for a forward and backswing of the actuation plate, respectively. As the gimbal operation is not ideal, though, the gimbal laser beam lines are expected to diverge from the ideal case, as shown in Figure 26 and Figure 27 for the forward swing and backswing peak positions, respectively.

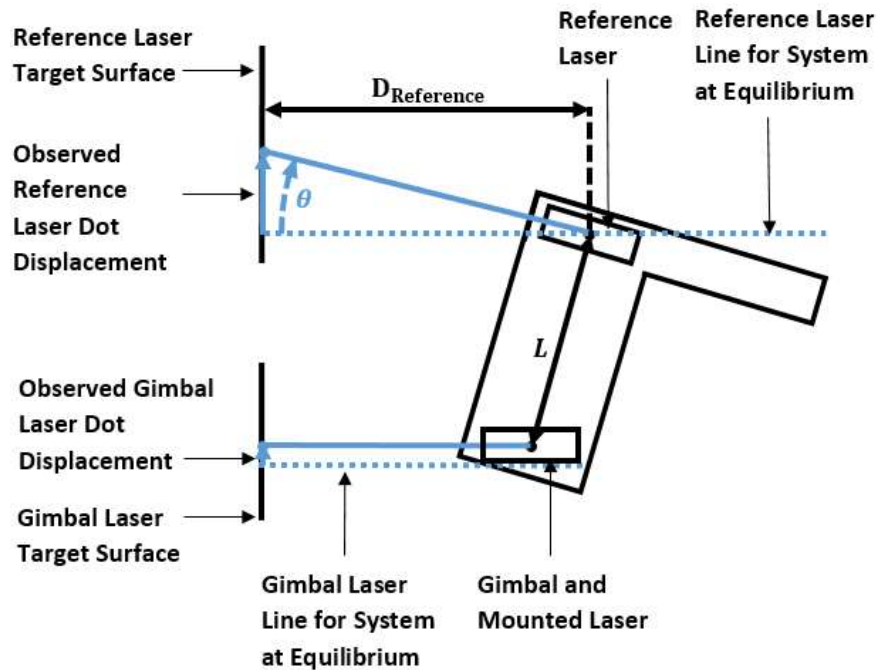


Figure 24. An example of ideal gimbal operation when swung forward. The gimbal and reference laser are mounted to the actuation plate.

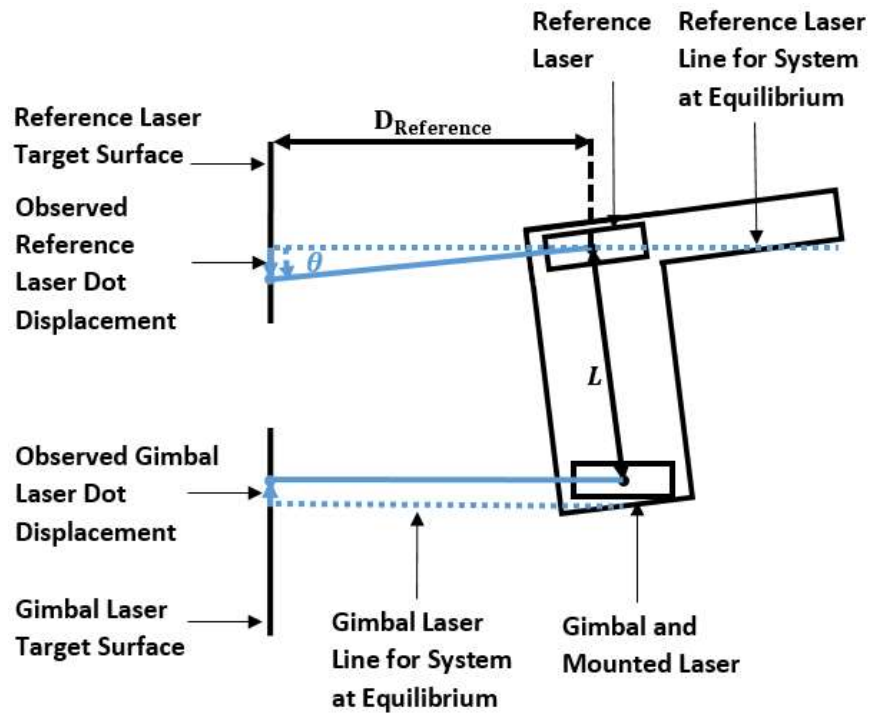


Figure 25. An example of ideal gimbal operation when swung backward. The gimbal and reference laser are mounted to the actuation plate.

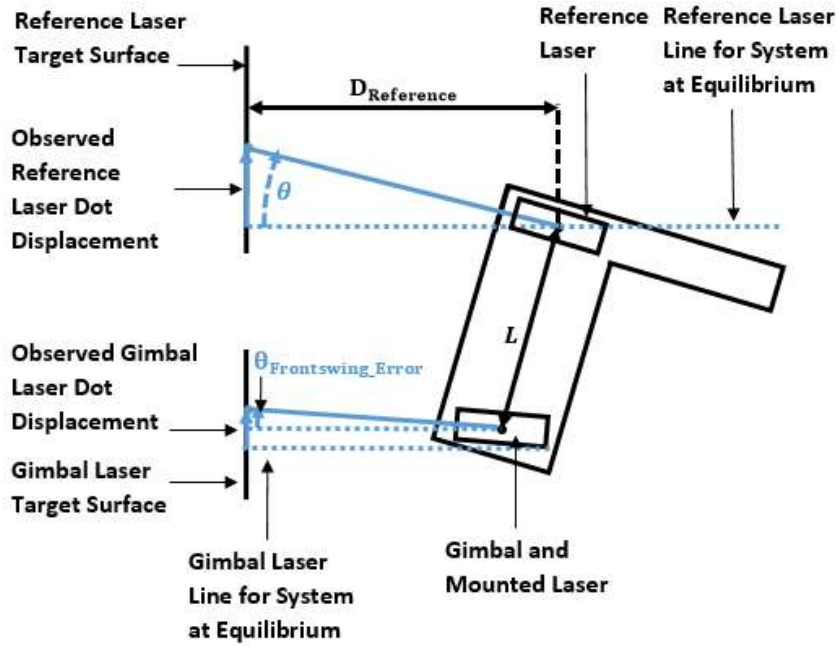


Figure 26. An example of a non-ideal operation scenario of the gimbal where the device mount has not been counter rotated by the same angle as the actuation plate forward swing.

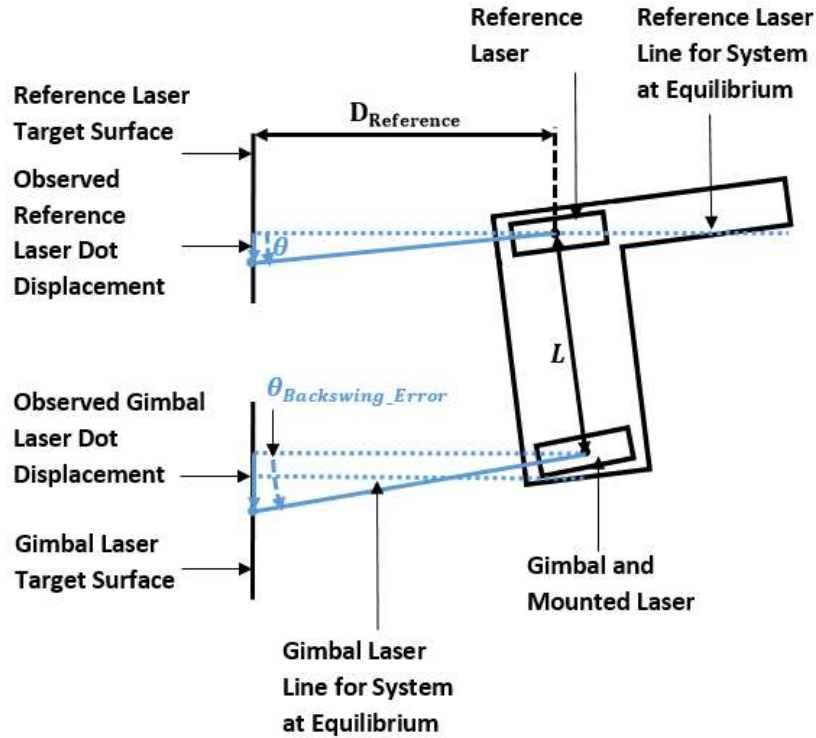


Figure 27. An example of a non-ideal operation scenario of the gimbal where the device mount has not been counter rotated by the same angle as the actuation plate backswing.

Determining the pose error of the device mount, by using the displacement from equilibrium, is possible, but requires the displacement of the device mount laser dot from the ideal position at system equilibrium. As the gimbal is operating under non-ideal conditions, the device mount will not be orientated at a perfectly horizontal level, nor will the actuation plate be at equilibrium in the vertical position

Therefore, assuming the change in distance of the gimbal to target surface during actuation is negligible, it can be assumed that the gimbal is stationary and is not translated, or rotated by the actuation plate. Therefore, the resulting gimbal laser movements are from the gimbal motors rotating, as seen in Figure 28. Note that the distance D_{Gimbal} is defined at the end of section 4.7.

The horizontal dotted line is the equilibrium position of the system. As stated above, this line is only perfectly horizontal under ideal conditions. Therefore, the position of the reference laser and gimbal laser at equilibrium cannot be used. This having been said, however, the equilibrium position can be estimated by assuming that the mean position of the laser dot, for a given test, is the equilibrium position of the laser dot for that test.

To determine the gimbal response, equation (39) is used, where the mean gimbal laser dot's position is deducted from the maximum amplitude found. The resulting method for quantifying the gimbal response means that for good gimbal operation, the determined angle would be small, but for poor gimbal performance the determined angle would be large. If the displacement of the gimbal laser dot did not oscillate about an average, but drifted during the oscillations, the data would be detrended. Therefore, the average displacement would be zero.

As the examples indicate, the above setups would be used to measure the gimbal's responses to pitch inputs. To measure the gimbal's pitch responses to roll inputs, the gimbal would be dismounted, rotated by 90° and then mounted again. The methods discussed above would then be used again.

Note that the largest measured reference and gimbal laser dot displacements are used in the determination of the magnitude of the actuation and response. A sample calculation is provided in section 6.4 for clarity. The limits and corresponding measurement uncertainty that the displacement assumptions introduce, are discussed in Appendix D.

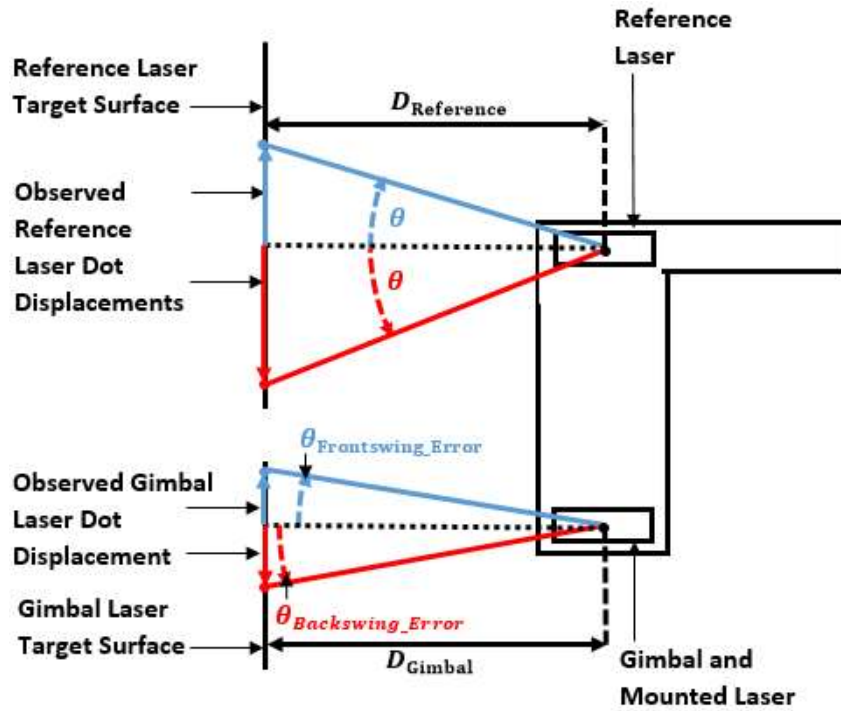


Figure 28. An example of a peak-to-peak gimbal base rotation, with device mount response errors and what the right angle triangle assumption implies.

$$\theta_{\text{Error}} = \tan^{-1} \left(\frac{P_{\text{Gimbal_Max}} - P_{\text{Gimbal_Mean}}}{D_{\text{Gimbal}}} \right) \quad (39)$$

$$G = \left| \frac{\theta_{\text{Error}}}{\theta_{\text{Actuation}}} \right| \quad (40)$$

The resulting expected reference and ideal gimbal laser dot displacement profiles for a 10.0 Hz, 8 mm peak-to-peak shaker actuation can be found in Figure 29. The gimbal and reference laser dot displacements are measured against the left y-axis, and are indicated as red squares and blue dashes, respectively. It must be stressed that in this example the gimbal laser dot displacements are purely due to the vertical displacements of the gimbal, as in Figure 24 and Figure 25. The gimbal laser dot's peak displacement in Figure 29 is 0.1092 mm, while the reference laser dot's peak displacement is 52.6 mm. This means that the displacements of the gimbal laser dot, due to the vertical gimbal displacement, can be ignored. This implies that any gimbal laser dot displacements in the experiments are considered to come from the gimbal's motor rotations only.

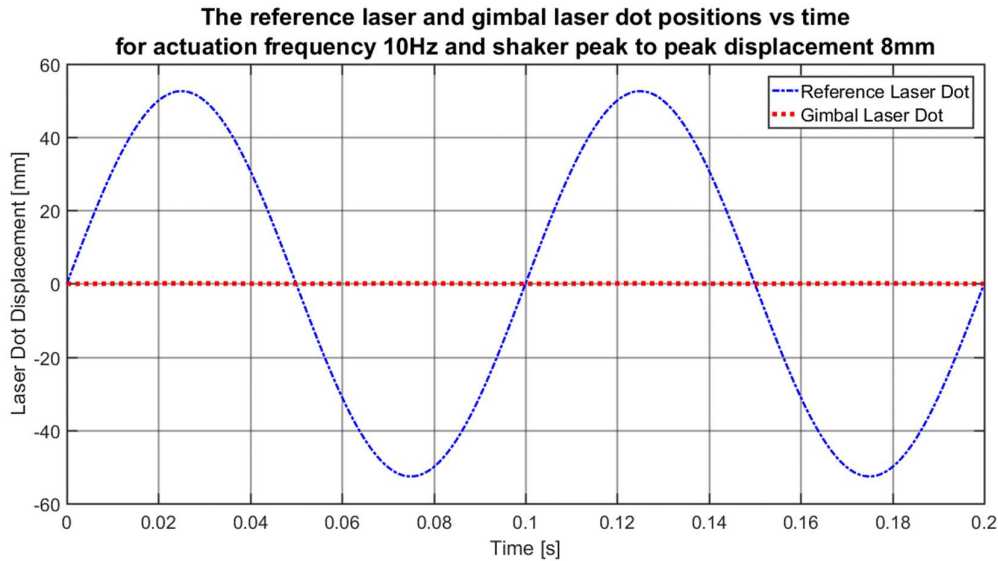


Figure 29. The expected reference laser and gimbal laser dot displacement vs time plots for gimbal pitch and roll responses.

4.5 Laser Dot Displacement Measurement

As stated in section 4.1, it was decided that two cameras would be used to capture the reference laser dot and gimbal laser dot displacements. The laser dot's displacement between images would then be determined by triangulation in each image, relative to an in-image axis system produced by a fixed checkerboard pattern. The pattern is provided in Appendix A, with its dimensions.

To be able to triangulate the laser dot's position in millimetres in each image, the camera's intrinsic and extrinsic parameters needed to be known, which required a camera calibration. A series of photographs would be taken of the checker-board pattern, at different angles relative to the camera, providing enough data for the calibration algorithms to determine the camera parameters.

The key to determining the laser dot displacement lay in finding the same point within the laser dot, and then tracking this feature's displacement through the sequence of photographs. Since the reference laser was not a Gaussian laser, Gaussian centroid detection algorithms could not be used. However, the possibility of using edge-detection algorithms to track the laser dot's movements were investigated, when using the reference laser under defocused conditions. An example of the defocused laser and the imperfections in the laser dot sight, can be found in Figure 30.

In order to use the algorithm, threshold filtering was required, which meant sampling the laser dot pixel intensities from the laser images. This meant that there was a possibility of removing portions of the laser dot from the image. This was a concern as it was important to try and keep the image as unaltered as possible, in

order to preserve the true shape of the laser dot in the image, regardless of quality of laser dot shape or light intensity, as this contained the true centroid.

With this in mind, the Barycentre method was then chosen as the algorithm to track the displacement of the laser dot. This method was computationally expensive, though.

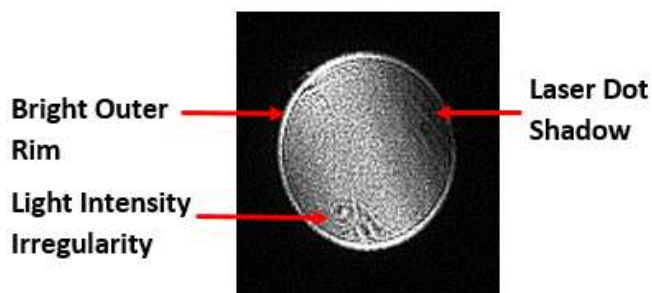


Figure 30. The defocused FP-LR-635-1-C-F laser dot with site shading on the upper right, brighter-than-centre outer rim and laser dot irregularities. Note that the image provided of the laser dot is cropped and enlarged.

Therefore, the tracking of the laser dot in each image was achieved by means of two steps.

1. Finding an initial rough laser centroid site and creating a search block around it.
2. Determining the Barycentre of the laser centre within the search block.

The first step was necessary as 3197 photographs would be taken per experiment, and these would take time to process. To reduce the processing time the functions “regionprops” and “imfindcircles” were used to provide close and quick guesses to the laser centroid in an image, see Figure 31.

“Regionprops” had the ability to determine the weighted centroids of multiple in-image features, but was affected by pixel intensity noise, often found around the laser site. “Imfindcircles” specifically searched for circular-shaped objects in the image, of a radius supplied by either the function “regionprops”, or by a user specified radius range. Therefore, “imfindcircles” was used to average out the guessed centroid of the laser dot site.

Once the initial laser centroid guess was determined, a search box was established with sides placed 1.5 times the average radius, determined by “regionprops” and “imfindcircles”, of the found circle’s centroid, as seen in Figure 31. Although both the aforementioned functions could determine the centroids of in-image feature objects on a subpixel level, it was found that a higher accuracy could be achieved by then determining the Barycentre of the feature within the search box. How this was tested and determined is discussed in section 4.7.

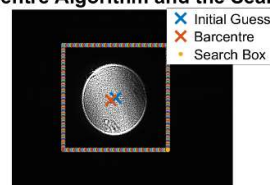
The Barycentre was determined by excluding the pixels with pixel intensities below the maximum background pixel intensity when the lasers were off, which was determined before the experiment. Once the Barycentre was determined, the centroid pixel co-ordinates were then converted into world co-ordinates using the Matlab function "pointsToWorld".

Initial tests revealed that the algorithm was still struggling to track the changing position of the laser reliably, as the Barycentre method was significantly affected by the high-intensity pixels situated on the rim of the laser dot site. These, in addition to laser dot shape changing as it displaced, prevented the algorithm from reliably and accurately finding the laser dot centre, or any other feature within the laser dot, see Figure 31.

**The Guessed Laser Centroid by the Functions
"Regionprops" and "Imfindcircles"**



**The Refined Laser Centroid by
the Barycentre Algorithm and the Search Box**



**The Guessed Laser Centroid by the Functions
"Regionprops" and "Imfindcircles"**



**The Refined Laser Centroid by
the Barycentre Algorithm and the Search Box**

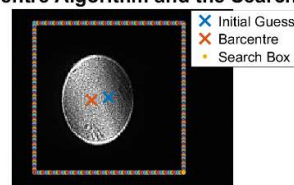


Figure 31. An example of the process of trying to find the same position in the defocused reference laser between two different positions (Above and Below). The top two photographs are of the reference laser near the middle of the image, while the bottom two photographs show the reference laser dot near the edge of the image. Note that the photographs have been zoomed significantly. The top and bottom left images show the initial guesses at the laser centroid using the Matlab functions "regionprops" and "imfindcircles". The search box is then established around the suspected laser centroid site and then the Barycentre algorithm is used within the box (Top and Bottom Right). The background pixel intensity, determined before the laser is turned on, is used to determine which pixels do not need to be taken into account when finding the Barycentre. Thus, any pixel intensity flaring observed around the laser centroid, will still be taken into account and not discarded. Note the compression of the laser dot as it draws closer to the edge of the image. This is due to the angle from which the camera is observing the target surface.

To reduce the effect of the laser dot shape changes, the pixel intensity changes and laser dot imperfections, the option of using a focused and brighter, but smaller laser dot was considered. The better consistency of the pixel intensities would improve the initial laser centroid guess. The smaller size would also make it more likely that the same position in the laser dot would be found, thus reducing the uncertainty of the determined laser dot position and displacement. There were concerns, though,

that changes in pixel intensities in a smaller dot would cause the algorithm to struggle to track a laser dot feature consistently.

Therefore, simulations were carried out with a simulated focused laser dot form, but with increasing average and standard deviation image pixel intensities near and around the laser dot site. With varying image pixel intensity, the algorithm was still able to determine the simulated laser centroid with relatively good results, see Figure 32.

The examples in Figure 32 indicated that for significant differences in pixel intensities, such as in shown simulation 3 of Figure 32, the algorithm began to struggle to accurately find the centroid of the laser dot site. It was clear that for greater pixel intensity variation near the true centroid of the laser, the greater the negative effect on the algorithm accuracy.

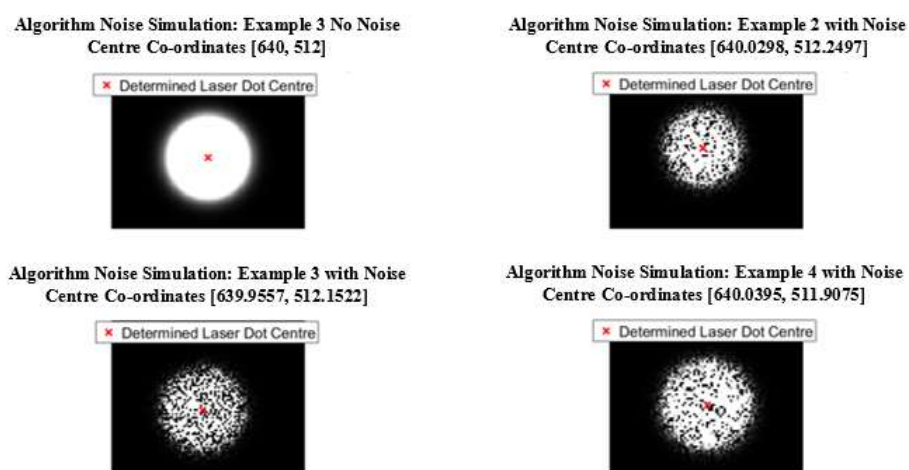


Figure 32. Laser dot centroid tracking simulations on a Gaussian simulated dot with normally distributed, but varying image pixel intensity. Note that the original point co-ordinates in pixels were [640, 512] and that the images are significantly enlarged. The figures show how the algorithm is able to perform under varying degrees of pixel intensity noise and pixel noise distribution.

Therefore, if a region of the laser dot site were affected, such that the brightest pixels were not on the true laser centroid, the determined centre would be pushed away from the darker regions, or pulled towards lighter regions. The findings of these simulations highlighted and validated the need to use a small, focused laser dot with a small region of high pixel intensity valued pixels, see Figure 33.

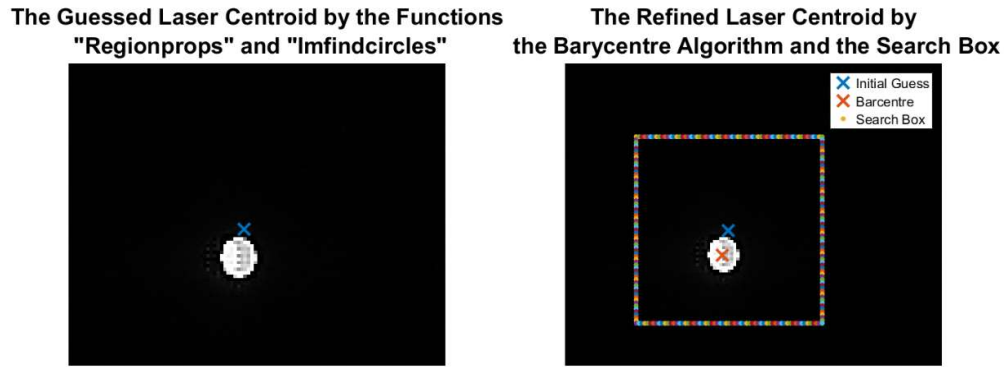


Figure 33. An example of the process used in finding an initial guess at the focused laser centroid using the Matlab functions "regionprops" and "imfindcircles" (Left). The search box is established around the suspected laser centroid site and then the Barycentre algorithm is used within the box. The background pixel intensity, determined before the laser is turned on, is used to determine which pixels do not need to be taken into account when finding the Barycentre. Thus, the faint pixel intensity flaring, observed around the laser centroid, was still taken into account and not discarded. Note that the images provided above have been zoomed significantly.

4.6 Achievable Camera Angular Resolution

To capture the gimbal's responses, the image resolution had to allow the laser dot tracking system to be able to measure gimbal responses and actuation angles to an accuracy better than the gimbal's, when its base is being displaced. As no gimbal pose accuracy data was available for gimbals under dynamic gimbal base conditions, it was decided to use the known pose accuracies of heliostats, known to be below 1 mrad under ideal conditions (Chong, Wong, Siaw, Ng, Yew, Liam, Lim, Lau, 2009), as a benchmark. With this in mind, it was decided to aim to achieve a measurement system accuracy five times more accurate than 1mrad, thus an accuracy of 0.2 mrad.

Figure 34 is an example of the correlation between the required subpixel angular resolution, shown as the incremental laser pitch rotation, and the corresponding subpixel image resolution required in the image y-axis to achieve this, shown as the horizontal dashed lines. The distance between the dashed lines indicates the smallest distance that can be measured, or the subpixel image resolution. Note, $\alpha_{\text{Initial_Guess}}$ is the benchmark accuracy of 0.2 mrad stated above. $\text{Image_Re}_{\text{Sub_pixel}@\text{fps}}$ is the subpixel image resolution at a given frame rate and is used in Appendix C.

In order to achieve this subpixel resolution, the required distance of each camera from the target surface needed to be determined, which is covered in Appendix C. It was found, though, that the theoretical distances required for the cameras from Appendix C were too close to the target surfaces to capture enough calibration blocks to perform an adequate camera calibration. Therefore, the cameras were shifted back until enough calibration blocks could be captured for a camera calibration.

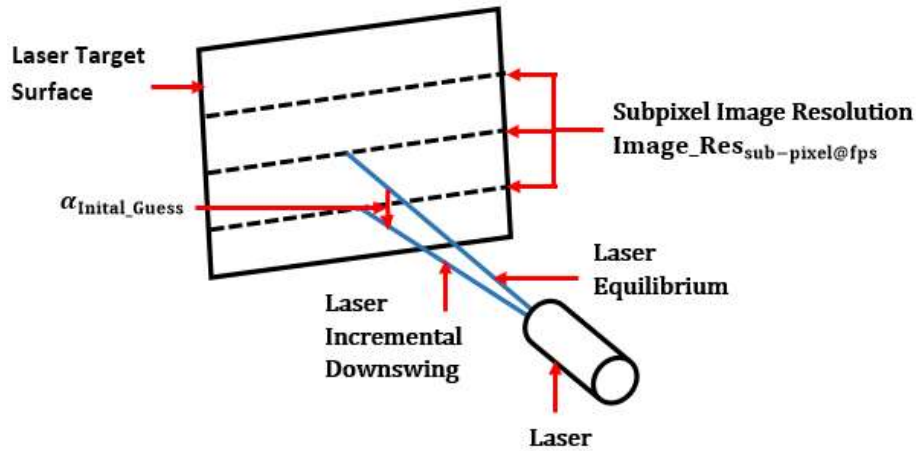


Figure 34. An example of the correlation between the angular subpixel resolution and the image subpixel resolution. To achieve the required angular subpixel resolution of $\alpha_{Initial_Guess}$, indicated as the incremental pitch rotation of the laser, an image subpixel resolution of $Image_Res_{sub-pixel@fps}$ is required for the image y-axis, which is shown as the dashed lines on the target surface. The distance between the dashed lines indicate the smallest displacement that can be measured by the system. Note that this approach applies to both the reference laser and the gimbal laser and that the figure is not to scale.

For the camera operating at 2000fps, the distance to the target surface was 486.5 mm, resulting in a theoretical y-axis angular resolution of 0.3 mrad. For the camera operating at 10 000fps, the distance to target surface was 453.5 mm, resulting in a theoretical y-axis angular resolution of 0.7 mrad. Although not as small as the initial angular resolution guess in equation (58), the angular accuracies predicted were close enough.

It must be noted that the total recording time that could be stored for each camera, was dependant on the internal memory available on the camera memory buffer. Operating at 10 000fps a total of 1924 photographs could be stored, which equated to a recording time of 0.1924 s. Operating at 2000fps a total of 1223 photographs could be stored, which equated to a recording time of 0.6115 s. However, when using both sets of data to determine the gain, only 384 samples from the 2000fps data set could be used. Where the samples were not taken at the same point in time, interpolation was used.

One of the implications of these limitations was that the uncertainty of the lower frequency measurements would be greater than the higher frequency measurements. In addition, the uncertainty for the 2000fps measurements would be higher than the 10 000fps measurements.

4.7 Laser Dot Displacement Tracking Verification Experiments

To use the measurement system, the uncertainty of its measurements needed to be determined, which required accuracy verification experiments. Therefore, two sets of experiments were carried out per camera frame rate, where the algorithm accuracy was determined for the specific frame rates, image axes and frame rate-specific camera-to-target distances required, from section 4.6. The reference laser

was mounted to a turret mill bed, which was accurate to the nearest 0.02 mm, and displaced along the axis parallel to the calibration board x-axis, or y-axis, depending on the axis being tested, as seen in Figure 35. Note that the positive x-axis direction of the calibration board in Figure 35 is from the left side of the board to the right. The positive y-axis direction is from the top of the board to the bottom.

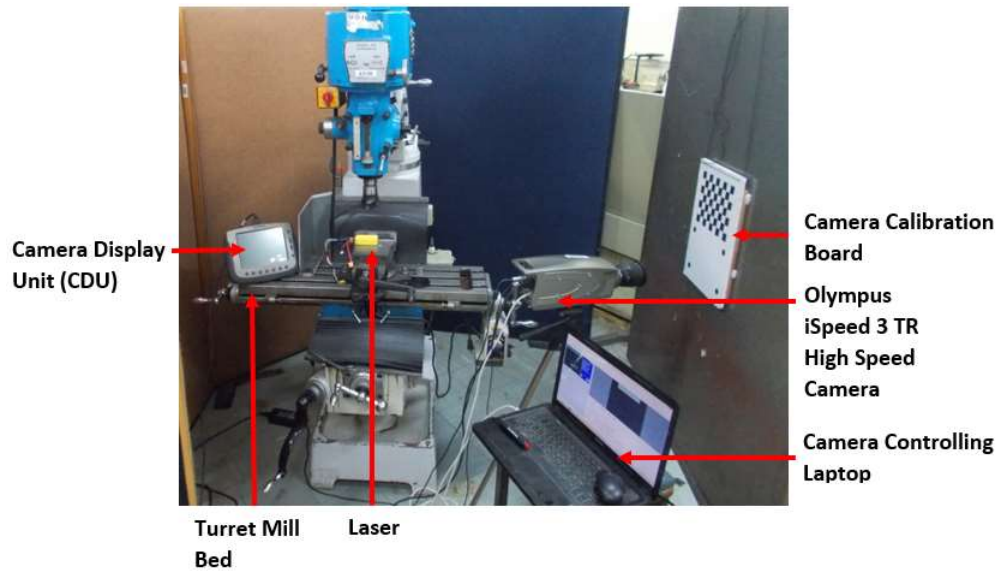


Figure 35. The laser dot tracking accuracy verification experiment setup for the 2000fps tests.

It was understood that the accuracy of the algorithm depended on the camera distance and angle-to-target surface, the resolution of the image and the position of the laser dot in the camera region of focus.

The last variable meant that the accuracy of the algorithm would not just change with the quality of focus of the image, but with the position of the laser dot within the region of focus. Therefore, for simplification, it was decided to displace the laser dot along each calibration board axis separately, and to monitor how the algorithm would perform with the increasing distance from the in-focus datum. For the higher resolution photographs, the laser dot could be displaced by 150 mm, but the lower resolution could only be displaced by 105 mm due to image boundary constraints.

For each experiment five tests were conducted, where 30 displacement steps would be taken from the same datum point, determined by the turret mill. The displacement step sizes increased with each test, starting with 0.02 mm and ending with 5 mm. The samples were separated into groups of five to provide an indication of the change in accuracy with distance from the camera region of focus. An example in Figure 36 shows the grouping of the smaller step sizes and the manner in which an image axis was investigated, which would have been the calibration

board y-axis. Note that the sizes of the dots and the displacements are not to scale and that the camera region of focus is not circular as the camera was facing the target surface at an acute angle.

The details of the step sizes and the space between the groupings can be found in Table 6 in Appendix B.2, while the camera setup conditions for each set of tests can be found in Table 7 in Appendix B.3.

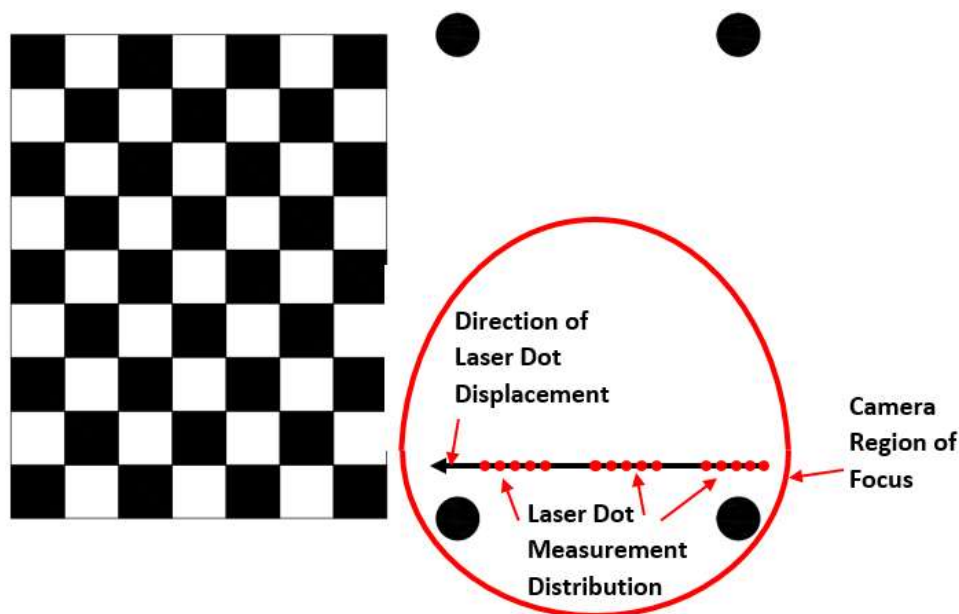


Figure 36. An example of the grouping of the smaller laser dot displacement steps. Note that the displacements and sizes of the dots are not to scale and are exaggerated for clarity. Note that the direction of laser displacement in the figure is in the positive y-axis direction for the camera and calibration board, and therefore in this case upwards.

The first two experiments were carried out at 2000fps as this provided the highest image resolution of 1280x1024 pixels. The second two experiments were carried out at 10 000fps, as this provided the time domain resolution required for relatively high-frequency disturbance inputs up to 200.0 Hz. The higher frame rate came with a drop in-image resolution to 528x396 pixels, though.

To compensate for the drop in-image resolution at higher frame rates, the camera software automatically cropped and enlarged the images, but did not auto focus the camera and therefore did not affect the camera calibration performed beforehand. The amount of cropping and enlarging could be observed beforehand and therefore the camera could be positioned and focused until the required number of calibration blocks could be observed.

Figure 37 is an example of how each test, at 5 mm step sizes, was executed and how the algorithm generally performed. Note the significant increase in the difference

between the true and determined laser dot displacements as the distance from the in-focus datum increases.

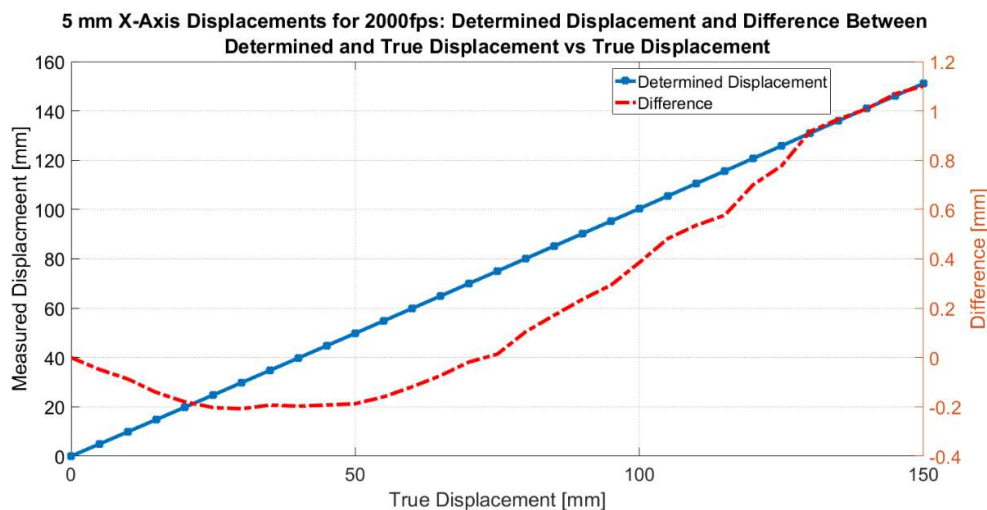


Figure 37. 2000fps, 1280 pixel algorithm accuracy verification test example data for the x-axis displacements. The graphs shows the determined laser dot displacement (left y-axis) and displacement difference (right y-axis) vs the true displacement. The steps were 5 mm in length. Note that the difference between the true and determined displacement appears to be small, but the displacement difference clearly shows the significant drop in algorithm accuracy as the distance from the region of camera focus increases. This has been attributed to a “smudging” of the calibration board block boundaries, which allow the algorithm to triangulate the position of the laser dot.

The results of the verification tests can be found in Table 1 below, which contain the average difference and uncertainty of the average, with a 95% certainty, between the displacement measured by the turret mill and the camera system for each image axis. In addition, the table also shows the corresponding lowest measurable laser dot displacement. This was determined as the average difference minus the uncertainty.

The way in which the average difference and corresponding uncertainties are used to determine the final measurements’ uncertainties are discussed in section 4.8.

Table 1 indicates that the algorithm performed better for the lower resolution images with a lower average difference and standard deviation of the average, which was not expected.

As the cameras had to be mounted at different distances to the target surface, a possible explanation that was considered was that in the higher resolution images the calibration blocks would be significantly smaller in the image than for the lower resolution images. Thus, even though there would be a higher density of pixels per image, the number of pixels per calibration block could have been lower than that of the lower resolution images, due to the increased distance to target.

Table 1. Algorithm accuracy verification test results

Verification Test Results for 2000fps and 10 000fps Experiments				
Frame Rate	2000fps		10 000fps	
Image Axis	1280 Pixel Axis (X Axis)	1024 Pixel Axis (Y Axis)	528 Pixel Axis (X Axis)	396 Pixel Axis (Y Axis)
Mean Difference ± Uncertainty [mm] (P=95%)	-0.06 ± 0.08	0.12 ± 0.22	-0.04 ± 0.06	-0.06 ± 0.07
Corresponding Minimum Detectable Displacement [mm]	>0.14	>0.1	>0.1	>0.13

However, upon inspection it was determined from the calibration images for the 2000fps tests, the pixel densities of the x-axes and y-axes were, on average, 4.8684 pixels/mm and 4.8567 pixels/mm respectively, whereas the pixel densities for the x-axes and y-axes of 10 000fps tests were, on average, 3.6557 pixels/mm and 4.0806 pixels/mm respectively. It was noted, though, that the further the blocks were from the laser dot displacement datum, the lower the pixel density.

When reconsidering Figure 37, the increase in measured displacement error was thought to result from the laser dot moving outside of the camera's region of focus. It did not imply that the algorithm's accuracy was drifting over time, though, as consistent difference error profiles were observed for every set of axis experiments, which indicated that a systematic error was present.

This did provide an explanation for the large differences in displacement differences seen at the maximum displacement from datum positions for the 2000fps and 10 000fps graphs. It still did not explain, however, why the higher resolution setup was producing less accurate tracking than the lower resolution system.

Considering that a large portion of the accuracy data used to determine the accuracy for the 2000fps tests lay beyond 10 mm, statistically then the poorer performance data of the 2000fps tests had a larger effect on the determined accuracy than the poor performance results of the 10 000fps tests.

Therefore, it was concluded that the unexpected difference in accuracy was not due to a serious system, or user, error, but due to setup and operation parameters that dictated how far the laser would have to be able to travel in one image, and how

many of these points would be in a region of significant poor performance. Therefore, the accuracies achieved for each setup were the optimal performances that could be achieved under the operational constraints of the experiment requirements, and not necessarily due to the system being at fault.

Considering the worst performance for the measurement system of the reference laser dot displacement, it was decided to design the gimbal base actuation to produce a 2 mm displacement of the reference laser dot for a 0.1 ° angular actuation. This resulted in a reference laser-to-target surface distance of 1608 mm. The gimbal laser at this distance, on the other hand, could not produce a bright enough laser dot site for the 2000fps camera to detect. Therefore, through testing, the maximum distance was found that the target surface for the gimbal laser could be mounted. This distance was found to be 580 mm from the centre of rotation of the reference laser.

4.8 Final Measurement Processing and Uncertainty

When processing the final measurement, the average displacement difference of the algorithm, determined in section 4.7, would be deducted from the measured displacement from equations (38) and (39), see equations (41) and (42).

The uncertainty in the final measurements for each experiment was determined through the use of the root sum square method, see equation (18) in section 2.8. Note that the accuracy verification test uncertainty, mentioned in section 4.7, is included here with the remaining system uncertainties, which are discussed in Appendix D.

Two critical components of the uncertainties in the measurements were the assumptions of the laser displacement profiles from sections 4.2 and 4.4. The uncertainty, introduced by the error between the true and measured angles, was quantified through Monte Carlo simulations. The distributions of the errors between the true and the measured angles can be found in Appendix D.3.

Equation (43) is the determined actuation uncertainty and equation (44) is the determined response uncertainty. It must be noted that components of the equations, such as the reprojection errors, would change per experiment if the camera was moved. Therefore, the measurement uncertainty was considered to be constant for a set of experiments, if both of the monitoring cameras had been undisturbed during the duration of a set of experiments.

The determination of the uncertainty of each measurement was necessary as it directly affected the bounds of the response gain that can be expected from the gimbal. A detailed breakdown of the error and uncertainty analysis to determine equations (43) and (44), is provided in Appendix D.

$$\theta_{\text{Actuation}} = \tan^{-1} \left(\frac{d_{\text{Reference_Observed}} - d_{\text{diff_ref}}}{D_{\text{Reference}}} \right) \pm u_{\text{Actuation}} \quad (41)$$

$$\theta_{\text{Response}} = \tan^{-1} \left(\frac{d_{\text{Gimbal_Observed}} - d_{\text{diff_gimbal}}}{D_{\text{Gimbal}}} \right) \pm u_{\text{Response}} \quad (42)$$

$$u_{\text{Actuation}} = \sqrt{\begin{aligned} &u_{\text{Reference_Assumption}}^2 + u_{\text{Reference_Reprojection}}^2 \\ &+ u_{\text{Reference_Camera_Distance}}^2 + u_{\text{Reference_Bore_Sight}}^2 \\ &+ u_{\text{Reference_Inclinometer}}^2 + u_{\text{Reference_Distance}}^2 \\ &+ u_{\text{Reference_Verification}}^2 \end{aligned}} \quad (43)$$

$$u_{\text{Response}} = \sqrt{\begin{aligned} &u_{\text{Response_Assumption}}^2 + u_{\text{Response_Reprojection}}^2 \\ &+ u_{\text{Response_Camera_Distance}}^2 + u_{\text{Response_Bore_Sight}}^2 \\ &+ u_{\text{Actuation}}^2 \end{aligned}} \quad (44)$$

5 Preliminary Tests

This chapter covers the preliminary tests, where the goal of these tests was to gain insight into how the actuation system and measurement system would perform, what unforeseen dynamics were present in the actuation system, how they affected the measurements and how the system needed to be changed to address these issues.

In addition, the tests allowed for an initial look at the gimbal's response gains, which would help in fine-tuning the variable ranges of the final experiment, such as frequency increment sizes and actuation increment sizes.

5.1 Determination of Support Frame Natural Frequencies

To use the designed support frame, discussed in chapter 3, its natural frequencies needed to be determined. The support frame was bolted to the heavy main support stand, as shown in Figure 17, which was in turn bolted to a purpose-built, concrete vibration lab floor. Even though these precautions were taken, it was necessary to determine the natural frequencies of the support frame as, if these resonances were present within the proposed test frequency range, they could affect the gimbal's responses. To determine these critical frequencies three harmonic excitation tests were performed on the beam and actuation plate, to determine the FRFs.

In the first of the natural frequency tests, the upper beam of the support frame, shown in Figure 38 with mounted accelerometers, was struck with a modal hammer from above. The reason for striking the beam from above was to excite the beam in the same direction as the shaker would. For the second modal hammer test, the actuation plate was struck horizontally with the modal hammer near accelerometer 5, as seen in Figure 39 with mounted accelerometers. The actuation plate was hit on the accelerometer-mounted side, thereby exciting the actuation plate in a rolling rotation.

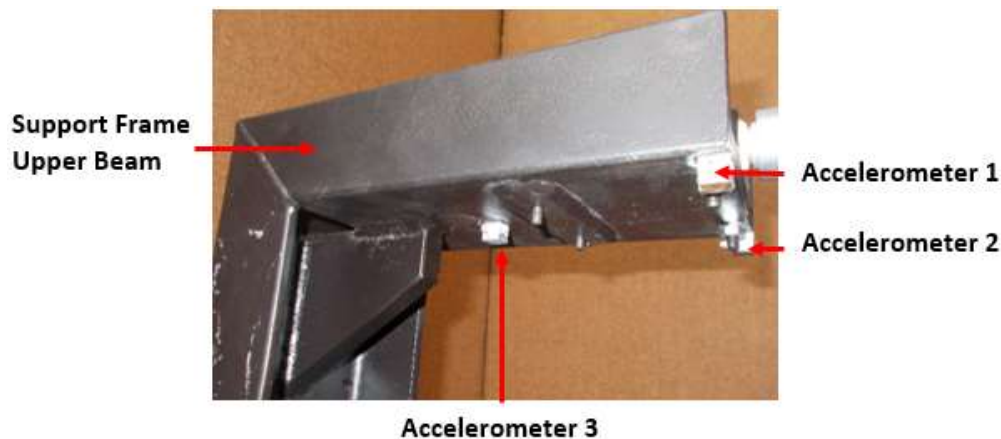


Figure 38. Accelerometers 1, 2 and 3 mounted to the upper beam of the support frame, all measuring acceleration in the z -axis with respect to the reference laser co-ordinate system, or upwards in the figure.

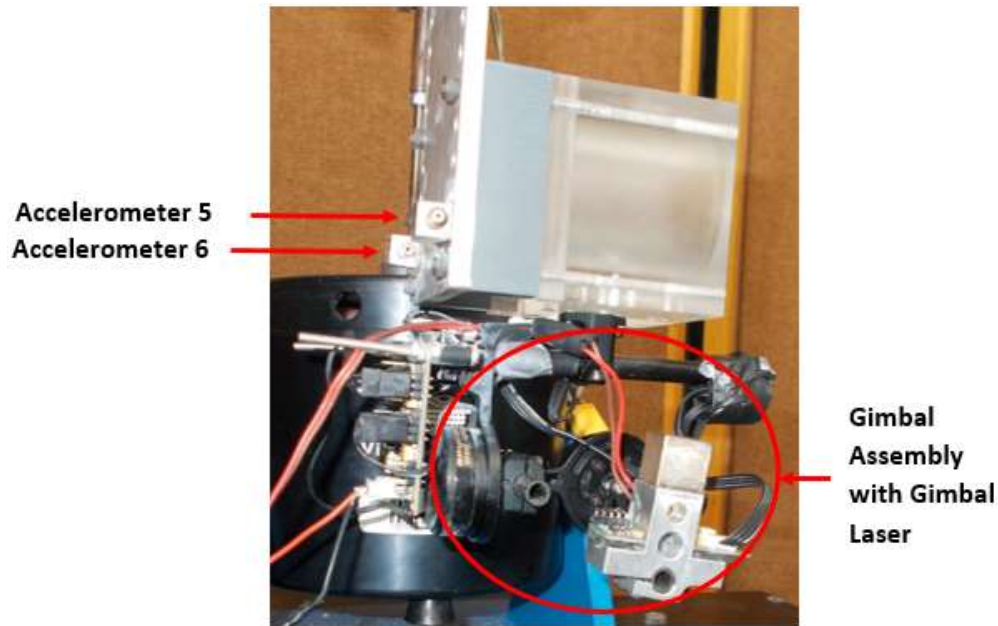


Figure 39. Accelerometers 5 and 6 mounted to the actuation plate to measure the horizontal accelerations of the plate. The direction of positive acceleration is parallel to the reference laser y-axis, which is towards the right in the figure.

Figure 40 and Figure 41 are the FRFs and corresponding coherences of the support beam and actuation plate for the first modal hammer test, respectively. The FRFs of the second modal hammer test can be found in Appendix E, as seen in Figure 81 and Figure 82, respectively. The natural frequency responses of the support frame beam and actuation plate, for both modal hammer tests, can be found in Table 2 and Table 3, respectively. Note that 10 averages were used in calculating the FRFs.

There was some difficulty in exciting the structure sufficiently, resulting in the poor low-frequency coherences. Therefore, for the third test, the mounted shaker was used to excite the beam and actuation plate by running a sinusoid frequency sweep through the shaker. It was found that the upper beam responded with a 50.0 Hz frequency throughout the test, while the actuation plate's responses were not as consistent, or clear, but were included. The power spectral density graphs can be found in Appendix E. See Figure 83 and Figure 84.

The presence of these natural frequencies meant that the amplitude of the beam displacements at these frequencies needed to be investigated.

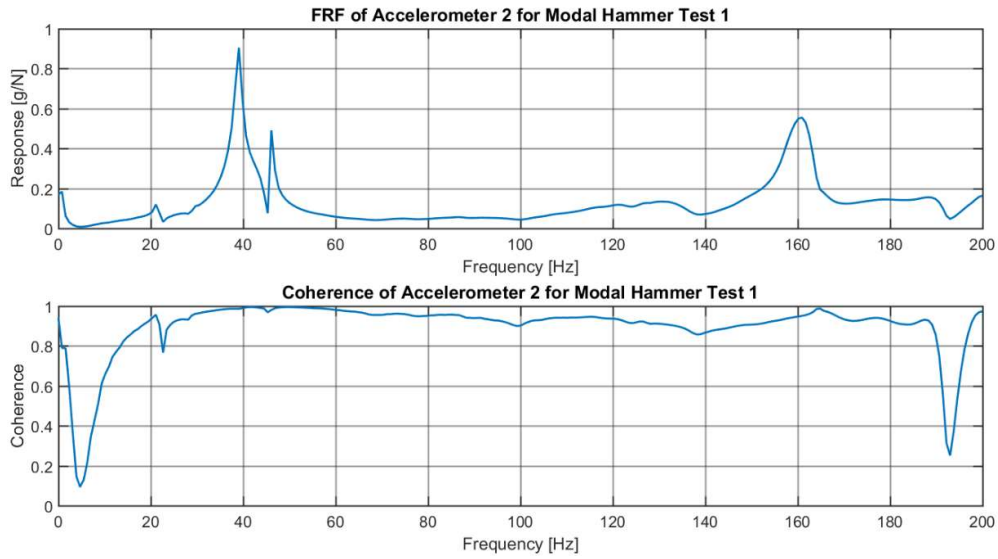


Figure 40. The FRF of the first modal hammer tests. The upper beam of the support frame was struck from above, the resulting responses indicating reliable resonances at 39.1 Hz, 46.1 Hz and 161.0 Hz.

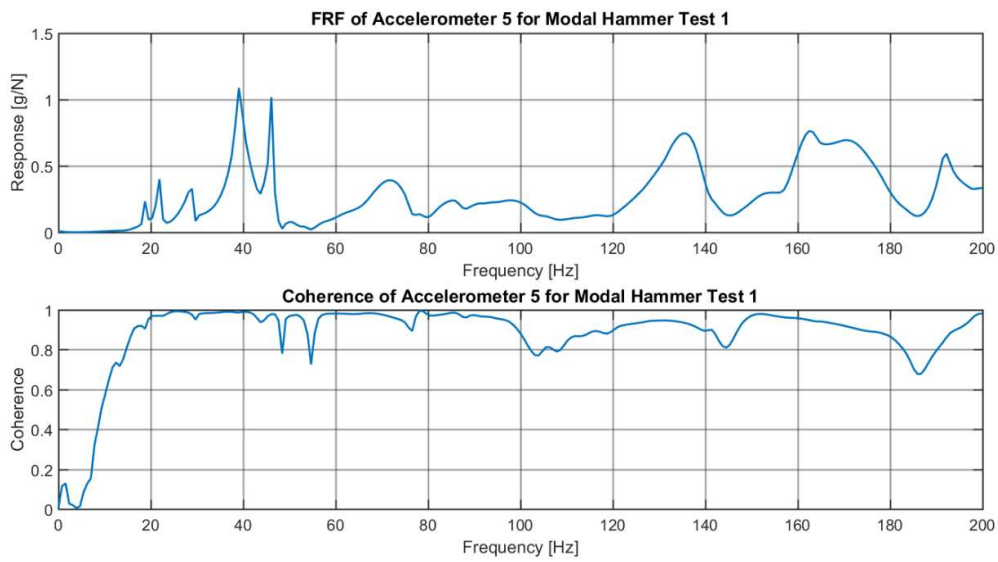


Figure 41. The FRF of the first modal hammer test for the actuation plate. Resonances at 18.8 Hz, 21.8 Hz, 28.9 Hz, 39.1 Hz, 46.1 Hz, 135.2 Hz and 162.5 Hz were observed.

Table 2. The results of the two modal hammer tests on the upper beam of the support frame. For the first modal hammer test the beam was struck from above, while for the second test the actuation plate was struck near the bottom of the plate in a horizontal direction.

Natural Frequency Tests for the Upper Beam of the Support Frame				
Modal Hammer Test 1 [Hz]	39.10	46.10	161.00	
Magnitude [g/N]	0.91	0.49	0.56	
Modal Hammer Test 2 [Hz]	18.80	21.90	46.10	135.20
Magnitude [g/N]	0.18	0.65	3.00	1.16

Table 3. The results of the two modal hammer tests on the actuation plate. For the first modal hammer test the beam was struck from above, while for the second test the actuation plate was struck near the bottom of the plate in a horizontal direction.

Natural Frequency Tests for the Actuation Plate							
Modal Hammer Test 1 [Hz]	18.80	21.80	28.90	39.10	46.10	135.20	162.50
Magnitude [g/N]	0.23	0.40	0.33	1.09	1.02	0.75	0.76
Modal Hammer Test 2 [Hz]	18.80	21.90	46.10	135.20	175.80		
Magnitude [g/N]	1.58	1.33	2.64	2.72	2.21		

5.2 Unwanted Support Frame Displacement

A series of upper beam, support frame displacement tests were performed at the critical frequencies determined in section 5.1. The tests revealed that noticeable vertical displacement was taking place at the end of the upper beam of the support frame. Figure 42 is an example of the beam's displacements, measured with a Inductive Displacement Transducer (IDT), at 40.0 Hz and a shaker peak-to-peak displacement of 0.27 mm. Although this displacement is small, when compared to the smallest measurable displacement, excluding the algorithm uncertainty, from

section 4.7, the displacement is slightly larger than double the minimum measurable displacement. Therefore, the displacement of the support beam had to be taken into account, or removed.

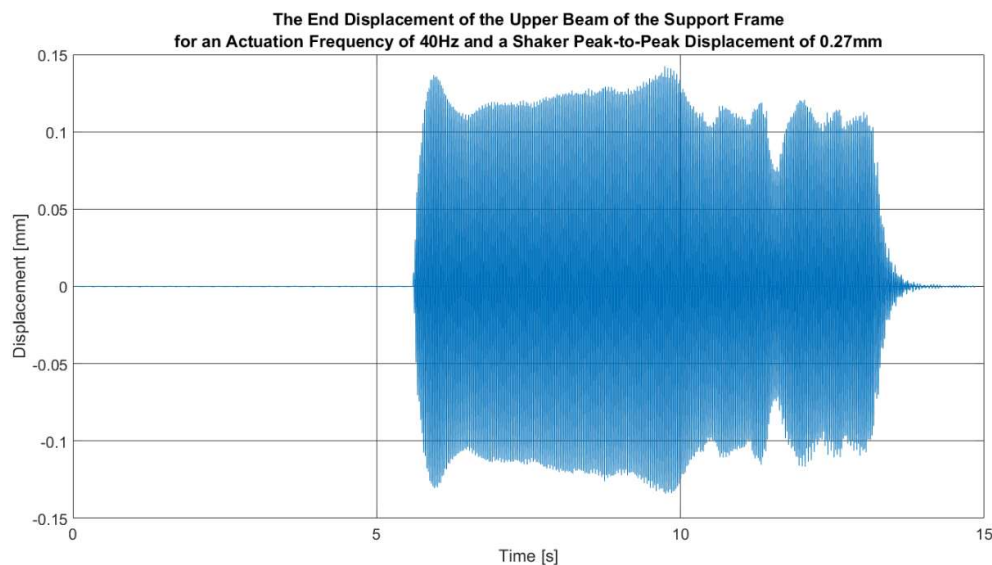


Figure 42. An example of the displacement of the upper beam of the support frame. The actuation frequency was 40.0 Hz and the shaker peak-to-peak displacement of 0.27 mm. The lack of displacement in the first six seconds of the test was due to the shaker not being turned on, until the gimbal was stable. The graph shows, though, that significant displacement of the upper beam of the support frame is taking place, which needs to be taken into account.

Stiffening of the structure in order to dampen out the oscillations was considered, but it was unclear how much time it would take to design a structure that would properly reduce all of the displacements, without introducing other unforeseen dynamics. Furthermore, designing such a structure would require in-detail modelling of the structure, which was not within the project scope.

Similar to the measurement of the actuation, as discussed in chapter 4, measuring the beam displacement with an accelerometer by using omega integration was considered. In order to achieve this, the measurements of the accelerometer and camera measurements needed to be synchronised, as well as the filtering of the acceleration signal, as discussed in chapter 4.

Synchronisation of the two measurement systems is possible by monitoring the cameras' trigger voltage with the LMS Data Acquisition (DAQ) device (Siemens, 2015). As the trigger voltage is a Transistor-Transistor Logic (TTL) voltage, the cameras' trigger moment can be determined and used in post-experiment processing. The TTL voltages refer to the voltage levels that define a digital zero, or one, at an input pin. Thus, a voltage that is measured to be between 0 V and 0.8 V

is defined as a logic zero, while a voltage measured to be between 2 V and 5 V is interpreted as a logic one (Brown & Vranesic, 2009).

Due to the recording duration of the 10 000fps camera, the longest time sample that could be taken was 0.1924 s. To produce an accurate FFT, a large number of sample points are required. For the case mentioned above, this can be achieved by using a high sample rate for the accelerometer. However, this introduces significant amounts of signal noise. To reduce this, filtering is used.

This method was tested, with some success. However, the filtering of the accelerometer data needed to be adjusted for each experiment and the consistency of the determined displacements was lacking. As over 300 sets of experiment data would need to be processed, and as more accurate and established measurement devices were available, it was decided to not pursue this method any further.

It was decided to use an IDT mounted to the support frame, of which the sensor end would be magnetically attached to the upper support beam end, see Figure 43. The IDT was a WA/10mm Inductive Displacement Probe produced by HBM and was a proven displacement measurement device, with high measurement accuracy. Data sheets on the IDT stated that the bandwidth of the device was limited to 65.0 Hz, so it was decided to limit the testable frequency band to 60.0 Hz. Synchronisation of the IDT measurements and the camera system measurements could be achieved by means of the camera trigger voltage method discussed above.

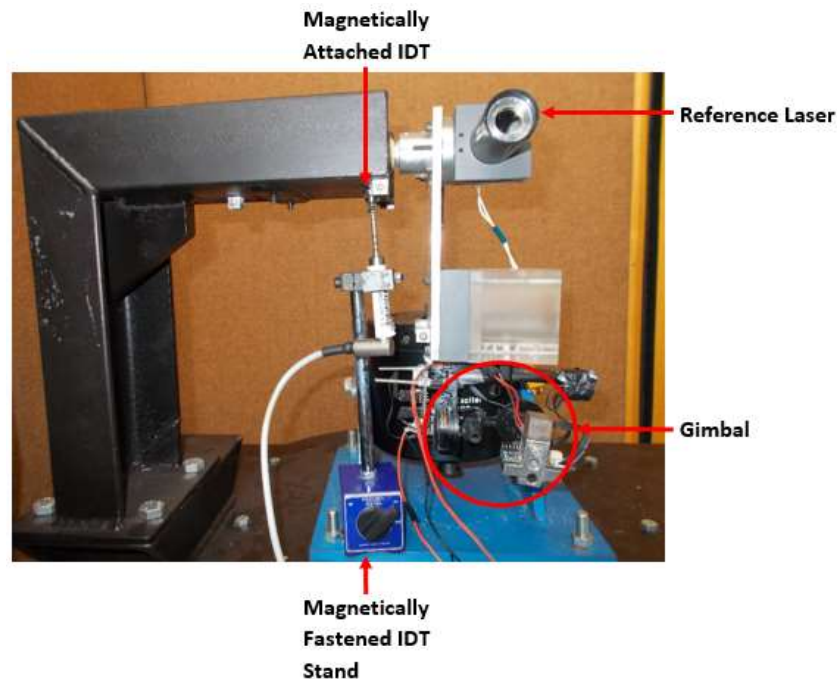


Figure 43. The magnetically attached Inductive Displacement Transducer (IDT). The base of the IDT was magnetically attached to the support frame, while the sensor tip was magnetically attached to the end of the beam.

5.3 Actuation Plate Yawing

The support frame displacement tests in section 5.2 also revealed that the reference laser dot was displacing horizontally, as seen in Figure 44, which was not expected. The off-centre positioning of the gimbal and the actuator driving point were suspected to be the sources of the yawing motion, until high-speed footage revealed that the yawing originated from the gimbal structure flexing. In the footage the pitch motor arm, as seen in Figure 45, would swing the roll motor and device mount back and forth, which produced a torque about the gimbal frame base, as seen in Figure 45, and is discussed in section 5.5. This torque caused the actuation plate and reference laser to twist.

As the gimbal could not respond in yaw, it was clear that the horizontal displacements of the gimbal laser were due to the undesired yawing rotation. Although unexpected, the yawing motion was not of concern as it was determined to be within 1° , and as discussed in Appendix D.3, the displacement assumptions for the reference and gimbal lasers from sections 4.2 and 4.4, could hold for rotations up to 10° . Any effect that the yawing had on the laser displacement assumption, was taken into account when determining the assumption uncertainty by using the Monte Carlo simulations and uncertainty analysis in Appendix D.

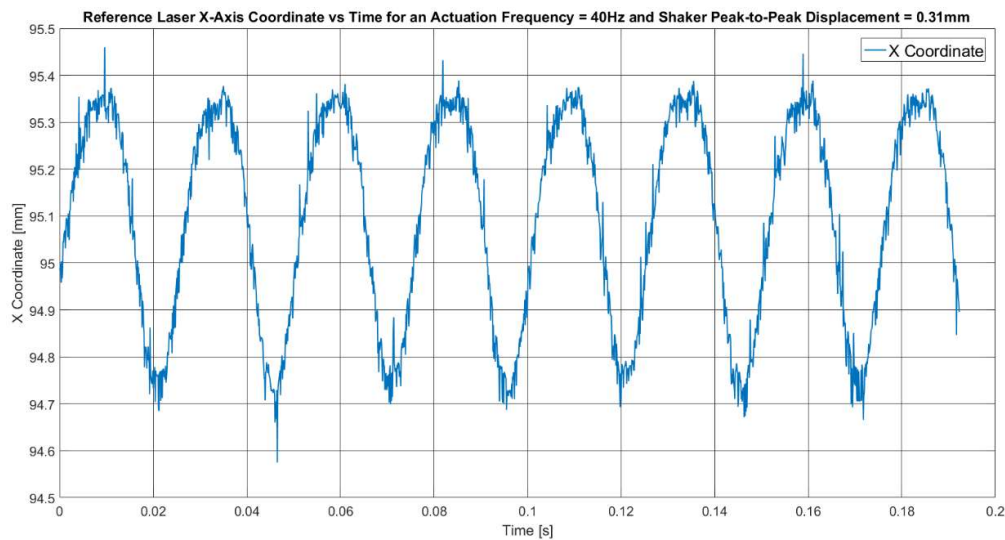


Figure 44. The reference laser dot x-axis co-ordinate vs. time for a pilot test at 40.0 Hz and a peak-to-peak displacement of 0.31 mm. The results indicate that the reference laser is being twisted, which was not expected.

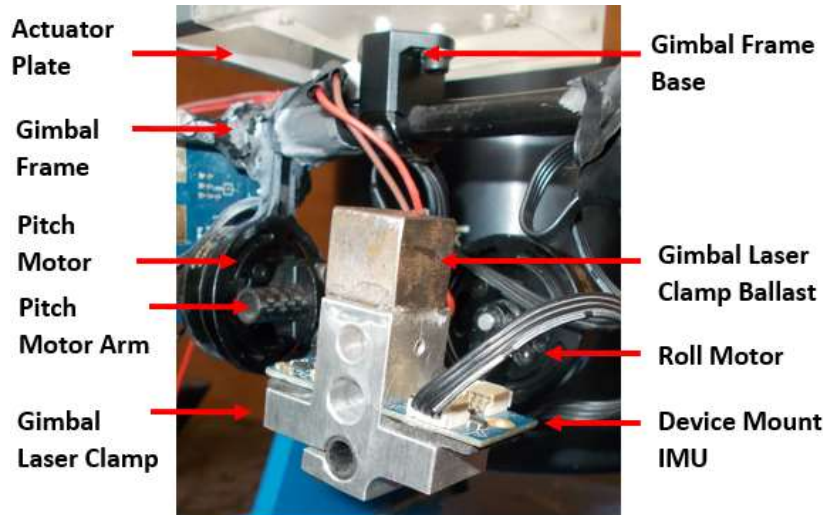


Figure 45. The gimbal, the gimbal frame, the gimbal base, the gimbal motor and the actuation plate. High-speed videos revealed that the horizontal displacement of the gimbal laser dot came from the pitch motor arm flexing and allowing the roll motor to be swung back and forth. These oscillations produced a torque on the gimbal frame base, which was transferred to the actuation plate, which began to twist. This twist caused the reference laser to yaw.

5.4 Gimbal Response Tests

For this series of tests, the gimbal response would be determined for two actuation amplitudes per test frequency, after which the frequency would be increased by 2.5 Hz. To achieve the larger actuation amplitude, the shaker peak-to-peak voltage would be tripled. As the shaker could not vibrate below 10.0 Hz (Bruel & Kjaer, 2014), the starting test frequency was 10.0 Hz, while the upper test frequency limit was 60.0 Hz, which was established in section 5.2.

5.4.1 Assumptions

In the operation of the gimbal laser, it is assumed that the laser beam projects parallel to the laser barrel, and that the laser beam is pointing in the same direction as the device mount. Similarly, for the reference laser, it is assumed that the laser beam projects parallel to the laser barrel, and that at equilibrium position the reference laser beam is perpendicular to its target surface. It was also assumed that the observing cameras, capturing the actuations and gimbal responses, start recording at the exact same moment.

The last assumption was made since, the processing speed of the cameras meant that the delay between the trigger being activated and the first image being stored, was, in the worst case, in the order of microseconds, which meant the delay was negligible (C. Robinson 2017, personal communication, 25th August), (iX Cameras, 2016).

5.4.2 Expected Results

For the operation of the gimbal it was expected that the greater the input energy into the gimbal, such as a large actuation amplitude or high actuation frequency, the more difficult it would be for the gimbal to respond and for the IMUs to send low-noise disturbance information.

For pitch and roll actuations the gimbal was expected to perform well for the first frequencies from 10.0 Hz to 15.0 Hz, gradually increasing in gain for both pitch and roll actuations. Approaching the natural frequencies of the actuation plate though, as shown in Table 2 and Table 3 and discussed in section 5.1, the gimbal response gain was expected to increase significantly and peak at the natural frequencies, indicating a loss of control. Similarly, it was expected that as the actuation amplitude increased, the gimbal would exhibit poorer disturbance rejection.

In addition to this, the following points were expected throughout the tests for each actuation type.

1. The gimbal will produce a response with a low gain at low frequencies, which will increase as the actuation frequency increases, until the gimbal cannot maintain control.
2. The gimbal laser dot will displace with a sinusoidal displacement profile, due to the actuation method.
3. The gimbal should perform better for roll actuations, as the gimbal will not be rotated in pitch, and therefore would not require device mount pitch adjustments.

As discussed and shown in section 4.4, for an ideal gimbal, the gimbal laser dot displacement is as a result of the gimbal's vertical displacement. When compared to the reference laser dot displacement, the gimbal laser dot displacement is negligible. Therefore, regarding point 3, as the device mount does not need to respond in pitch, the vertical displacement of the gimbal laser should only result from the gimbal's vertical displacements, as for an ideal gimbal. As the gimbal is not ideal, some amplification of the input is expected and therefore low gains are expected for the responses to roll actuations.

For pitch actuations however, as the actuation directly affects the gimbal and device mounts' pitch poses, the gimbal's responses are expected to be more acutely affected. Therefore, the response gains for pitch actuations are expected to be larger and more erratic than the response gains to roll actuations.

5.4.3 Experiment Setups and Procedure

Figure 46 and Figure 47 show the camera and target surface setups for the pitch actuation tests, of the gimbal laser and reference-laser-monitoring cameras, respectively. Figure 48 shows the monitoring camera for the gimbal laser, once repositioned for the roll actuations. The target surfaces had the camera calibration patterns on one side of the surface, with the other side clear and white. This was

needed, as the intensity of the laser dot site would be changed as it passed over the darker regions of the board.

Therefore, the calibration would be done with the one side of the board, and then the board would be clamped with the calibration pattern in the camera centre of focus. The datum photograph and measurements would be taken with the latter being done using a laser range finder, relative to the support frame. After this, the board would be rotated and clamped again to ensure that the laser would only shine on the white side of the board. The board's orientation and distance to the support frame would be checked against the datum measurements, to ensure that the board was in the same position as before. The uncertainty introduced by this process is included in the uncertainty analysis in Appendix D. Matt vinyl finishes were used for both boards. Note, the distances that were used for the individual target surfaces to their respective lasers, were discussed at the end of section 4.7.

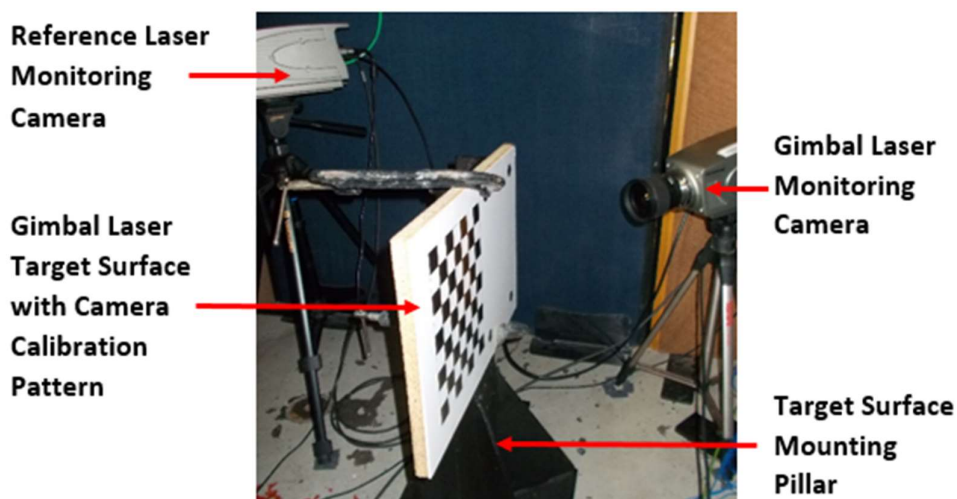


Figure 46. The monitoring camera for the gimbal laser, with the gimbal laser target surface in the foreground. The monitoring camera for the reference laser is in the background on the left. The target surface was held in place with g-clamps on a steel pillar, which was bolted to the floor. The left side of the target surface had the calibration pattern on it.

For each test, at each frequency, the gimbal and lasers would be switched on first. Once the gimbal calibrated and remained stable, the recording of the IDT and camera-trigger voltage, through the Quantum X, would be started, followed by the recording of the LMS connected accelerometers and camera trigger voltage. The shaker would then be switched on, and the cameras would be triggered. Once the LMS software finished its recording, the shaker would be stopped, the lasers and gimbal switched off, the IDT recording stopped, and then the cameras taken out of trigger standby mode.

The reason for using two DAQs was that there were not enough functioning channels on the LMS DAQ, or the Quantum X. Note, the accelerometers referred

to above are from section 5.1 and were mounted in the same positions throughout the entire investigation.

The voltage applied to the shaker was fine-tuned with the use of an oscilloscope and an analogue signal amplifier, while the supplied actuation frequency was generated and controlled by the LMS DAQ and the LMS Test Express software (Siemens, 2015).

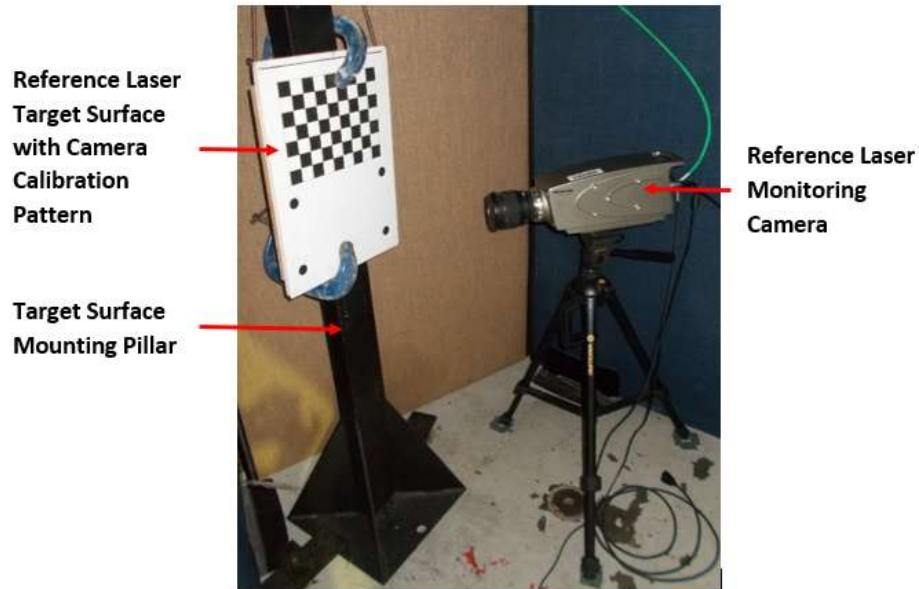


Figure 47. The monitoring camera for the reference laser, with the reference laser target surface. The target surface was mounted to a steel pillar, which was bolted to the floor. The target surface was lightly held in place with g-clamps.

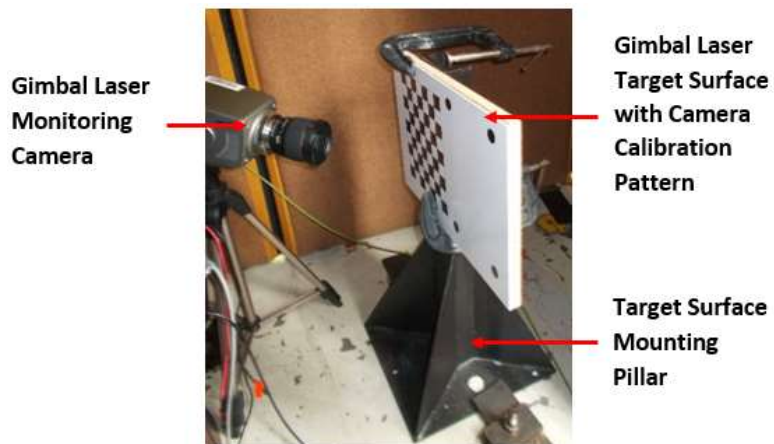


Figure 48. Gimbal laser-monitoring camera with the gimbal laser target surface on the right of the image. The target surface had been placed to the right of the main support frame to allow the gimbal to be rotated by 90° to capture the pitch responses to roll inputs.

5.4.4 Pitch Actuation Gimbal Response Results and Discussions

During the experiments, from 30.0 Hz and above, rattling was heard, which increased in volume with the actuation frequency. No loose bolts, or joints, were found on the support structure, and the gimbal rotated smoothly in hand. The source of the rattling was discovered after the pitch and roll experiments and was found to be a gimbal grub screw. The effect of the loose grub screw on the gimbal performance is discussed in section 5.5.

Figure 49 contains the gimbal response gain plots for the small and large pitch actuations, with their respective measurement uncertainties. The error bars for the gains provide an indication of the displacements of the laser dots for the gimbal laser and the reference laser. The larger the displacements, the smaller the uncertainty, and vice versa. Where the displacements approached, or exceeded, the accuracy limits of the measurement system, the uncertainty of the measurement would become large. This resulted in an unreliable data point and the lower bound of the measurement uncertainty becoming a negative number, which could not translate to the decibel scale. Therefore, these measurements had to be omitted.

Considering the figure, the gimbal appears to attenuate the inputs between 0.0 Hz and 20.0 Hz, which was expected. However, the gain does appear to be reducing from a region of amplification, which was not expected. In addition, the gains for the small and large pitch actuations appear to show no consistent relationship, which was not expected.

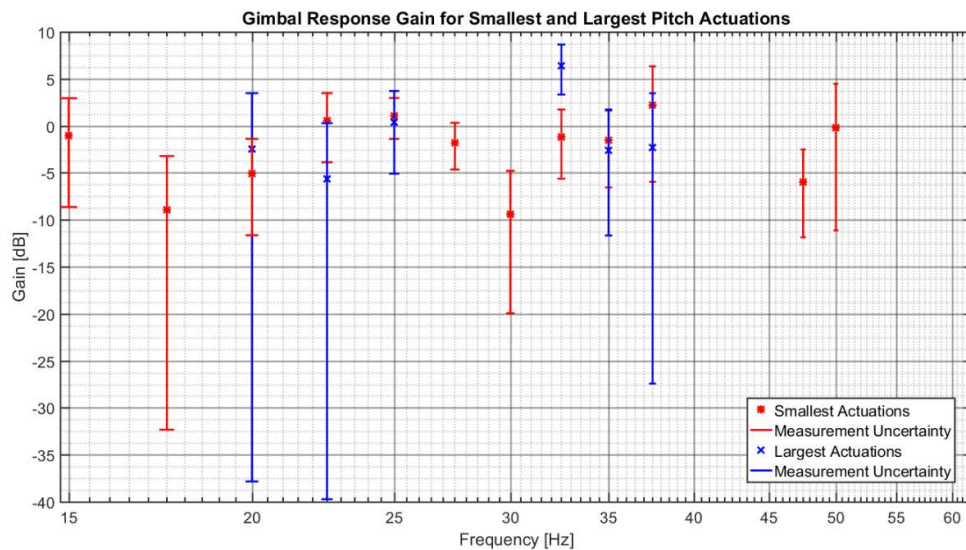


Figure 49. The gimbal's pitch response gain plot for pitch actuations.

No clear linear relationship between input frequency and response gain is visible for either of the actuation amplitudes, which was not expected. In addition, no consistent correlation can be seen between the response gains and the support frame and actuation plate natural frequencies.

During the processing of the results, it was noticed that the displacement profile of the gimbal laser dot, as seen in Figure 50, was a nonlinear response, which was not expected. The figure shows the reference and gimbal laser dot displacements versus time, for pitch actuations at 17.5 Hz and a shaker peak-to-peak displacement of 0.3 mm, or a corresponding actuation angle of 0.14° . For the reference laser, measured against the right y-axis, the peaks correspond to the furthest forward swing of the gimbal. Therefore, the valleys in its displacements correspond to the furthest back swing of the gimbal away from the target surface.

The left y-axis is used to measure the gimbal laser dot displacements. The calibration application determined the positive y-axis to be downwards, with respect to the world co-ordinate system.

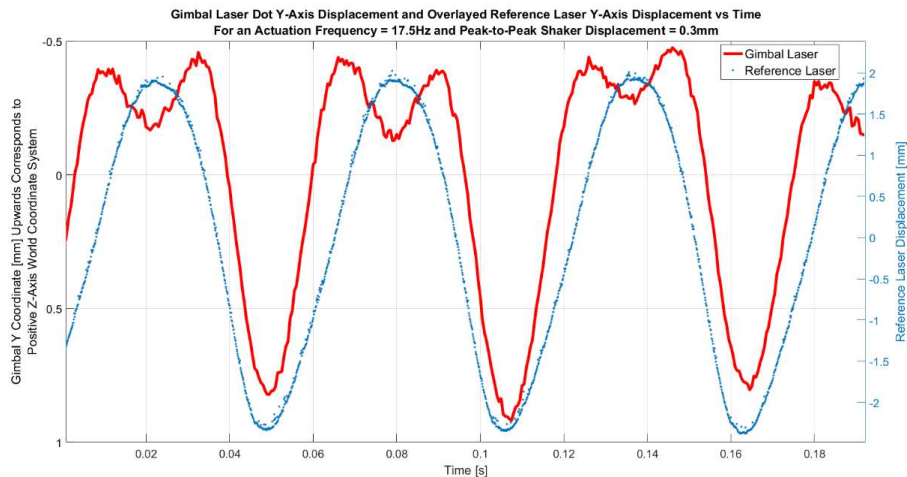


Figure 50. The gimbal pitch response to pitch actuations at 17.5 Hz and shaker peak-to-peak displacement of 0.33 mm, or an actuation angle of 0.15° . The figure shows the reference laser dot and gimbal laser dot displacements versus time, for pitch actuations at 17.5 Hz and shaker peak-to-peak displacement equal to 0.33 mm, or a corresponding actuation angle of 0.15° . The displacement of the reference laser dot is measured against the right y-axis, while the gimbal laser dot displacement is measured against the left y-axis. The calibration application determined the positive y-axis to be downwards, with respect to the world co-ordinate system. Therefore, the y-axis of the graph has been inverted for the displacements to be relative to the world co-ordinate system.

As the gimbal motors have a direct impact on the gimbal laser dot displacement, it is suspected that this double oscillation is due to the gimbal struggling to respond. The double oscillation is also seen to be cyclic, where the first peak will be larger than the second, which is then switched for the next forward swing peak.

Although the nonlinear responses were not expected, when the scale of the displacements are taken into account, it is apparent that the magnitudes of the double oscillations are significantly smaller than the overall input and response magnitudes. Therefore, as discussed in section 4.2, these nonlinearities could be ignored.

5.4.5 Roll Actuation Gimbal Response Results and Discussions

During the experiments, for 27.5 Hz, 30.0 Hz and frequencies above 35.0 Hz, the gimbal controller struggled to maintain control, often requiring three or four runs before the gimbal response could be kept. For frequencies from 35.0 Hz and above, rattling was heard again, which increased in volume with the actuation frequency, which was also noted in section 5.4.5.

Unlike the pitch actuation tests, though, the gimbal would not operate beyond 40.0 Hz. For the largest actuations at 27.5 Hz, 30.0 Hz and 37.5 Hz, and 40.0 Hz for both actuation amplitudes, the gimbal laser would swing violently, resulting in the laser dot displacing beyond the camera field of view, as seen in Figure 51.

Figure 52 shows the gimbal pitch response gains for the smallest and largest roll actuations. Similar to the pitch actuation tests, no clear relationship between the gimbal response gain and the actuation frequency is observed. When compared to the pitch actuation tests' gains, the response gains of the roll actuations appear to be more consistent, with smaller uncertainty bounds. However, the response gains for roll appeared to be consistently larger than the response gains to pitch actuations, which was not expected.

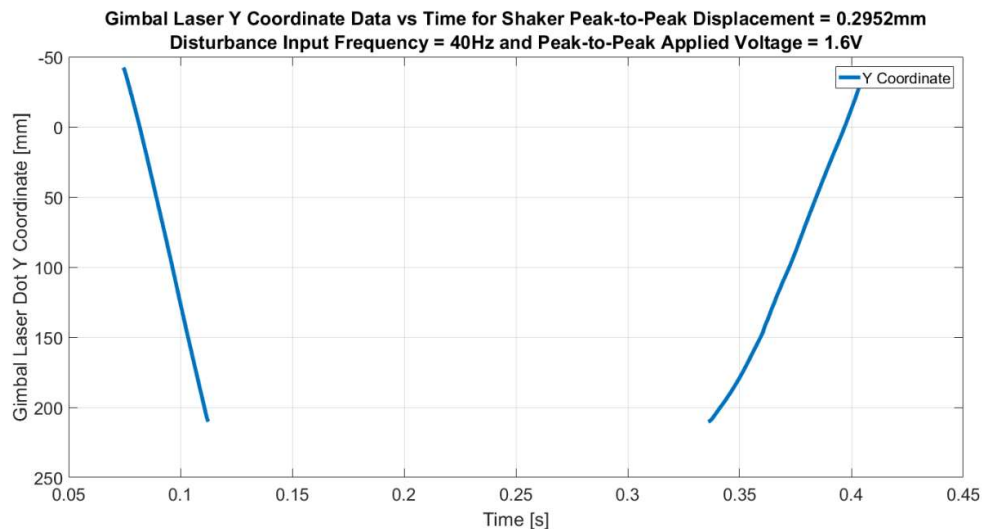


Figure 51. An example of the gimbal losing control for the largest roll actuations at 40.0 Hz. The break in the displacement line of the laser dot is due to the laser dot moving outside of the camera's field of view. The calibration application determined the positive y-axis to be downwards, with respect to the world co-ordinate system. Therefore, the y-axis of the graph has been inverted for the displacements to be relative to the world co-ordinate system.

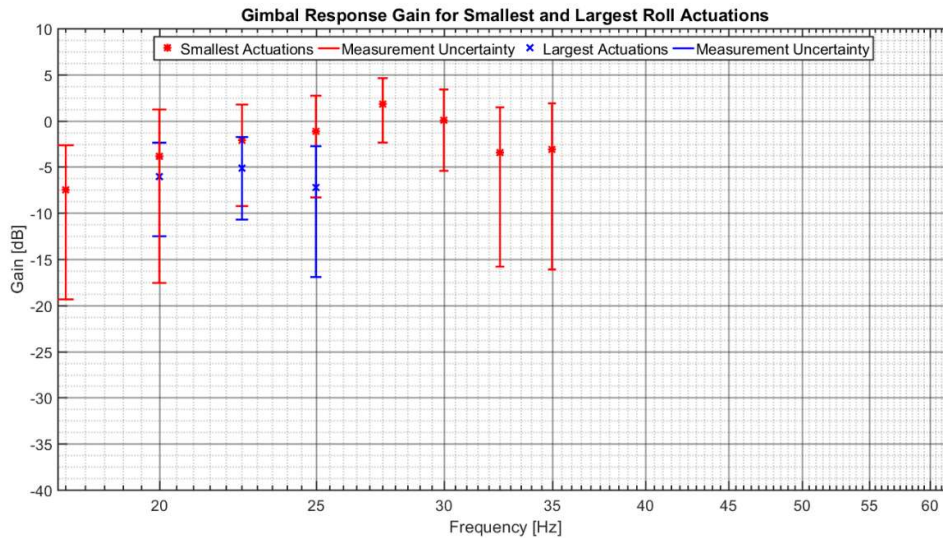


Figure 52. The gimbal's pitch response gain plot for the smallest and largest roll actuations. Note that the graph extends to 35.0 Hz as the gimbal could not operate beyond that point, and that the gimbal could not operate for 27.5 Hz, 30.0 Hz, 32.5 Hz and 37.5 Hz for the largest actuations.

5.5 Preliminary Tests Summation

The preliminary tests for the support frame, actuation system and gimbal response produced the following results:

1. The support frame and actuation plate natural frequencies induced displacements in the upper beam of the support frame. These frequencies and displacements were present in the test frequency range, which meant the use of an IDT was necessary to account for their effects.
2. The gimbal's responses to pitch and roll appeared to differ, with the responses to roll producing more consistent, but larger, response gains. The larger gains were unexpected, as the device mount did not need to adjust in pitch when being subjected to roll actuations.
3. The response gain did not show a clear relationship with increasing actuation amplitude.

After the experiments were completed, the gimbal was removed from its mounting on the actuation plate for a close inspection of possible damage, or for any signs of wear of the motors or joints. Here it was noticed that a grub screw, connecting the pitch motor arm to the pitch motor, had slightly loosened, which allowed for a small play in the pitch motor arm connection, which allowed the roll motor assembly to oscillate slightly. Figure 53 shows the gimbal and the device mount with the direction of rotation superimposed on the figure.

This caused the roll motor and laser mount to displace on the pitching motor shaft, which was suspected to be the source of the gimbal's loss of control. Upon tightening of the grub screw and testing at the frequencies that the gimbal lost

control, it was found that the gimbal could operate. Thus, for the main experiments, after each test, the frame was inspected for loose screws and joints.

The improved gimbal performance for pitch actuations after the tightening of the grub screw, lead to the loose pitch arm being suspected of being the source of the poor performance.

The loose pitch arm was also suspected to be the reason for the poorer performance seen in the roll actuations. The reason is that the pitch arm would be perpendicular to the direction of movement, therefore aggravating the moment arm.

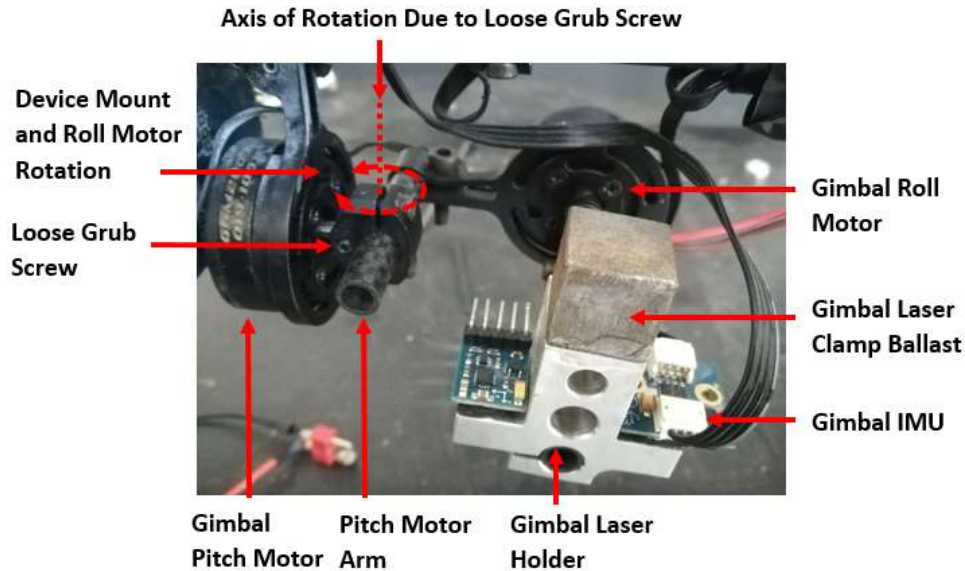


Figure 53. The gimbal and device mount, with the loose grub screw on the pitch motor shaft. The figure shows the rotation direction and axis of rotation of the roll motor and device mount assembly about the pitch motor shaft, because of the loose grub screw. The grub screw was meant to keep the pitch motor arm locked onto the pitch motor shaft. As this grub screw loosened, however, the weight on the end of the arm was able to shift, sending vibrations through the frame of the gimbal.

6 Final Experiments

This chapter covers the experiments and their observations that produced the final gimbal response gain plots for this project. The assumptions, expected results and experiment procedures are discussed, followed by the observations made during the experiments. The results and discussions associated with these can be found in sections 6.4 and 6.5

6.1 Assumptions, Expected Results and Experimental Procedure

The assumptions outlined in section 5.4.1 were used in the final experiments, while the setups and procedures outlined in section 5.4.3 were also used in the final experiments, with the addition of the joint and fastener checks after each test. It was recognized that smaller increments in the increase of the actuation size were required. Therefore, a shaker middle voltage was introduced into the voltages used in the preliminary tests.

It was expected that, following the preliminary tests and the finding of the loose grub screw, the gimbal response performance would improve.

In the preliminary tests, no clear, or consistent, correlations were observed between the gimbal responses and the natural frequencies of the support frame and the actuation plate. It was unclear, though, whether this was as a result of the loose grub screw, or not. Therefore, the results expected for the preliminary tests were also expected for the higher frequency and amplitude resolution experiments, in addition to the following.

1. For each type of rotation, the gimbal response will worsen with increasing actuation amplitude.
2. The gimbal will produce a response with a low gain at low frequencies, which will increase as the actuation frequency increased.
3. The gimbal laser will displace with a sinusoidal displacement profile.
4. The gimbal will perform better for roll actuations than for pitch, as the device mount will not be rotated in pitch, and therefore would not require device mount pitch adjustments.

6.2 Experiment Observations for Pitch Actuations

For the actuation frequencies from 10.0 Hz to 14.0 Hz the gimbal laser displacements were very small, with no drifting oscillation observed. From 14.0 Hz, however, the laser dot displacement, for the gimbal laser significantly increased with a noticeable increase in actuation angle at 21.0 Hz.

From 25.0 Hz the gimbal laser dot's displacements became circular. In addition, the gimbal laser dot's oscillations were observed to be slow and out of sync with the reference laser dot's movements.

At 30.0 Hz a buzzing noise was heard, which was suspected to be the device mount IMU cable knocking against the gimbal frame. The cable could not be fastened, as there needed to be sufficient play on the cable to allow the device mount to be rolled. Beyond 30.0 Hz, the cable did not vibrate in this manner again. From

34.0 Hz noticeable horizontal reference laser dot displacement was observed, which increased with frequency and applied shaker displacement amplitude.

At 37.0 Hz, with an applied voltage of 3.9 V, and at 45.0 Hz and an applied voltage of 4.7 V, a vibration noise could be heard. Similar to the preliminary tests, as the actuation frequency was increased, the gimbal's ability to maintain control during the test became less frequent. Approaching 60.0 Hz, the gimbal appeared to be off as the device mount's movements were dictated entirely by the movement of the actuation. The support frame and gimbal were inspected after each case, and no loose components, or fasteners, could be found.

Finally, the high-speed cameras were used to capture the actuating plate and the gimbal's movements during tests at 10.0 Hz at 1.2 V, 20.0 Hz at 2.2 V and 43.0 Hz at 4.5 V using frame rates of 1000 fps. For the 10.0 Hz test, the gimbal and structure appeared to be operating as expected. However, for the 20.0 Hz test, slight gimbal twisting was observed, which was not expected.

For the 43.0 Hz test, significant flexure of the gimbal structure was observed, which was transmitted up to the reference laser. Thus, it was determined that the horizontal displacements, seen in both the reference laser and gimbal laser dot displacements, were as a result of the gimbal frame flexing. This explained the significant difference in horizontal displacements between the reference laser dot and gimbal laser dot. The acceleration versus time plots of the actuation plate mounted accelerometers, accelerometers 5 and 6 in Figure 85 and Figure 86 in Appendix E, produced supporting results.

6.3 Experiment Observations for Roll Actuations

For the actuation frequencies from 10.0 Hz to 14.0 Hz, the gimbal laser dot displaced slightly. Most of the displacement was in the horizontal axis.

From 30.0 Hz to 45.0 Hz the gimbal laser dot oscillations gradually drifted in the vertical direction. For the frequencies below 30.0 Hz, the laser dot's oscillations drifted upwards, while for the frequencies from 30.0 Hz to 45.0 Hz the laser dot's oscillations drifted downwards.

Above 45.0 Hz, the displacement of the gimbal laser dot seemed first to increase and then decrease during an experiment. Thus, it appeared as if the laser dot became stationary and then would begin to oscillate again, indicating that a beat was present. From 52.0 Hz the laser dot displacements became increasingly smaller, to the point where only the drift in vertical position of the laser dot could be seen, and it appeared as if the gimbal was slowly drifting back and forth.

At the end of each test, the shaker was switched off, but the gimbal was left on. For all but two frequencies, the gimbal controller was still able to maintain control after the shaker was switched off. The problem frequencies were 30.0 Hz and 31.0 Hz, where the gimbal would continue to rotate its motors, with increasing violence, after the shaker was switched off.

6.4 Pitch Actuation Results and Discussions

This section covers the results and discussions of the pitch actuation tests. Figure 54 and Figure 55 show the peak gimbal response gain plots to the three pitch actuation sizes. Figure 54 shows the gains without the uncertainty bounds, and Figure 55 shows the same results, with the measurement uncertainty bounds.

Figure 54 indicates that for the first 17.0 Hz the gimbal gain is being attenuated, implying the gimbal is countering the inputs. However, these gains are larger than expected from section 5.4.2, therefore it indicates partial countering of the inputs.

The gain also appears to be cyclic, peaking at 32.0 Hz and then increasing again toward 60.0 Hz. It also is noted that in the range between 45.0 Hz and 49.0 Hz, the gains of the three different actuation sizes differ significantly and appear to be erratic. Where the uncertainty of a measurement was greater than the magnitude of the measurement, the point was ignored in Figure 55. The individual results for each actuation amplitude for the pitch actuations can be found in Appendix F.

The gimbal resonances, at the support structure and actuation plate natural frequencies, are discussed in section 6.4.1. The peak responses at 32.0 Hz and 60.0 Hz are discussed in section 6.4.2 while the gain attenuations from 11.0 Hz to 17.0 Hz and from 32.0 Hz to 49.0 Hz, are discussed in sections 6.4.3 and 6.4.4 respectively. A gain and uncertainty sample calculation is also provided in section 6.4.5.

One of the expectations from section 6.1 was that the gain would increase with the actuation amplitude. Considering Figure 54, no consistent relationship between the actuation size and the gain is observed.

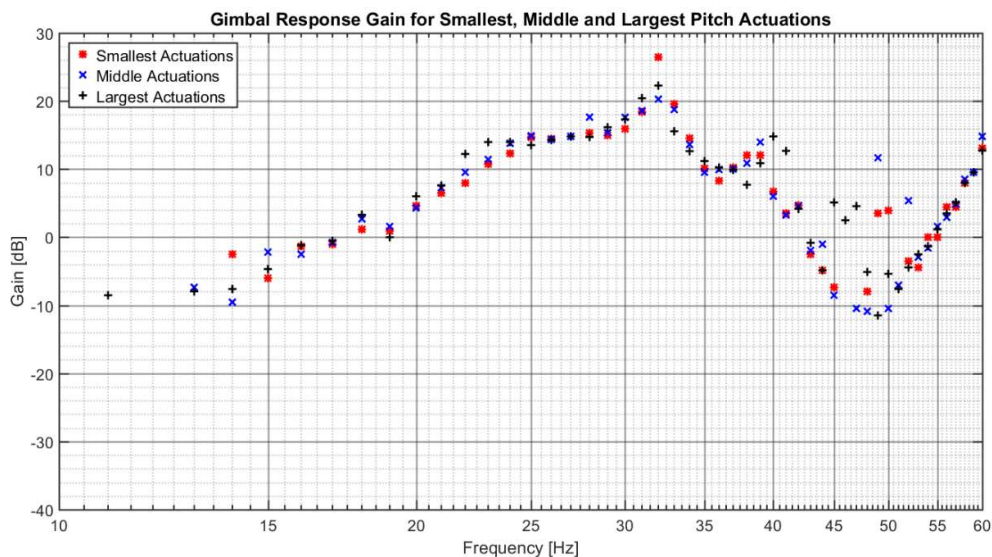


Figure 54. The gimbal response gains to the three different pitch actuation sizes.

Considering Figure 55 in the 10.0 Hz to 20.0 Hz range, there is a clear and steady increase in gain, but a reduction in gain uncertainty. For the lower frequencies, there are fewer cycles for each data set. Therefore, there are fewer peak values to measure, which corresponds to a larger measurement uncertainty. In addition, as the laser dot displacements approach the lower limit of the measurable displacements, the uncertainty of the measurement increases.

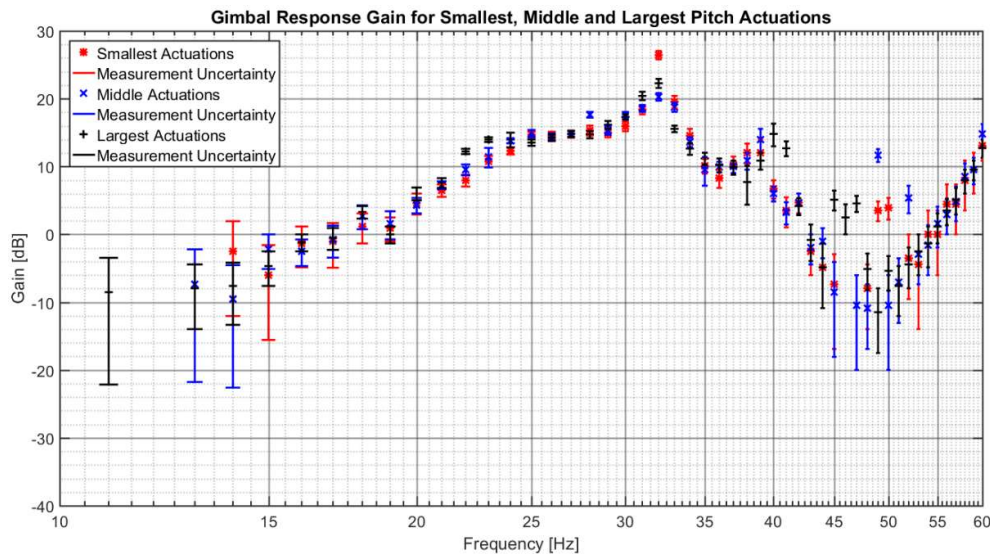


Figure 55. The gimbal response gains to the three different pitch actuation sizes with uncertainty bounds. The overlapping of the uncertainty bounds indicate that there is a correlation between the measured values for the three responses.

6.4.1 The Gain Resonances at the System Natural Frequencies

The gimbal gain resonances that correspond to the natural frequencies of the support structure and actuation plate are summarised in Table 4. Note, T1, T2 and T3 in the table refer to the first modal hammer test, second modal hammer test and frequency sweep test respectively.

The gimbal showed distinct gain resonance for all three actuation sizes at 18.0 Hz, 39.0 Hz and 50.0 Hz, as seen in Figure 54 and Figure 55. Importantly, these responses corresponded to natural frequencies of the support structure and actuation plate, which can be found in Table 4. Regarding the 18.0 Hz resonance, however, it was noted that the closest natural frequency was 18.8 Hz. With the frequency difference being larger than the other frequency differences, there was some concern regarding the correlation between the two.

For the remaining support frame and actuation plate natural frequencies from section 5.1, no distinct resonances were observed for all three actuation sizes. Therefore, no certain connection could be made between the gimbal response and the natural frequency of interest.

The gimbal resonances in Table 4 were expected, as there were no significant damping devices isolating the gimbal from the input vibrations. Therefore, if the gimbal is part of a measurement system, it will need vibration isolation. However, considering the high frequency drone controller vibrations from section 3.1 and the gimbal's responses, the efficacy of the vibration isolation will need to be confirmed.

Table 4. The gimbal gain resonances and corresponding support structure and actuation plate natural frequencies for pitch actuations.

The Gain Resonances for the Pitch Actuation Tests		
Gain Resonances [Hz]	Support Structure Natural Frequencies [Hz]	Actuation Plate Natural Frequencies [Hz]
18.0	18.8 (T2)	18.8 (T1 & T2)
39.0	39.1 (T1)	39.1 (T1)
50.0	50.0 (T3)	-

6.4.2 The 32.0 Hz Resonance and the Gain Increase towards 60.0 Hz

The response at 32.0 Hz was not expected, as there were no natural frequencies close to this response. If the source of the 32.0 Hz response was external to the gimbal, or from the gimbal structure, it would have been observed in one of the natural frequency tests. However, no clear responses can be seen at 32.0 Hz in any of the natural frequency test results.

This and the buzzing observation from section 6.2, was the reason that the device mount IMU cable was suspected to be the source of the gimbal's response 32.0 Hz. As stated in section 6.2, it was suspected that the device mount IMU cable was knocking against the gimbal frame. Therefore, as no noise was observed for the 32.0 Hz tests, device mount IMU cable vibrations were suspected to be the most likely source of the gain at 32.0 Hz.

It is thought that the vibrations were being transferred to the device mount IMU, effecting its measurements. However, this required an in depth investigation to provide proof. As it lay outside of the scope of the thesis, it was left for following investigations.

6.4.3 The 11.0 Hz to 17.0 Hz Gain Attenuation

The gimbal was expected to be able to function for the lower end of the frequency range, which appears to be proven by the gains between 11.0 Hz and 17.0 Hz in Figure 54. When considering the time signal data in this region, though, the gimbal

responses appeared to be nonlinear, as in Figure 50 in section 5.4.4. Figure 56 is an example of this for the largest pitch actuations at 13.0 Hz.

The graphed data shows nonlinear plateauing of the response, near the peaks of the inputs. This plateauing was noted for all the responses from 11.0 Hz to 16.0 Hz, but not from 43.0 Hz to 54.0 Hz. However, as discussed in section 5.4.4 regarding Figure 50, the nonlinearities are significantly smaller than the overall inputs and responses. In addition, as stated in section 1.1, the focus of the study was on the peak response of the gimbal for a given disturbance frequency and amplitude, due to the LTI assumption and approach detailed in section 4.2. Therefore, the nonlinearities in the responses were seen as negligible and were ignored.

Considering the magnitude of the peak gimbal laser dot displacements in Figure 56 and that they would be discernible against the reference laser dot displacements, it is clear that the gimbal is amplifying the inputs.

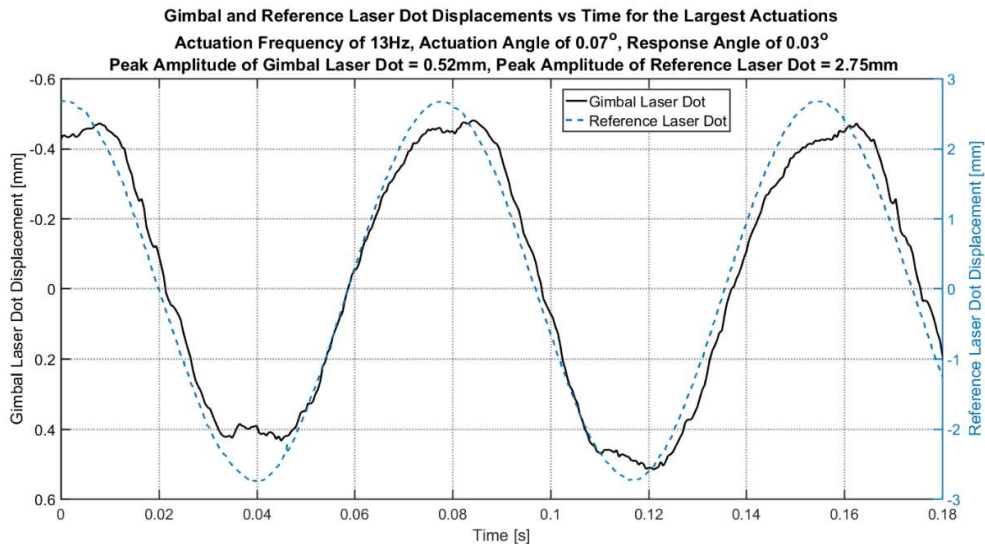


Figure 56. A time domain example of the gimbal's responses to the largest pitch inputs versus time at 13.0 Hz.

It was also noticed that for the responses from 11.0 Hz to 16.0 Hz, the responses were all close in phase to the input. Beyond this region, though, the phase of the response was inconsistent between the different actuation sizes and frequencies.

An example of this loss of phase synchronisation can be found in Figure 57 below, where the gimbal time domain responses to the largest pitch actuations at 35.0 Hz are shown. Although the phase was not as important as the magnitude of the responses, the phase consistency from 11.0 Hz to 16.0 Hz was an indication of some form of control.

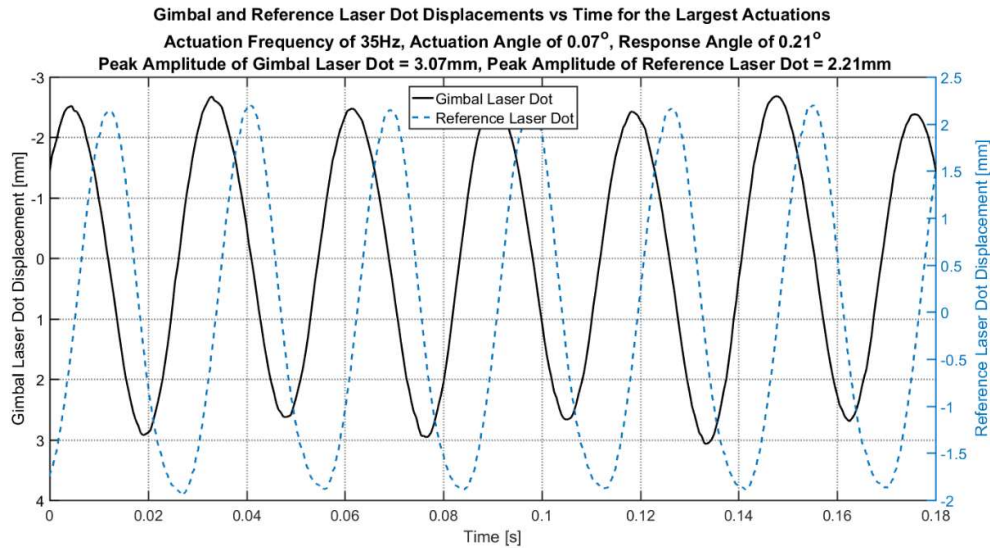


Figure 57. A time domain example of the gimbal's responses to the largest pitch inputs versus time at 35.0 Hz.

6.4.4 The 32.0 Hz to 49.0 Hz Gain Attenuation

The actuation system was a second order system, therefore a drop in gain at higher frequencies was expected, but at much higher frequencies. It is suspected that the improvements in disturbance rejections from 32.0 Hz to 35.0 Hz, and 39.0 Hz to 49.0 Hz were the result of the way in which the gimbal was forced to respond at these actuation frequencies, rather than the gimbal improving in disturbance rejection.

Figure 58 shows the gimbal gain, input and output versus frequency for the largest pitch actuations. The gain is measured against the left y-axis, while the angular inputs and outputs are measured against the right y-axis. Considering Figure 58, the input and output components of the gains provided indications that the largest influence on the magnitude of the gain plots was the gimbal's responses.

The input magnitudes for each set of actuation sizes were compared and found to be consistent in their trends. The magnitude of the input linearly increased for each actuation increase, which was expected.

From Figure 58, between 32.0 Hz and 48.0 Hz, it is clear that even when the input's magnitude is increasing, the gain is still decreasing due to the output. Why the gimbal response was decreasing over this specific frequency range, for all the actuation sizes, was not clear. After considering the time domain data within this frequency range, though, the gimbal appeared to be overpowered by the inputs and was unable to counter, or partially counter, the inputs.

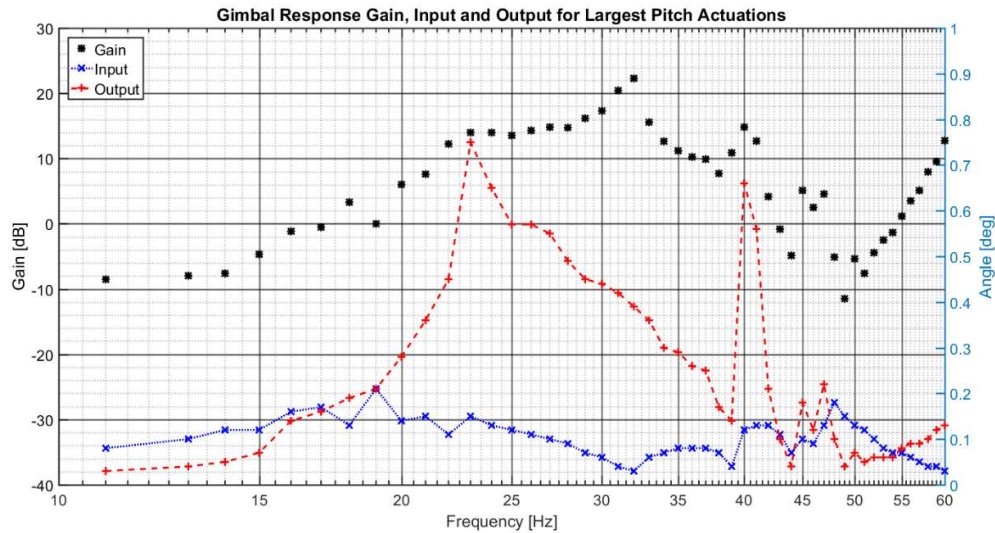


Figure 58. The gimbal response gain, input and outputs versus frequency, for the largest pitch actuations.

6.4.5 Gain Sample Calculation

An example of how the gain and corresponding gain uncertainty is determined is provided below for clarity of the data processing procedure. The actuation frequency is 32.0 Hz and the applied shaker voltage is 3.4 V peak-to-peak, thus the largest actuation amplitude at 32.0 Hz, as seen in Figure 59.

In Figure 59, the absolute displacement versus time signals of the gimbal and reference lasers are provided. The largest amplitude is then determined for each, as indicated in the figure. Note that as the both the displacements were detrended, the mean laser dot positions are zero, as stated in section 4.2.

Equation (45) is used to determine the actuation angle and is from Equation (38) in section 4.2. From the results of the measurement system accuracy tests, the average algorithm error must be taken into account. Therefore, 0.06 mm must be added to the measured amplitude in equation (38).

Equation (46) is used to determine the gimbal response angle and is from Equation (39) in section 4.4. As stated above, the displacement has been detrended, therefore the mean laser dot position is zero. From the results of the measurement system accuracy tests, the measurement system error must be taken into account. Therefore, 0.12 mm must be deducted from the measured amplitude.

Equation (47) is then used to determine the gain of the response and is from equation (40) in section 4.4. The uncertainty of the gain is determined by equation (48), which is from equation (33) in section 2.8 (Figliola & Beasley, 2011). Note that the gain uncertainty value, given in equation (49), is the unitless absolute gain value and is not in decibels.

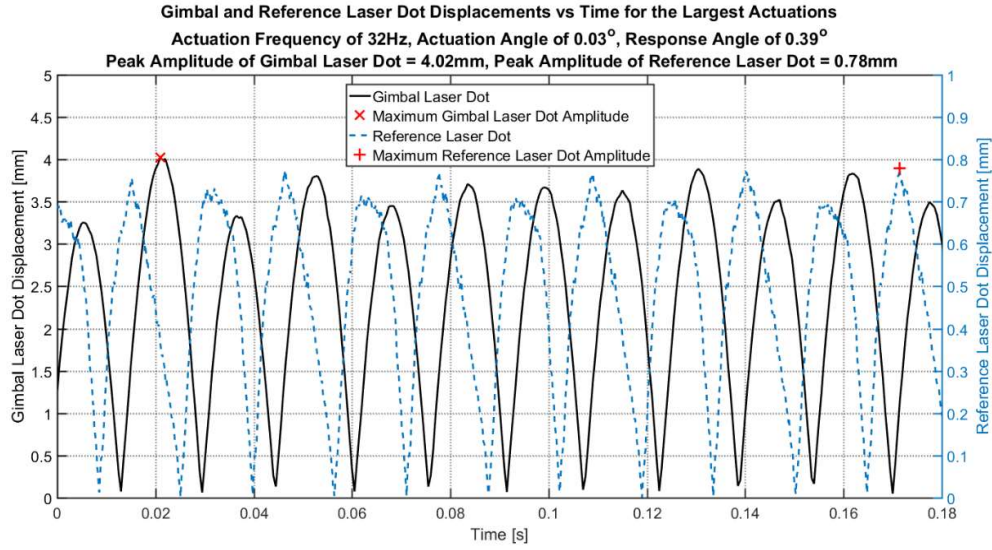


Figure 59. The absolute gimbal response to the largest absolute disturbance at 32 Hz. The displacement of the gimbal laser dot is measured against the left y-axis, while the displacement of the reference laser dot is measured against the right y-axis. Note, the correct, positive y-axis displacement for the gimbal laser dot is actually downwards. For simplicity, though, it was decided to plot the positive y-axis for the gimbal laser dot displacement as upwards.

$$\theta_{\text{Actuation}} = \tan^{-1} \left(\frac{0.78 \text{ mm} + 0.06 \text{ mm}}{1611 \text{ mm}} \right) = 0.03^\circ \quad (45)$$

$$\theta_{\text{Error}} = \tan^{-1} \left(\frac{4.02 \text{ mm} - 0.12 \text{ mm}}{580 \text{ mm}} \right) = 0.39^\circ \quad (46)$$

$$G_{32 \text{ Hz_Largest_Pitch}} = 20 \log \left| \frac{\theta_{\text{Error}}}{\theta_{\text{Actuation}}} \right| = 22.28 \text{ dB} \quad (47)$$

$$u_{G_{32 \text{ Hz_Largest_Pitch}}} = G_{32 \text{ Hz_Largest_Pitch}} \left(\frac{u_{\text{Gimbal}}}{\theta_{\text{Error}}} + \frac{u_{\text{Actuation}}}{\theta_{\text{Actuation}}} \right) \quad (48)$$

$$u_{G_{32 \text{ Hz_Largest_Pitch}}} = \pm 1.77 \quad (49)$$

The uncertainty of the angle of actuation, as seen in equation (50), is determined by the measured reference laser dot displacement uncertainty. It must be noted that the actuation uncertainty is an order of magnitude smaller than the uncertainty of the measurement algorithm in section 4.7, which means that the actuation uncertainty is normally ignored. However, it is still included in the example for clarity.

The uncertainty of the reference laser dot displacement is determined by equation (51). The root sum method, from equation (18) in section 2.8, is used to combine the two measurement uncertainties. The algorithm actuation uncertainty from section 4.7 and the random uncertainty of the variation in the peak displacements of the reference laser dot.

Random error presents itself as the scattering of measured data when repeated measurements are made, under constant operating conditions (Figiola & Beasley, 2011). The uncertainty introduced by random error is quantified by equation (52), which is from equation (15) in section 2.8 (Figiola & Beasley, 2011).

In calculating the t-value in equation (52), the measurement certainty and degree of freedom are required. As stated in Appendix D, the assumed probability is 95%. As stated in section 2.8, the degree of freedom of a measurement is the number of measured points, minus the number of parameters used in determining the measurements.

The number of measured points, or in this case displacement peaks, is twelve. The number of previously determined statistical parameters used in determining the measurements is three. These parameters were the distance of the centre of rotation to the target surface, the average error of the algorithm, and displacement of the support beam.

The random standard uncertainty, as seen in equation (53), is the estimate of the probable range of random error and is from equation (17) in section 2.8.

$$u_{\text{Actuation}} = \tan^{-1} \frac{u_{\text{Reference}}}{1611 \text{ mm}} = \pm 0.002^\circ \quad (50)$$

$$u_{\text{Reference}} = \sqrt{(0.07 \text{ mm})^2 + u_{\text{Peak_Deviation_Ref}}^2} \quad (51)$$

$$u_{\text{Peak_Deviation_Ref}} = t_{12-3,(95\%)} \sqrt{s_{\text{Peak_Deviation_Ref}}^2} \quad (52)$$

$$S_{\text{Peak_Deviation_Ref}} = \frac{S_{\text{Peak_Deviation_Ref}}}{\sqrt{12}} \quad (53)$$

The uncertainty of the response angle, as seen in equation (54), is determined by the measured gimbal laser dot displacement uncertainty.

The uncertainty of the gimbal laser dot displacement is determined by equation (55). The root sum method, from equation (18) in section 2.8, is used to combine the two measurement uncertainties. The algorithm actuation uncertainty from section 4.7 and the random uncertainty of the variation in the peak displacements of the gimbal laser dot. As stated above, the random error of the gimbal laser dot displacements must be taken into account and is quantified by equation (56), which is from equation (15) in section 2.8 (Figiola & Beasley, 2011).

Similar to the actuation t-value, the degree of freedom of the measurement is nine. There are twelve measured peaks and three previously determined statistical parameters used in determining the measurements. These parameters were the distance of the centre of rotation to the target surface, the average error of the algorithm, and displacement of the support beam.

The random standard uncertainty, as seen in equation (57), is the estimate of the probable range of random error, and is from equation (17) in section 2.8.

$$u_{\text{Response}} = \tan^{-1} \frac{u_{\text{Gimbal}}}{580 \text{ mm}} = \pm 0.02^\circ \quad (54)$$

$$u_{\text{Gimbal}} = \sqrt{(0.22 \text{ mm})^2 + u_{\text{Peak_Deviation_Gimbal}}^2} \quad (55)$$

$$u_{\text{Peak_Deviation_Gimbal}} = t_{12-3, (95\%)} \sqrt{S_{\text{Peak_Deviation_Gimbal}}^2} \quad (56)$$

$$S_{\text{Peak_Deviation_Gimbal}} = \frac{S_{\text{Peak_Deviation_Gimbal}}}{\sqrt{12}} \quad (57)$$

6.5 Roll Actuation Results and Discussions

This section covers the results and discussions of the roll actuation tests. Figure 60 and Figure 61 show the peak gimbal response gain plots to the three roll actuation sizes. Figure 60 shows the peak response gains without the uncertainty bounds, while Figure 61 shows the same results with the measurement uncertainty bounds.

Where the uncertainty of a measurement was greater than the magnitude of the measurement, the point was ignored. The individual results for each actuation amplitude for the roll actuations can be found in Appendix G.

As discussed in sections 5.4.2 and 6.1, the responses to roll actuation were expected to be better than the responses to pitch actuations. This is supported by the comparison of the mean gains for the pitch and roll responses. The mean gain for the pitch actuations was 8.95 dB, while the average gain for the roll actuations was 6.10 dB.

Similar to the pitch actuations, the lower frequencies of the roll gains indicate partial countering of the inputs, due to the gain magnitudes. Unlike the pitch actuation tests, though, the gain for the roll actuations starts above 0 dB. In addition, between 10.0 Hz and 14.0 Hz only the gains for the large actuations can be used.

Therefore, it cannot be assumed that the gimbal's gain is always below 0 dB for the remaining actuation sizes between 10.0 Hz and 14.0 Hz. It was noted that the gain attenuation, for the low frequency the roll actuations, extends to 21.0 Hz, compared to 17.0 Hz for the pitch actuations.

Also apparent in Figure 60 are the relatively consistent gain values, in comparison with the gains for the pitch actuations. Where the gain for the pitch actuations varies significantly, the gain for the roll actuations gradually increases. The lack of significant cyclic gain variation suggests that there is a sensitivity to the direction of the actuation.

Between 23.0 Hz and 27.0 Hz, the gains had to be ignored due to their uncertainties being too large. Considering the consistency of the input and its magnitude, as discussed in section 6.4.4, this was suspected to be due to the gimbal. It was found that the magnitude of the gimbal laser dot displacements became smaller than the minimum measurable displacement in this region. Therefore, the uncertainty of the measurements became too large to be trust worthy. The large uncertainties associated with these measurements resulted in the lower measurement uncertainty boundaries becoming negative values; which do not translate to the decibel scale.

It was noted that the peak gain at 31.0 Hz was similar to the 32.0 Hz gain for the pitch actuations. As discussed in section 6.4.2, the device mount IMU cable was suspected to be the source of this. However, as discussed in section 6.4.2, this required further investigation.

Considering the expectation for the increase in gain with actuation size, no consistent relationship between the actuation size and gain is observed.

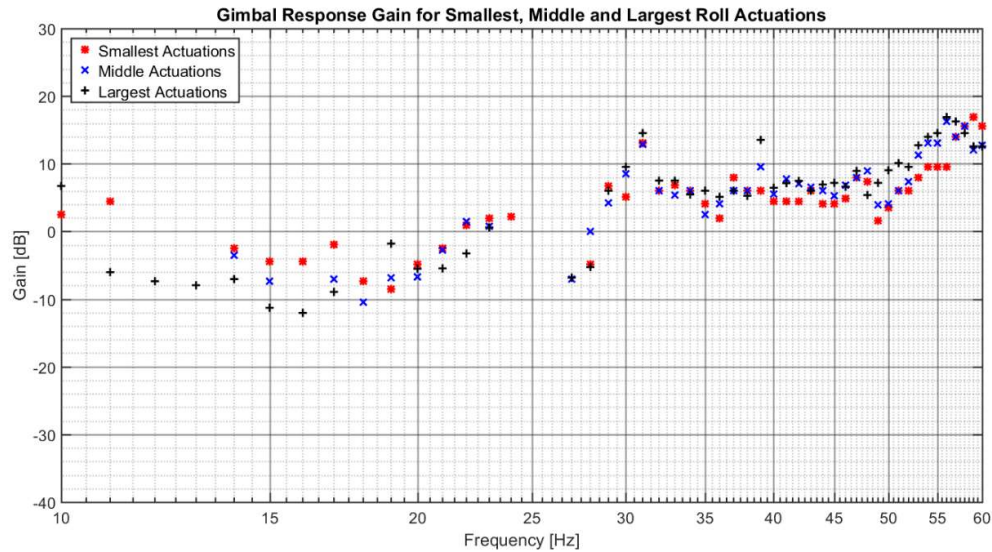


Figure 60. The gimbal response gains to the three different roll actuation sizes.

The gimbal gain resonances that correspond to the natural frequencies of the support structure and actuation plate are summarised in Table 5. Note, T1 and T2 in the table refer to the first and second modal hammer tests respectively.

It must also be noted that there are a noticeable increases in gain for 21.0 Hz and 22.0 Hz in Figure 60, which appear to correlate to the system natural frequencies of 21.8 Hz and 21.9 Hz, identified in section 5.1. However, the inconsistency between the different actuation size gains for 21.0 Hz and 22.0 Hz, were cause for doubt over the correlation to the natural frequencies. Therefore, they were not included in Table 5.

The results from Table 5 indicate that the gimbal is sensitive to the natural frequencies of the support frame and actuation plate, as discussed in section 6.4.1. Therefore, if the gimbal is part of a measurement system, it will need vibration isolation. However, considering the high frequency drone controller vibrations from section 3.1 and the gimbal's responses, the efficacy of the vibration isolation will need to be confirmed.

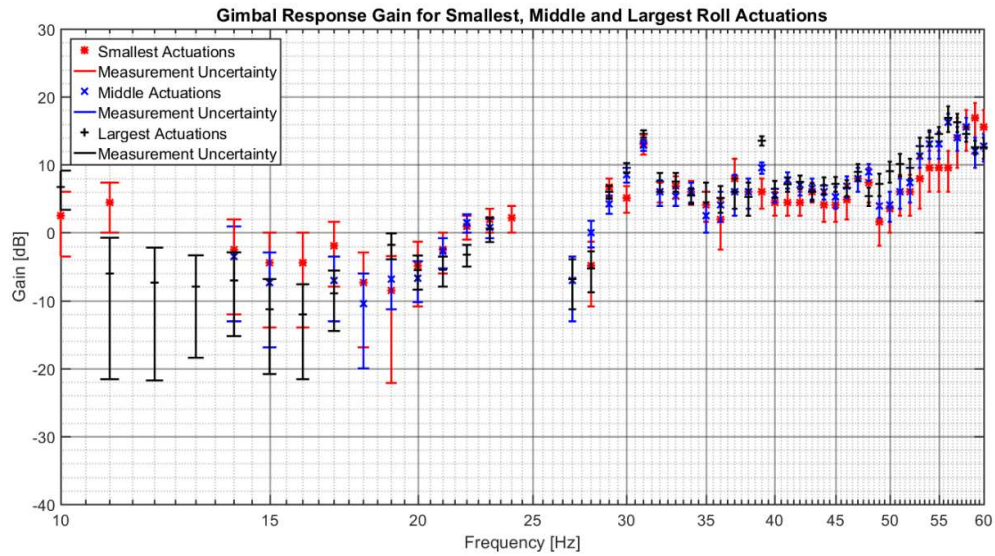


Figure 61. The gimbal response gains to the three different roll actuation sizes with uncertainty bounds. The overlapping of the uncertainty bounds indicate that there is a correlation between the measured values for the three responses.

Table 5. The gimbal gain resonances and corresponding support structure and actuation plate natural frequencies for roll actuations.

The Gain Resonances for the Roll Actuation Tests		
Gain Resonances [Hz]	Support Structure Natural Frequencies [Hz]	Actuation Plate Natural Frequencies [Hz]
29.0	-	28.9 (T1)
39.0	39.1 (T1)	39.1 (T1)
47.0	46.1 (T1 & T2)	46.1 (T1 & T2)

7 Conclusions and Recommendations

The aim of this experimental study was to produce accurate performance data of gimbal pitch responses, to pitch and roll actuations. It was understood that the gimbal would perform well for low-frequency disturbances, as it was designed for use in stabilising a camera. Therefore, the focus was on investigating actuation frequencies outside of the region of superior gimbal control.

The gimbal gain was expected to increase with the actuation frequency and amplitude, peaking at the natural frequencies of the actuation structure. In addition, the responses to roll actuations were expected to produce superior gain attenuation over the gain from the pitch actuations.

It was found that there was no consistent relationship between the actuation size and the corresponding gain. However, there was evidence to suggest that there was a close correlation between the responses of the three actuation sizes, throughout the test frequency range. Aside from the responses to the natural frequencies, the gimbal did not exhibit a consistent increase in gain with frequency.

The gimbal's responses at the support structure and actuation plate's natural frequencies validated the need for vibration-isolation pads, which was expected. Data from drone sensors, mounted to vibration isolation pads, indicated that high frequency vibrations were still detectable. This was seen as a problem, if the gimbal were to be used in a precision measurement system. Therefore, it was suggested that the efficacy of the gimbal vibration isolation be confirmed and was left for further, more detailed investigations in this avenue.

Considering the relative performance of the gimbal, for the two actuation methods, the average gain for the roll actuations was the lowest of the two. Therefore, implying the gimbal responses to roll actuations were overall superior, as expected.

The first noticeable feature in the responses was the gain attenuations at low frequencies, for both actuation methods. These responses suggested that the gimbal was able to counter the disturbances. The time domain data, however, suggested that the gimbal was under partial control. The responses maintained a consistent phase with respect to the input, for almost all the low frequency cases. This was indicative of partial control. The gimbal's responses also became nonlinear towards the peak of the inputs. As the focus was on the peak gimbal responses, these nonlinearities had to be ignored.

The second noticeable feature was the responses at 32.0 Hz and 31.0 Hz, for the pitch and roll actuations, respectively. The support structure and gimbal were ruled out as sources for these responses. Experiment observations at these frequencies noted buzzing noises, which lead to the gimbal IMU cable being suspected of colliding with the gimbal frame. It was thought that the cable vibrating could cause these responses, but this needed proof through an in depth investigation. Therefore, this was left for following investigations.

The third noticeable feature was the difference in the responses for the pitch and roll actuations, between 32.0 Hz and 46.0 Hz. From 32.0 Hz to 46.0 Hz the gains

for the pitch responses dropped significantly, while the gains for the roll actuations did not. It was suspected that the drop in the gain was due to the gimbal being forced to respond in this manner, rather than the gimbal being able to perform better.

The determination of the mechanics that caused these responses was not the focus of the study. In addition, the interactions of the variables that affected the gimbal's performance were complex and required an in depth analysis. Therefore, it was decided that a separate and more detailed study would be needed in this region, and was left for further studies.

Considering the overall results of the experimental investigation, accurate performance data, for increasing disturbance frequencies and amplitudes, was produced. This data provided different insights into the gimbal's performance, which were not available before. In addition, the investigations also provided insights into possible cross-correlations of roll inputs on pitch responses, which were not expected to be as prevalent as observed.

A key limitation in the investigation was the inability to reliably investigate above 60.0 Hz, to confirm the second gain peak at 64.0 Hz for the pitch actuations. For the measurement of the actuations, this could have been avoided by using an accelerometer and omega integration, as discussed in section 5.2. However, as detailed in section 5.2, this required significant amounts of fine tuning of the results for each experiment. When compared to an accurate and established method of measuring the displacements with an IDT, however, it was decided to not pursue using the accelerometer any further.

This frequency limitation did effect the analysis of the results later on, as producing FFTs from the laser dot displacement data became difficult and unreliable, due to the relatively small number of samples.

Even with the frequency limitation taken into account, however, it remains that the gimbal was unable to function properly approaching 60.0 Hz, for both actuation methods. Therefore, data beyond this actuation frequency for a gimbal without vibration isolation, would not have revealed more than what has already been produced.

Importantly, the results indicated that the gimbal must also be considered as a source of vibrations and dynamics. An off-the-shelf gimbal can be optimised for precision measurements, but the results suggest that the gimbal can be significantly affected by vibrations of its own cables, or flexing of its own frame.

It is recommended that further research be done to produce frequency domain performance data for the roll and yaw responses of the gimbal, under single-axis and multiple-axis actuations. Specifically, in the regions where known blade pass and drone frame frequencies are observed.

Research into the efficacy of the vibration isolation pads, provided by gimbal manufacturers, is also recommended. In addition, it is recommended to determine the source of the gimbal's gain response dropping between 32.0 Hz and 46.0 Hz for pitch actuations.

For these research continuations, the following points are recommended:

1. The use of high-speed cameras in capturing the gimbal's responses. The high-speed footage of both the laser's movements and gimbal's movements, proved invaluable in solving some of the unexpected dynamics observed.
2. The device mount IMU and power cables must be prevented from oscillating, and exerting tension, or compression, on the gimbal. As the gimbal is in a fine-tuned balance, the smallest forces can affect its responses.
3. The same actuation and measurement systems must be used to actuate the gimbal and measure its responses from below 10.0 Hz and above.
4. The natural frequencies of the actuating structure, or drone, must be determined before the testing of the gimbal.

A. Drawings and Dimensions

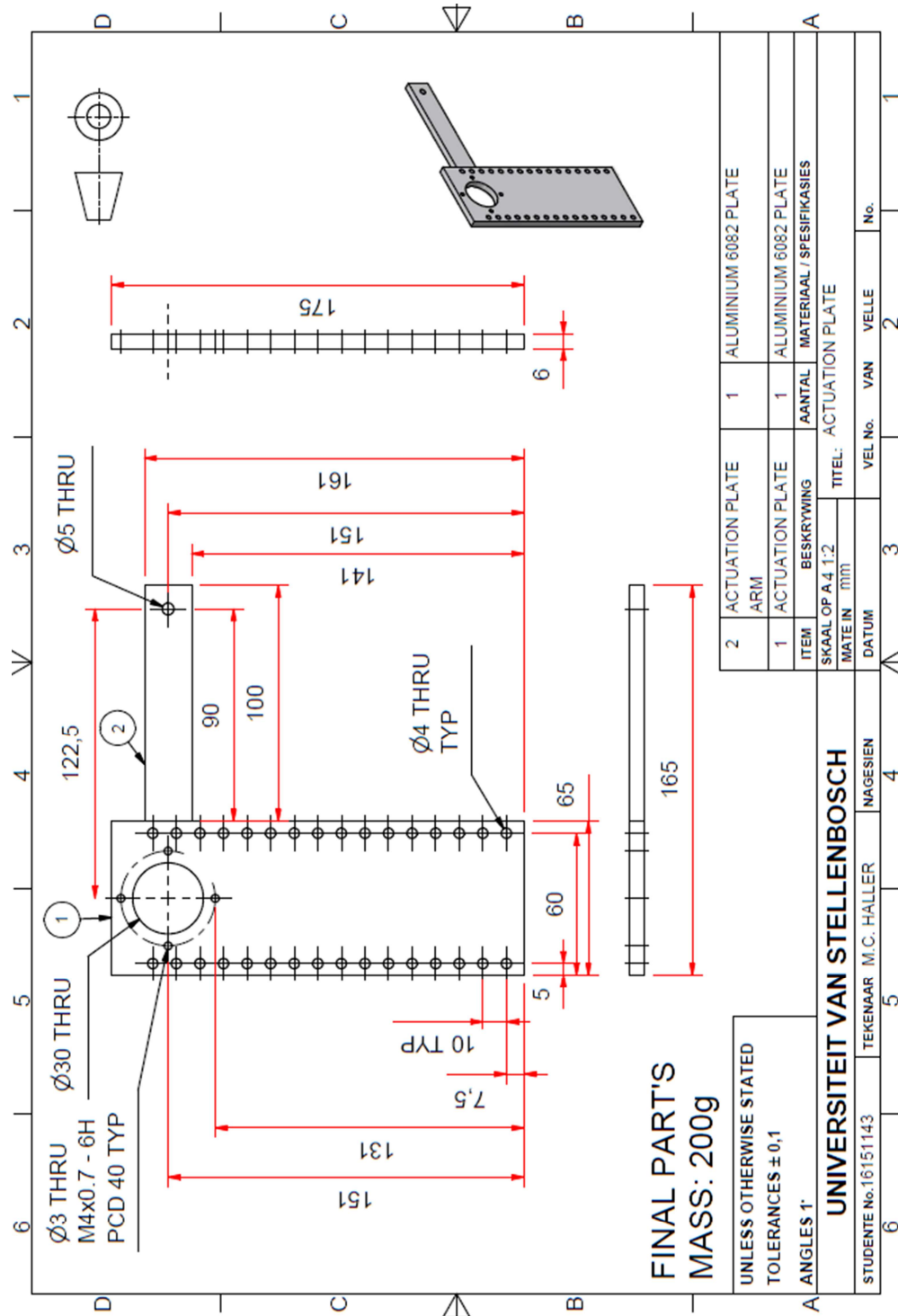


Figure 62. Actuation plate dimensions and material.

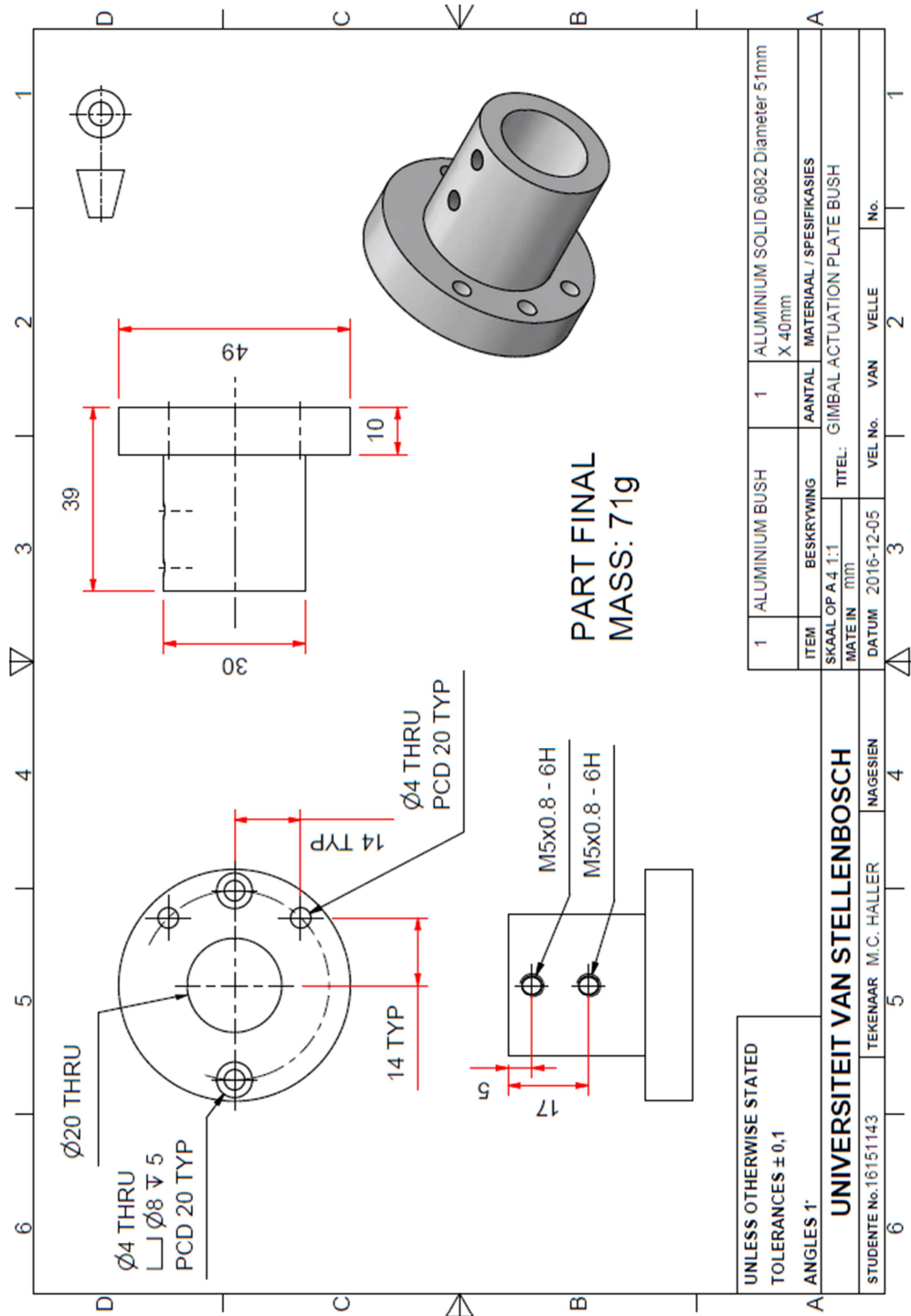


Figure 63. Actuation plate bush dimensions and material.

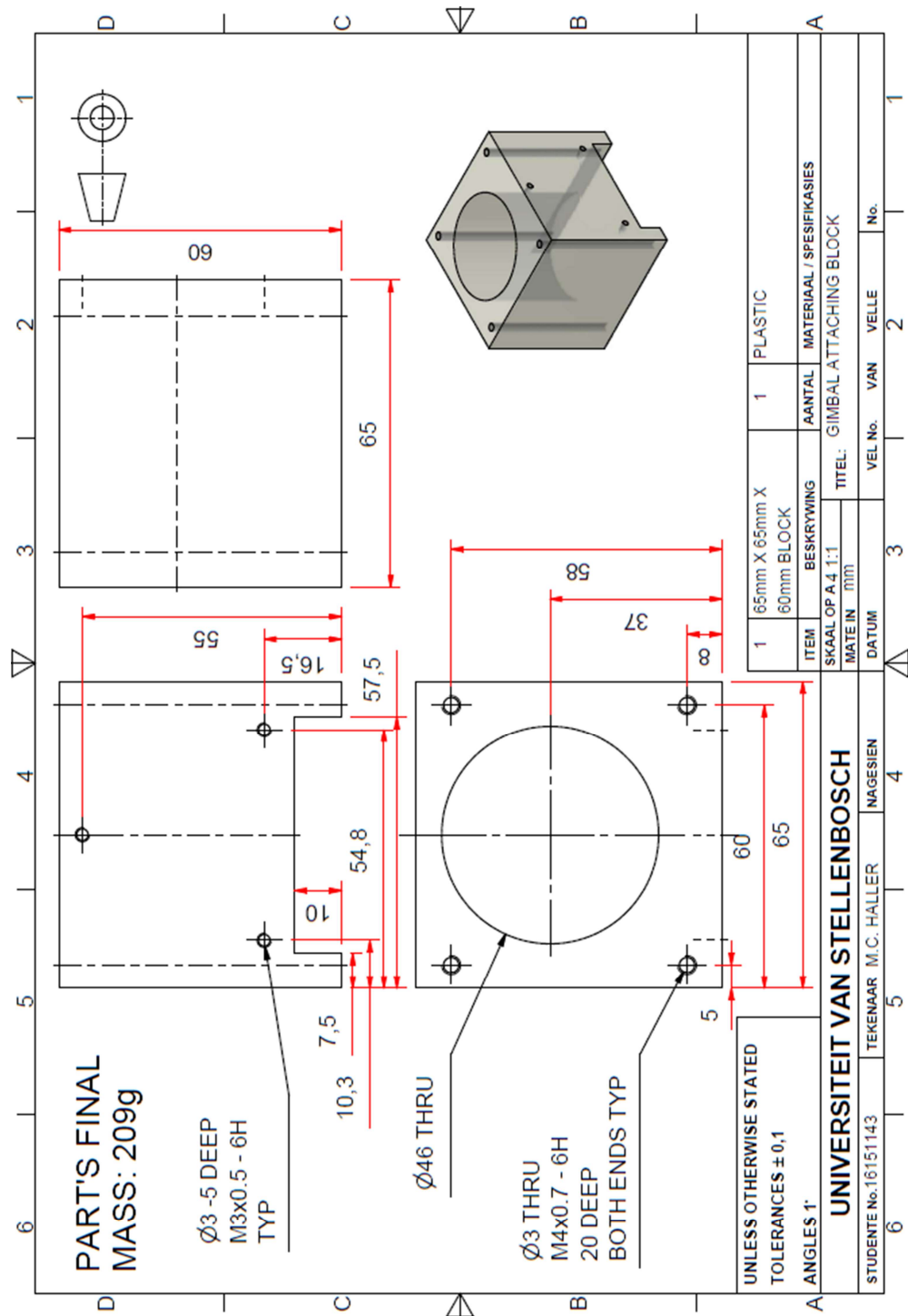


Figure 64. Gimbal attaching block dimensions and material.

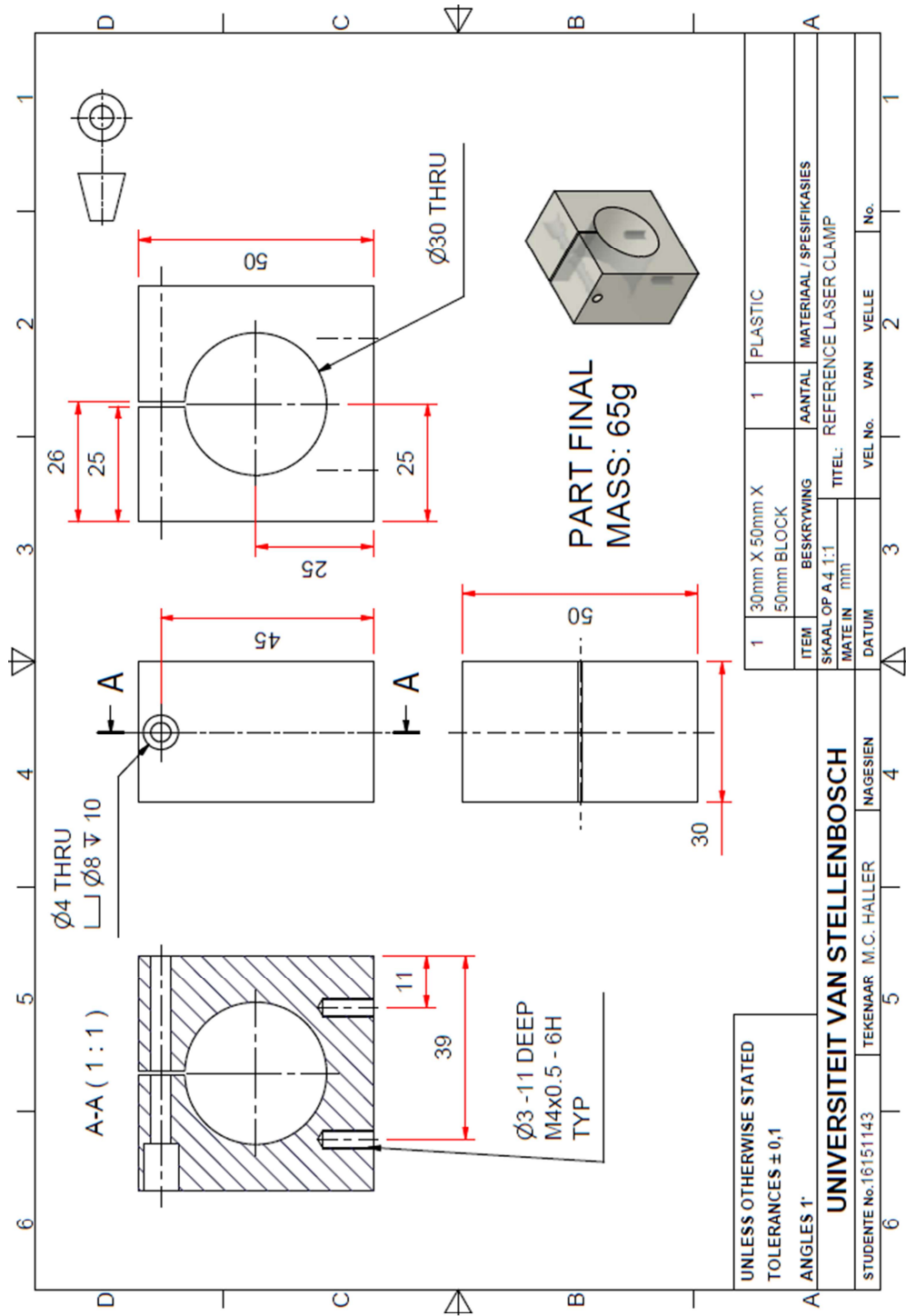


Figure 65. Reference-laser-clamp dimensions and material.

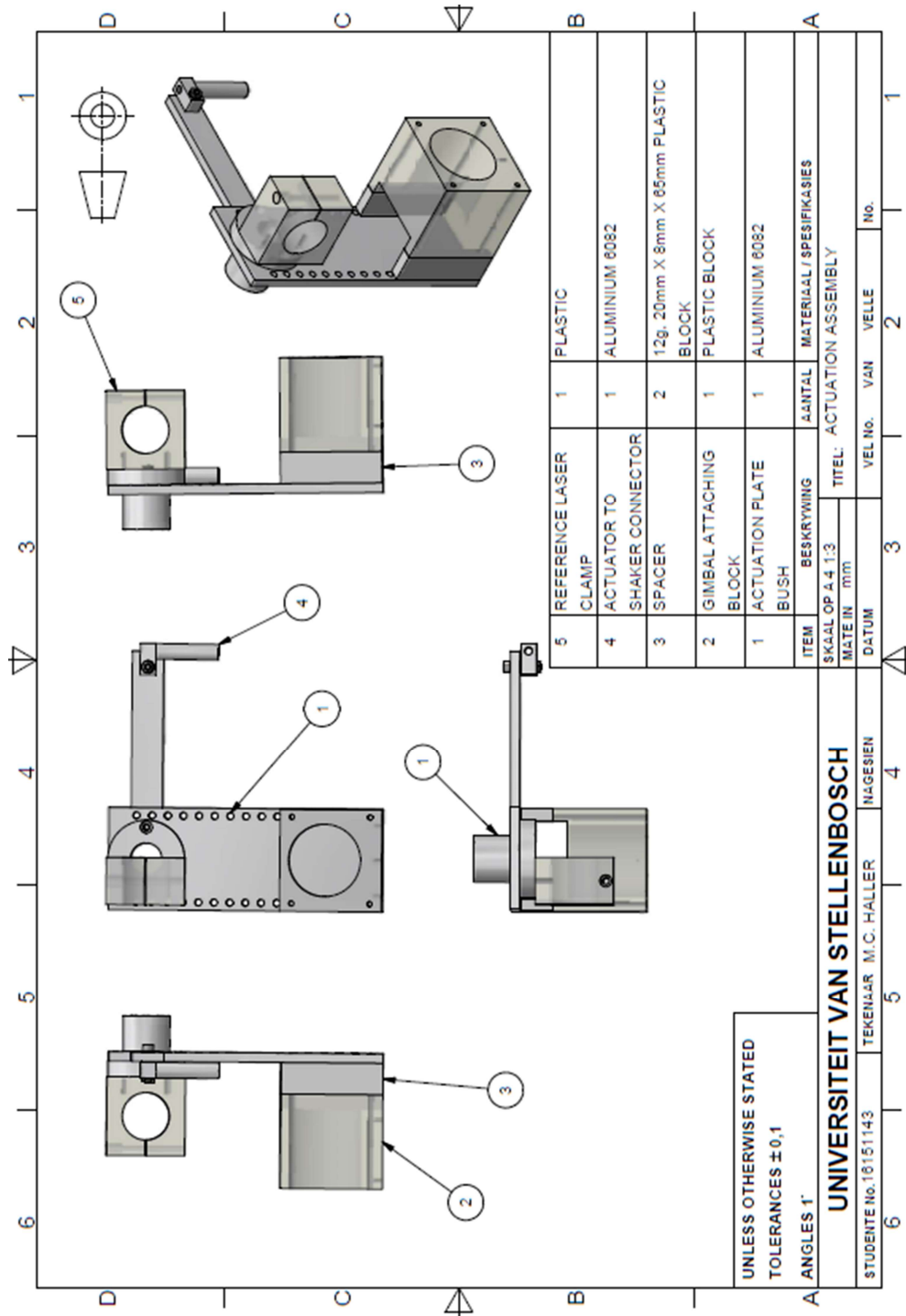


Figure 66. Actuation assembly

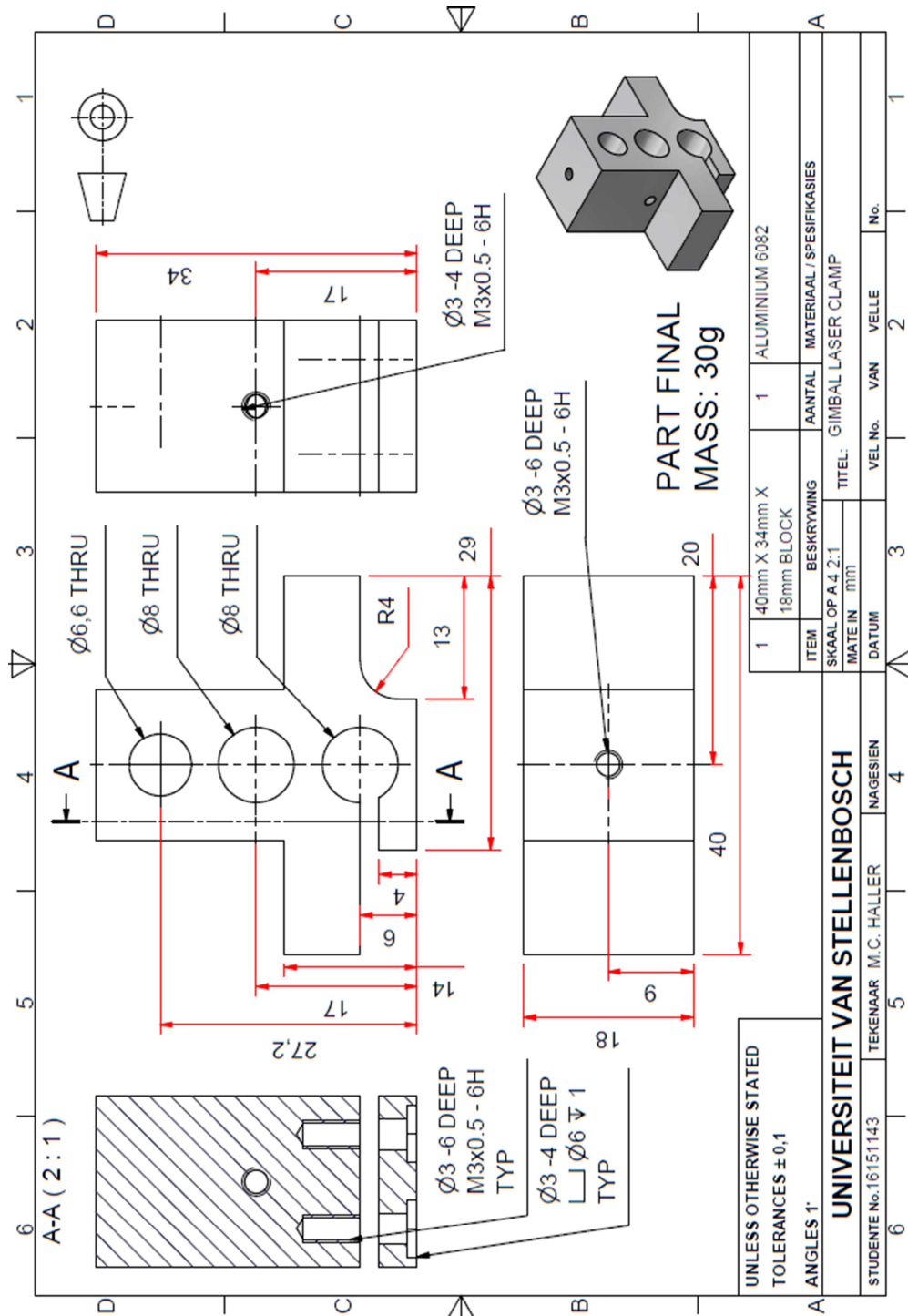


Figure 67. Gimbal laser clamp dimensions and material.

B. Tracking Algorithm Verification Setup Parameters

B.1 Camera Calibration Pattern

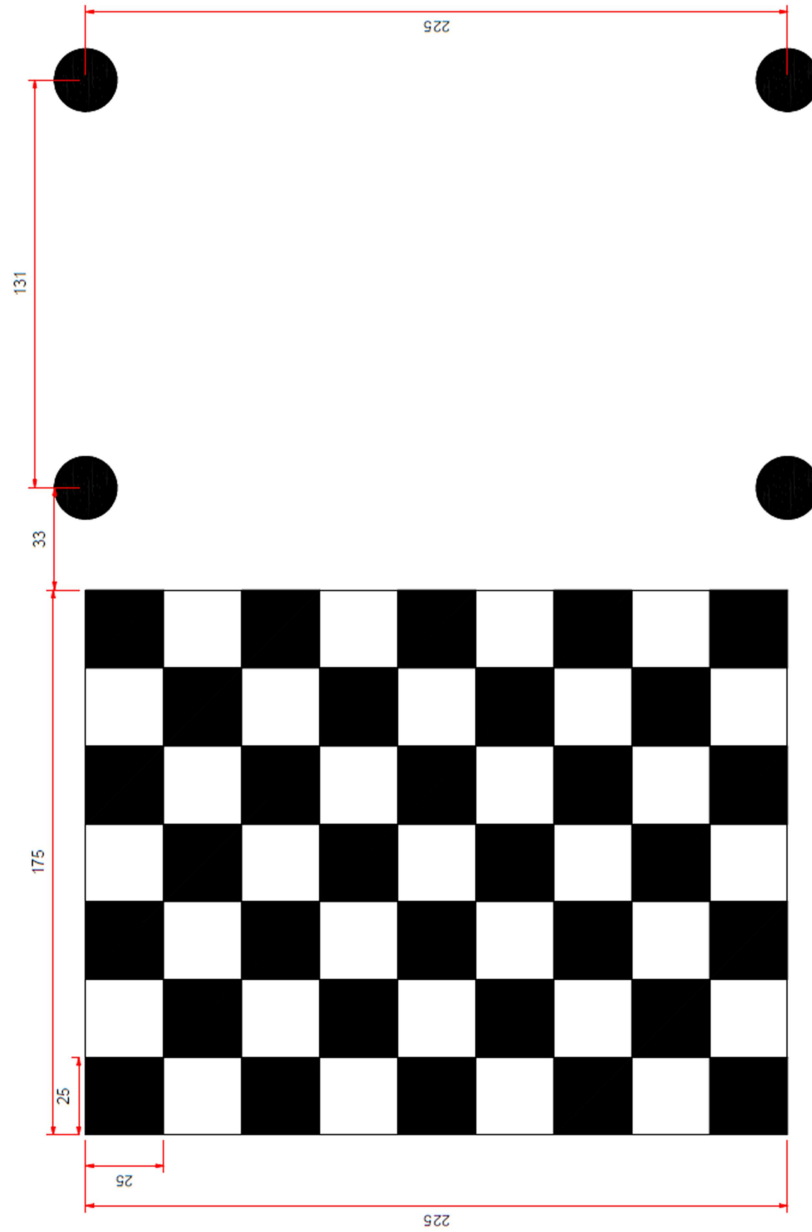


Figure 68. Calibration board pattern. Note that the measurement units are in millimetres and that the drawing is not to scale

B.2 Verification Test Plan

Table 6. Laser dot tracking algorithm accuracy verification test plan

Laser Dot Tracking Algorithm Verification Test Plan							
2000 Frames per Second				10 000 Frames per Second			
Major Axis [1280 Pixels]		Minor Axis [1024 Pixels]		Major Axis [528 Pixels]		Minor Axis [329 Pixels]	
Step Size [mm]	Spacing [mm]	Step Size [mm]	Spacing [mm]	Step Size [mm]	Spacing [mm]	Step Size [mm]	Spacing [mm]
0.02	29.98	0.02	29.98	0.02	21.8	0.02	21.8
0.1	29.9	0.1	29.9	0.1	21.1	0.1	21.1
0.5	29.5	0.5	29.5	0.5	20.7	0.5	20.7
1.0	29	1.0	29	1.0	20.2	1.0	20.2
5.0	-	5.0	-	5.0	19.2	5.0	19.2

B.3 Camera Setup for Verification Tests

Table 7. Laser dot tracking algorithm accuracy verification test system setup parameters

Laser Dot Tracking Algorithm Verification Test System Setup Parameters		
Camera Frame Rate [fps]	2000	10 000
Lens Field of View [deg]	84.1	84.1
Camera Distance to Target Surface From Camera Lens Base [mm]	453.5	486.5
Camera Exposure Setting [us]	495.938	95.938
Camera Aperture Setting [mm]	11	11
Camera Zoom Setting [m]	0.5	0.5
Camera Angle to Target Surface (Top View) (CW =negative, CCW = positive)[deg]	72	70
Camera Angle to Target Surface (Right Side View: CW=negative, CCW=positive) [deg]	-0.6	-3.7
Camera Height off Ground [mm]	943	1030
Distance of Centre of Laser to Target Surface [mm]	1232	1160
Calibration Board Angle (Right Side View) [deg]	3CCW,	6CCW
Calibration Board Angle (Top View) [deg]	0.42CW	2.86CCW

B.4 Accelerometer Sensitivities

Table 8. Support frame and actuation plate mounted accelerometers' sensitivities

Mounted Accelerometer Sensitivities	
Accelerometer Number	Sensitivity [mV/g]
1	97.6
2	98.5
3	95.1
4	101.107
5	102.3
6	102.3

C. Initial Camera Position for Angular Resolution

Figure 69 provides the visual example of the camera Field of View (FOV) which was defined by each camera's lens. The FOV was 84° and diagonal, therefore the angle between the two dashed lines from the camera to the two opposite corners of the target image surface was 84° . As the number of pixels per axis depended on the chosen camera frame rate, the initial camera-to-target surface distance determining equations listed below refer to Figure 69's generic variable names.

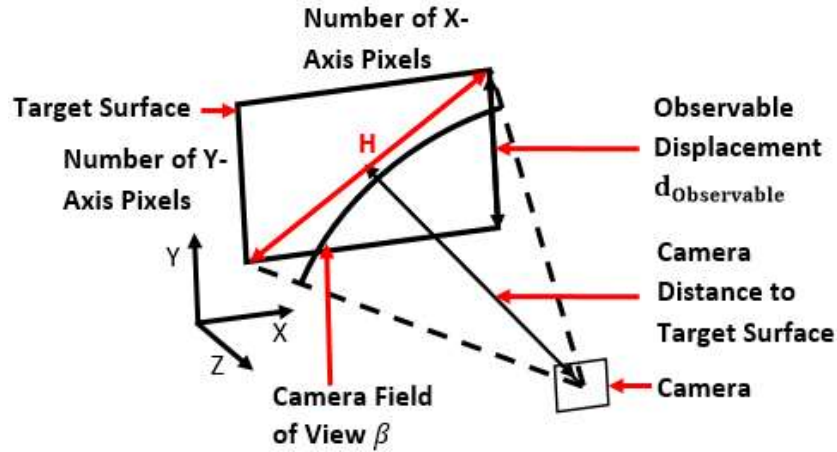


Figure 69. The camera Field of View (FOV) was determined by the attachable lens. The FOV was 84.1° and diagonal, therefore the angle measurement specified the angle between the dashed lines. The length H is the diagonal bisector which extends between the two opposite corners of the image.

Working from the required measurement system angular resolution, in equation (58), the required image subpixel resolution, to produce the required angular resolution, would be determined for the specific camera frame rate, see equations (59) and (60). Each axis of the image has a different resolution, therefore the smallest subpixel resolution that can be achieved will vary, depending on the image axis used.

$$\alpha_{\text{Initial_Guess}} = \frac{1 \text{ mrad}}{5} = 0.2 \text{ mrad} \quad (58)$$

$$\alpha_{\text{Initial_Guess}} = \tan^{-1} \left(\frac{\text{Image_Res}_{\text{sub-pixel@fps}}}{D_{\text{laser}}} \right) \quad (59)$$

$$Image_Res_{sub-pixel@fps} = \tan(\alpha_{Initial_Guess}) D_{laser} \quad (60)$$

As stated by Song et. al, the Barycentre algorithm, in the worst case scenario, could produce a sub-pixel accuracy of 0.5 of a pixel. This was then used in equations (61) and (62) to determine the minimum resolution required to achieve the required sub-pixel accuracy.

$$Image_Res_{sub-pixel@fps} = Image_Res_{@fps} 0.5 \quad (61)$$

$$Image_Res_{@fps} = \frac{Image_Res_{sub-pixel@fps}}{0.5} \quad (62)$$

If the number of pixels in an image axis and the resolution per pixel were known, the maximum observable displacement could be determined by using equations (63) and (64). As the gimbal was prevented from being able to yaw, the only displacement to be measured was the vertical displacement of each laser dot, which through trigonometry was understood to be a function of the FOV diagonal distance H, see equation (65). Therefore, using equations (63) and (65), and the known number of pixels per image axis, the required observable vertical laser dot displacement could be described.

Considering Figure 69 again, the distance H is the maximum observable diagonal displacement given the camera distance to target and the FOV, see equation (66). Therefore, this equation could be used to infer the required camera-to-target distance to achieve the required angular resolution based on the laser-to-target surface distance, the FOV and the frame rate resolution, see equation (67).

$$d_{Observable} = Image_Res_{@fps} No\#. Pixels \quad (63)$$

$$No\#. pixels = \text{Number of Image Axis Pixels} \quad (64)$$

$$d_{Observable} = H \sin \left(\tan^{-1} \frac{No\#. Y - Axis Pixels}{No\#. X - Axis Pixels} \right) \quad (65)$$

$$H = 2 D_{\text{Camera_@fps}} \tan\left(\frac{\beta}{2}\right) \quad (66)$$

$$D_{\text{Camera_@fps}} = \frac{2 \tan(\alpha_{\text{InitialGuess}}) D_{\text{laser}} \text{No\#. Axis Pixels}}{2 \tan\left(\frac{\beta}{2}\right) \sin\left(\tan^{-1} \frac{\text{No\#. Y - Axis Pixels}}{\text{No\#. X - Axis Pixels}}\right)} \quad (67)$$

As the pixel axis densities were different for each axis in the image, it was decided to base the required camera-to-target surface distances on the lower of the two image axis pixel densities as a worst case scenario. For the camera operating at 10 000fps the y-axis pixel count was 396 pixels, while the camera operating at 2000fps had a y-axis pixel count of 1024 pixels. The camera-to-target distances needed to achieve the required angular resolutions, as a function of the above mentioned axis pixel counts, can be found in equations (68) and (69).

$$D_{\text{Camera_@ 10 000fps}} = 234 \text{ mm} \quad (68)$$

$$D_{\text{Camera_@ 2000fps}} = 212 \text{ mm} \quad (69)$$

At these distances, though, the expected peak-to-peak laser displacement filled a relatively small portion of the image and an insufficient number of calibration blocks could be seen in each image to achieve a proper calibration. Therefore, it was decided to find the closest point to which the camera could be mounted, while still being able to capture the full laser dot displacements and sufficient number of calibration blocks.

In the error simulations, detailed in Appendix D.3, the actuation system offsets and gimbal offsets were considered. For the worst case scenario, where both the gimbal and actuation system peak offsets occur, the peak gimbal laser dot position was calculated to be close to 148 mm. Therefore, the maximum expected peak gimbal laser dot displacement from rest was designed for 150 mm.

The cameras were shifted away from the target surface until the necessary laser displacement and number of checkerboard blocks could be captured. For the camera to monitor the gimbal mounted laser, the distance to target surface was 453.5 mm, while the reference laser monitoring camera distance to target surface was

486.5 mm, as seen in Figure 70 and Figure 71. The corresponding theoretically achievable angular resolution for each frame rate was then determined.

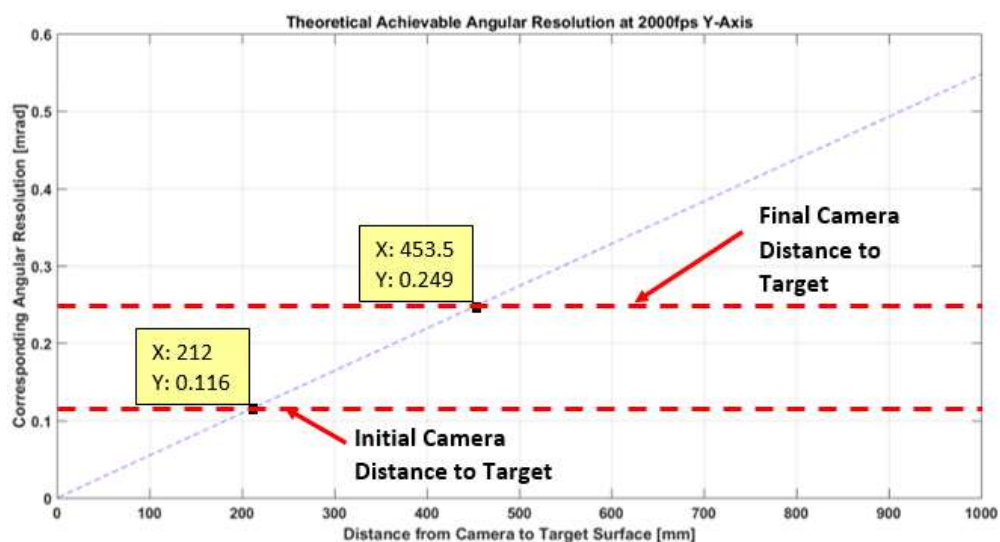


Figure 70. The theoretical camera sub-pixel angular resolution for the image y-axis that can be achieved by placing the camera 453.5 mm away from the target surface and operating it at 2000fps.

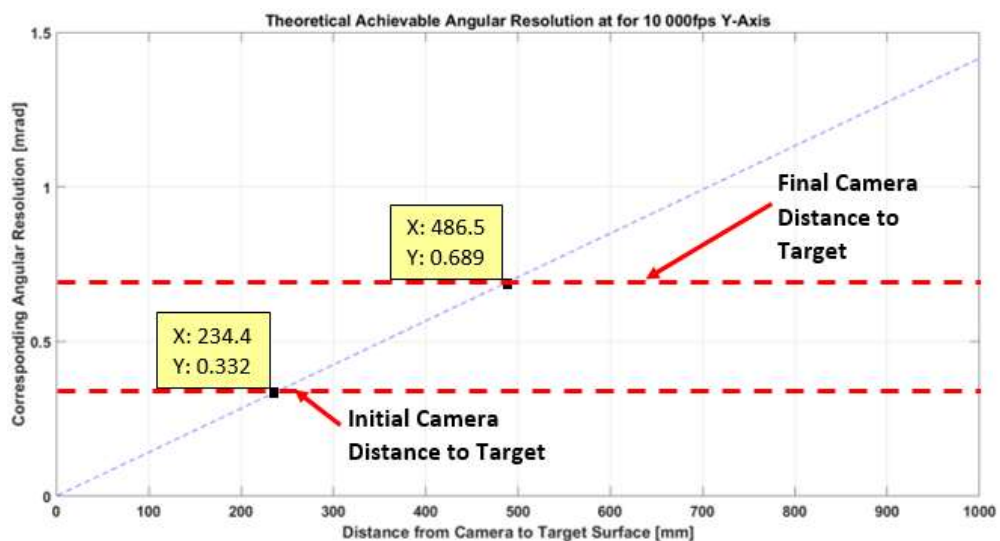


Figure 71. The theoretical camera sub-pixel angular resolution for the image y-axis that can be achieved by placing the camera 486.5 mm away from the target surface and operating it at 10 000fps.

The effect of camera misalignment, or purposeful misalignment as depicted in Figure 72, were also considered as possible sources of significant error due to the stretching of pixels over a larger distance for more acute camera angles. The

concern was that significant resolution would be lost near the far side of the image. This was seen especially if operating near the far end of the image away from the region of camera focus, where checkerboard lines would not be clearly defined in an image. Results from the laser dot tracking and displacement measuring experiments, discussed in section 4.7, seemed to indicate that this and other out of focus effects severely affected the achievable accuracies in these regions.

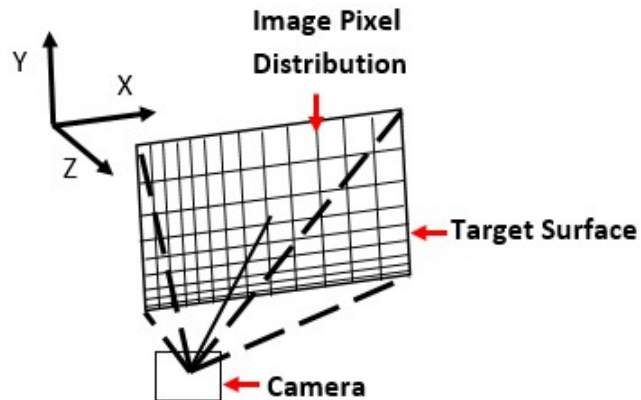


Figure 72. An example of an angled camera pixel distribution, where the pixels that are the closest to the camera are compressed, providing improved resolution. The pixels furthest from the camera are stretched, thus reducing the image resolution in this region.

D. Gimbal Actuation and Gimbal Response Tracking Error and Uncertainty Analyses

As no setup can ever be perfectly aligned, or balanced, it was necessary to consider the effects of system errors, for both the actuation system and gimbal response measuring, on the accuracy of the final results. Therefore, this chapter discusses the sources of the measured disturbance and gimbal response errors, discusses the Monte Carlo simulations, the uncertainty propagation analysis and finally the effects of these errors on the measurement uncertainties.

The support frame angular offset was considered to be any frame pose angle deviating from ideal equilibrium at rest and from an expected minimum, or maximum, position when oscillating, as discussed in section D.1. Gimbal angular offset was considered to be any angular response, or pose, other than that expected from an ideal gimbal response, as discussed in section 4.4.

For the reprojection errors, determined when the camera was setup and calibrated before the main experiments, the inclinometer, range finder and lasers' bore sight errors, the stated accuracies of these values were assumed to be to a confidence interval of 95%.

D.1 Actuation System Error Sources and Resulting Uncertainty Contributions

The error sources for the gimbal base actuation determination system come from seven sources, see Figure 73.

1. The accuracy verification tests.
2. The displacement profile assumption for the reference laser, as discussed in section 4.2.
3. The positioning of the camera for the experiment.
4. The reference laser bore site error.
5. The constant pitch offset of the support frame and actuation plate.
6. The constant roll offset of the support frame and actuation plate.
7. The constant yaw offset of the support frame and actuation plate.
8. The reference laser distance to target from its centre of rotation.
9. The active roll offset of the actuation plate.
10. The active yaw offset of the actuation plate.

The uncertainty introduced by the verification tests are not discussed here as they have been covered in section 4.7, but as shown in section 0 were taken into account using the root sum squared method. Note that, "Support and Actuation Frame Active Pose", in Figure 73 is referring to the change in frame and actuation plate poses during an experiment. This does not refer to the actuations, such as pitching or rolling, but rather undesired frame movements during an experiment.

For the support frame and actuation plate, the distance to target and initial pose in yaw, roll and pitch, were assumed to remain constant throughout the duration of

each experiment. The same was assumed for the bore sight error of the reference laser, the accuracy of the verification tests and the reprojection errors of the camera calibration. In addition, it was recognized that the reference laser dot displacement was affected by the combination of these five variables and so it was understood that each variable had a functional relationship with the reference laser dot displacement.

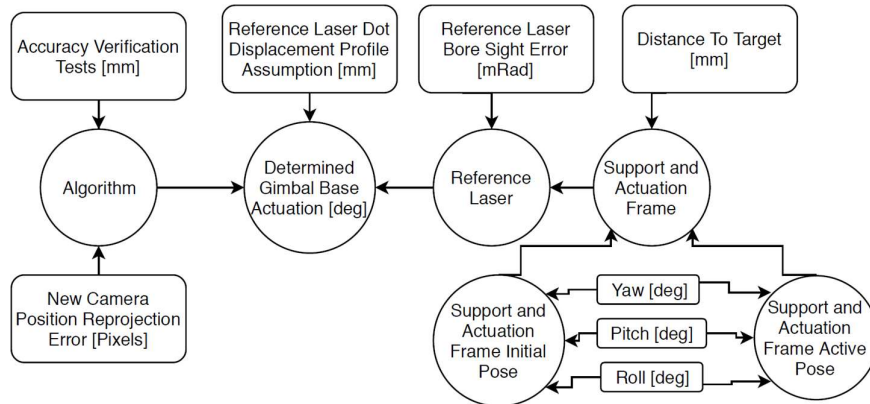


Figure 73. The error flowchart for the reference laser. There are seven sources of error for the reference laser starting with the algorithm used to track and measure the reference laser dot's displacements. The assumed right angled-triangle swing, discussed in section 4.2, introduces an error in the determined actuation angle. The reference laser, as discussed in section D.1.3, has a bore sight error, which causes a difference between the desired position and the true position of the reference laser dot. The support and actuation frames inherently have pose offsets, in static and dynamic conditions, which affect how the laser will be oscillated and therefore results in a difference between the perceived and true actuation angle.

D.1.1 Displacement Profile Assumption

The uncertainty introduced due to the assumed reference laser dot displacement profile was determined through using Monte Carlo simulations, equation (15), equation (25), equation (17) and a required certainty of 95% to determine the degrees of freedom of the t-value, which provided the uncertainty bound for equation (70).

It was recognized that the difference between the true actuation angle and the determined actuation angle, was a function of the support frame and actuation plate yaw offset, pitch offset, roll offset, reference laser distance to target surface and reference laser bore sight error. Therefore, the uncertainties associated with these variables would have functional relationships with the difference

Each variable had a specific functional relationship with the assumption performance. Therefore, they were related, implying that equation (24) in section 2.8 needed to be used to determine the random uncertainty. Each variable's errors were randomly chosen, resulting in the standard deviations of the variables, $s_{\bar{x}_t}$ in equation (71). The functional relationships, or the sensitivity indexes see equation

(22) in section 2.8, each variable had with the displacement was determined by the change in the laser dot displacement, for the change in the variables value, see equation (72) (Figiola & Beasley, 2011).

$$u_{\text{Reference_Assumption}} = 1.96 \overline{s_{\text{Reference_Assumption}}} \quad (70)$$

$$\overline{s_{\text{Reference_Assumption}}} = \sum_{i=1}^5 \sqrt{(\theta_{x_i} s_{\bar{x}_i})^2} \quad (71)$$

$$\theta_{x_i} = \frac{\overline{\partial \text{Displacement_Difference}_{\text{Reference}}}}{\partial \bar{x}_i} \quad (72)$$

D.1.2 New Camera Position Error

If the distance from the camera to the target is maintained, but the camera orientation is altered with respect to the target surface, the algorithm performance will not be affected. The orientation of the x and y-axes, with respect to the camera, are determined through the calibration process, as discussed in section 2.3.

Therefore, the only error introduced in this case is from the calibration algorithm's accuracy with determining the key positions of the calibration board, called the reprojection error. The reprojection error is the difference between the detected feature in a calibration image and its projection, in world co-ordinates, onto the same image (MathWorks, 2016).

If the distance to the target surface is affected, however, then the resolution of the image will change and therefore the accuracy of the algorithm used. Therefore, the only errors that must be taken into account are the reprojection error and the camera distance to the target surface. The uncertainty this reprojection error introduces is described by equation (73), as the error determined here is produced by a reliable algorithm and is assumed to have a certainty of 95%.

The uncertainty introduced by the error in the camera distance to the target surface is described by equation (74). As the camera distance to target is determined by two distance measurements, by the same device, the errors are correlated. This requires the use of equation (26) in section 2.8, resulting in equation (75). The sensitivity indexes can be found in equations (76) and (77), where they are the ratio between the change in the smallest measurable laser dot displacement, to the change in distance to camera target surface.

$$u_{\text{Reference_Reprojection}} = \frac{b_{\text{Reference_Reprojection}}}{2} \quad (73)$$

$$u_{\text{Reference_Camera_Distance}} = 1.96 \overline{b_{\text{Reference_Camera_Distance}}} \quad (74)$$

$$= \sqrt{\frac{\overline{b_{\text{Reference_Camera_Distance}}}}{\left((\theta_{\text{R_D1}} + \theta_{\text{R_D2}}) 0.5 \text{ mm} \right) + 2 \cdot (\theta_{\text{R_D1}} \theta_{\text{R_D2}}) (0.5 \text{ mm})^2}} \quad (75)$$

$$\theta_{\text{R_D1}} = \frac{\overline{\delta \text{Displacement_Resoution}_{\text{Camera}}}}{\delta D_{\text{Camera_Right_Distance}}} \quad (76)$$

$$\theta_{\text{R_D2}} = \frac{\overline{\delta \text{Displacement_Resoution}_{\text{Camera}}}}{\delta D_{\text{Camera_Left_Distance}}} \quad (77)$$

D.1.3 Reference Laser Bore Sight Error

Laser bore sight error is the misalignment of the laser beam and the centre line of the laser barrel, resulting in the laser beam pointing in a direction that makes an angle ψ with the laser barrel centre line, as shown in Figure 74. As the reference laser bore sight error could not be determined, it introduced an uncertainty into the displacement of the reference laser dot, as it would cause the laser beam to deviate from the ideal, perpendicular direction onto the target surface. The bore sight error was stated to be smaller than 3 mrad, therefore the worst-case scenario was assumed, which meant that the magnitude of the bore sight error was always 3 mrad.

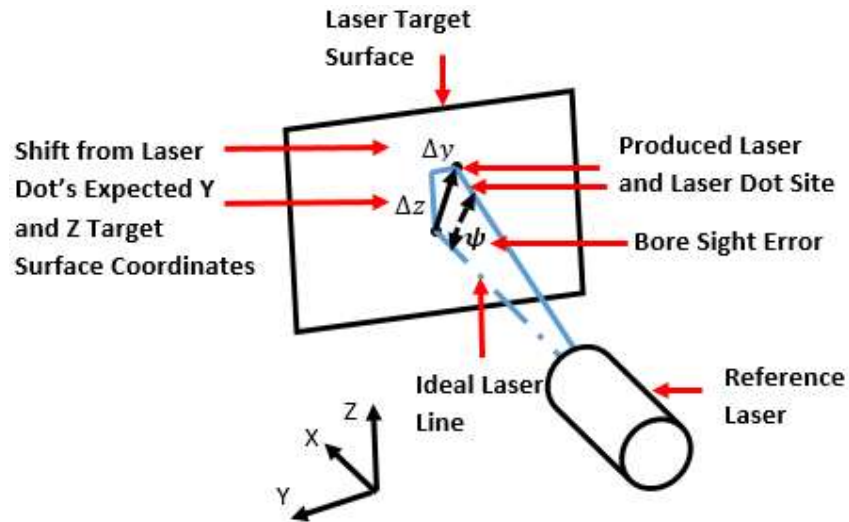


Figure 74. An example of laser bore sight error, where the laser dot's position on the target surface deviates from the expected laser dot location, due to the laser light line not shining in a parallel direction to the laser barrel.

The uncertainty introduced due to the reference laser bore sight error, with a 95% certainty, is described by equation (78). Similar to the displacement profile assumption in section D.1.1, the difference between the true and determined reference laser dot displacement was a function of the boresight error. Therefore, as in section D.1.1, to determine the uncertainty introduced on the displacement of the reference laser dot, the standard deviation of the displacement, see equation (79), was determined by using the average displacement difference and the average change in the bore sight error, see equation (80) (Figiola & Beasley, 2011).

$$u_{\text{Reference_Bore_Sight}} = 1.96 s_{\text{Reference_Bore_Sight}} \quad (78)$$

$$s_{\text{Reference_Bore_Sight}} = \theta_{\text{Disp_Bore_Sight}} 1.5 \text{ mRad} \quad (79)$$

$$\theta_{\text{Disp_Bore_Sight}} = \frac{\overline{\delta \text{Displacement_Difference}_{\text{Reference}}}}{\delta \psi_{\text{Reference_Bore_Sight}}} \quad (80)$$

Following the results of the Monte Carlo simulations in section D.3 though, the effect of the bore sight error on the determination of the actuation angle was found to be negligible. The reason for this was that the reference laser did not roll on the laser barrel centre axis during the experiments, which did occur for the gimbal laser and is discussed in section D.2.1.

D.1.4 Support Frame Constant Pitch Error

Pitch offset was considered to be any combination of base plate, support frame or actuation plate pitch angle that would cause the reference laser beam, at equilibrium, to not shine perpendicular to the target surface. Concerning the actuator plate, the pitch offset was considered as there was no controller to ensure consistent shaker stroke length. This could then result in the shaker consistently applying a larger stroke length for the front swing than the back swing, or vice versa, due to heavier loads in the front swing direction, see Figure 75.

The resulting effect of the pitch offset would be to increase the reference laser dot displacement, which would cause the actuation angle to appear larger than it truly is, see equation (81). This effect on the uncertainty of the determined angular input, was taken into account when determining the uncertainty of the right-angle triangle assumption in section D.1.1.

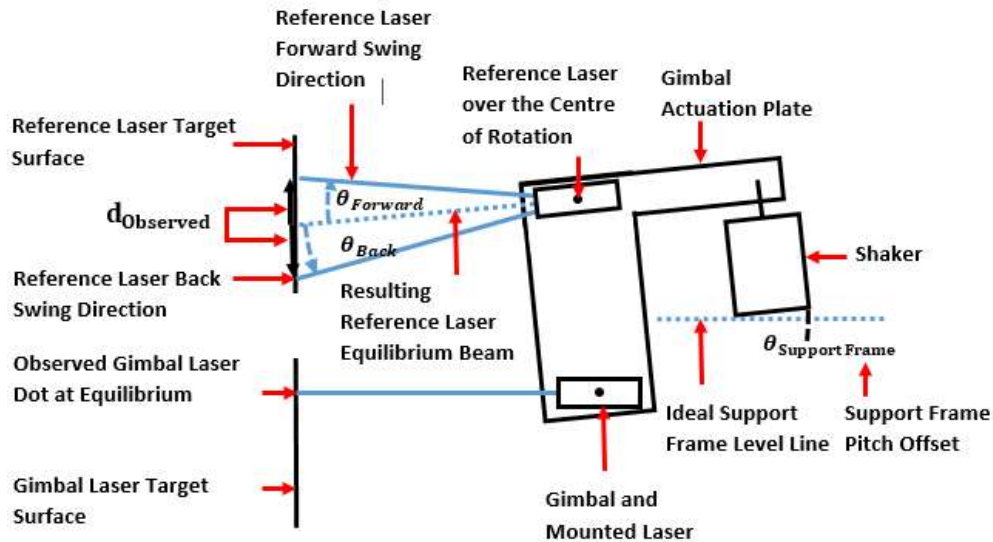


Figure 75. An example of the equilibrium error introduced to the reference laser displacement, if the support frame has a pitch pose error. Note that the rotations are not shown for the expected gimbal responses. The gimbal laser beam shows the gimbal and gimbal laser beam at system equilibrium with the support frame offset.

$$d_{\text{Observed}} = [\tan(\theta_{\text{Support Frame}} + \theta_{\text{Forward}}) - \tan(\theta_{\text{Support Frame}} - \theta_{\text{Back}})] D_{\text{Reference}} \quad (81)$$

An inclinometer, accurate to 0.1° , was used to determine the static pitch of the support frame and actuation plate, with respect to the world co-ordinate system. As the calibration board was also orientated with respect to the world co-ordinate system, the frame and board would theoretically be in alignment. It was recognized, though, that the inclinometer still allowed for, and introduced, an error, which is included in equation (90) which is discussed in Appendix D.1.7.

The inclinometer is a manufactured device, therefore a 95% confidence interval was assumed for the measurement uncertainty and therefore the uncertainty was equal to the systematic uncertainty, see equation (82). In addition to measuring the system's pitch offset, the inclinometer was also used to measure the system's roll offset, therefore both variables were determined using the same device and so these two errors were correlated.

As a result of this, equations (26) and (27) were used to determine the inclinometer systematic uncertainty, see equation (83). As before, the sensitivity indexes of the effecting variables had to be determined, resulting in equations (84) and (85), with the latter being discussed in section D.1.5. The sensitivity indexes were determined by the change in reference laser dot displacement, with respect to the change in frame pose roll and frame pose pitch separately.

$$u_{\text{inclinometer}} = b_{\text{inc.}} \quad (82)$$

$$b_{\text{inc.}} = \sqrt{\left((\theta_{\text{roll}} + \theta_{\text{pitch}}) \cdot 0.05^\circ \right)^2 + 2 (\theta_{\text{roll}} \cdot \theta_{\text{pitch}}) (0.05^\circ)^2} \quad (83)$$

$$\theta_{\text{pitch}} = \frac{\partial \text{Displacement_Difference}_{\text{Reference}}}{\partial \theta_{\text{Frame}}} \quad (84)$$

D.1.5 Support Frame and Actuation Plate Constant Roll Error

Similar to the definition of support frame pitch error, roll offset was considered to be any combination of base plate and frame roll angle that resulted in the reference laser dot displacement to deviate line to deviate from parallel with the z-axis, see Figure 76. Although not a problem on its own, roll error in combination with the pitch errors from section D.1.4, did worsen the effects of the pitch errors.

As discussed in section D.1.4, an inclinometer was used to the static roll of the support frame, with respect to the world co-ordinate system. Unlike the pitch error,

the roll error from the actuation plate would have very little, if any, effect on the reference laser displacements, as was proven in section D.3.

As the calibration board was also orientated with respect to the world co-ordinate system, the frame and board would theoretically be in alignment. It was recognized, though, that the inclinometer still allowed for, and introduced, an error and uncertainty associated with the accuracy of the inclinometer measurements, which is included in equation. GDIML bore sight error was also present.

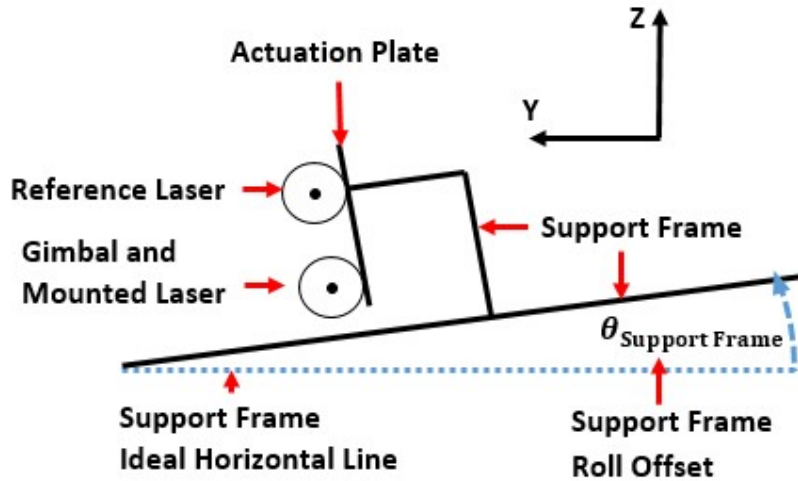


Figure 76. An example of a negative support frame roll offset angle. Note that the viewpoint is from behind the lasers and that the shaker and the target surfaces are not shown.

As a result of the frame roll error only affecting the reference laser dot displacement, when in combination with the pitch errors discussed in section D.1.4, a simplified equation defining how the frame roll angle affected the reference laser dot displacement could not be used.

$$\theta_{\text{roll}} = \frac{\overline{\partial \text{Displacement_Difference}}_{\text{Reference}}}{\partial \phi_{\text{Frame}}} \quad (85)$$

D.1.6 Support Frame Constant Yaw Error and Reference Laser Distance to Target Error

The perpendicularity of the support frame, and therefore the reference laser, to the reference laser target surface was determined through the use of a laser range finder. The range finder was also used in determining the distance of the reference laser to the reference laser target surface. Thus, the yaw and distance-to-target errors were

correlated, so equations (26) and (27) from section 2.8, were used to determine the range finder's correlated systematic error, see equation (87).

Equations (88) and (89) are the sensitivity indexes, see equation (22) in 2.8, of the resulting reference laser dot displacement for the change in reference laser distance to target and change in frame yaw angle, relative to the reference laser target surface respectively. Note, even though two distances were required to determine the yaw angle of the support frame, the second measurement was not independent of the distance to the target and the one side measurement of the support frame to the target surface. Therefore, only two variables were needed in equation (87).

$$u_{\text{Reference_Distance}} = 1.96 b_{r,f} \quad (86)$$

$$b_{r,f} = \sqrt{\left((\theta_{rf,1} + \theta_{rf,2}) \cdot 0.5 \text{ mm} \right)^2 + 2 \cdot (\theta_{rf,1} \theta_{rf,2}) (0.5 \text{ mm})^2} \quad (87)$$

$$\theta_{rf,1} = \frac{\overline{\partial \text{Displacement_Difference}_{\text{Reference}}}}{\partial D_{\text{Reference}}} \quad (88)$$

$$\theta_{rf,2} = \frac{\overline{\partial \text{Displacement_Difference}_{\text{Reference}}}}{\partial d_{\text{wall_left}}} \quad (89)$$

As indicated and discussed in sections D.1.1, D.1.4 and D.1.5, if an error causes the reference laser dot displacement profile to diverge from the ideal displacement profile assumed in 4.2, the determined angular actuation would be negatively affected. Therefore, if the reference laser distance to target is altered, the errors mentioned above will worsen. However, as determined by the Monte Carlo simulations in section D.3, this change in perpendicular distance of the centre line of rotation had to be greater than 9 °.

D.1.7 Actuation Uncertainty Summation

To determine the uncertainty of the determined actuation angle the root sum square method needed to be used, see equation (18), which resulted in equation (90).

$$u_{\text{Actuation}} = \sqrt{\begin{aligned} &u_{\text{Reference_Assumption}}^2 + u_{\text{Reference_Reprojection}}^2 \\ &+ u_{\text{Reference_Camera_Distance}}^2 + u_{\text{Reference_Bore_Sight}}^2 \\ &+ u_{\text{Reference_Inclinometer}}^2 + u_{\text{Reference_Distance}}^2 \\ &+ u_{\text{Reference_Verification}}^2 \end{aligned}} \quad (90)$$

D.2 Gimbal System Error Sources and Resulting Uncertainty Contributions

Four sources of significant error were identified for the gimbal response tracking, see Figure 77.

1. The positioning of the camera for the experiment.
2. The accuracy verification tests.
3. The gimbal laser bore sight error.
4. The synchronization of the reference laser monitoring and gimbal laser monitoring cameras.

Note that the uncertainty introduced by the accuracy tests was discussed in section 4.7 and is therefore not discussed here.

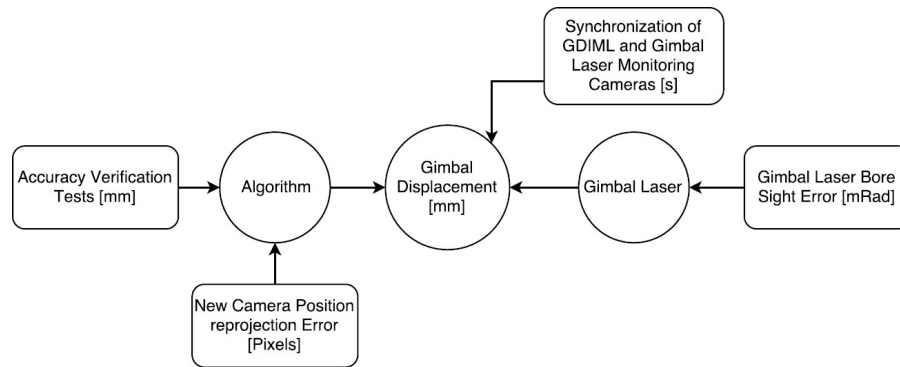


Figure 77. The error flowchart for the gimbal laser. There were four sources of error in the determination of the device mount response.

D.2.1 Displacement Profile Assumption

The uncertainty introduced due to the assumed gimbal laser dot displacement profile was determined through the Monte Carlo simulations, using equation (15). Equation (25)(17) and a required certainty of 95% was used to determine the degrees of freedom of the t-value, which provided the uncertainty bound for equation (91).

It was recognized that the difference between the true response angle and the determined response angle, was a function of the support frame yaw, pitch and roll offsets, the actuation plate yaw, pitch and roll offsets, the device mount yaw, pitch and roll offsets, the gimbal laser distance to target surface and gimbal laser bore sight error. Therefore, the uncertainties associated with these variables would have functional relationships with the difference

Each variable had a specific functional relationship with the assumption performance. Therefore, they were related, implying that equation (24) in section 2.8 needed to be used to determine the random uncertainty. Each variable's errors were randomly chosen, the uncertainty for the assumption was be the result of the standard deviations of the variables, $s_{\bar{x}_i}$ in equation (92), and the functional relationships, see equation (22) in section 2.8, they have with the displacement differences, see equation (93). The sensitivity indexes for each variables were determined by using the average displacement difference and the average value change for each variable in question (Figliola & Beasley, 2011).

$$u_{\text{Response_Assumption}} = 1.96 s_{\overline{\text{Response_Assumption}}} \quad (91)$$

$$s_{\overline{\text{Response_Assumption}}} = \sum_{i=1}^{11} \sqrt{(\theta_{x_i} s_{\bar{x}_i})^2} \quad (92)$$

$$\theta_{x_i} = \frac{\partial \overline{\text{Displacement_Difference}}_{\text{Response}}}{\partial \bar{x}_i} \quad (93)$$

D.2.2 New Camera Position Error

The determination of the uncertainty introduced by the gimbal laser monitoring camera's position uncertainty is the same as the determination of the reference laser monitoring camera's. Therefore the response monitoring camera's uncertainties can be found in equations (94) and (95) below.

$$u_{\text{Response_Reprojection}} = \frac{b_{\text{Response_Reprojection}}}{2} \quad (94)$$

$$u_{\text{Response_Camera_Distance}} = 1.96 b_{\text{Response_Camera_Distance}} \quad (95)$$

D.2.3 Gimbal Laser Bore Sight Error

As mentioned in section D.1.1, the laser bore sight error in this setup only becomes a problem if the laser is rolled. Since the device mount was allowed to respond in roll, the effect that the bore sight error and device mount roll would have on the determined device mount pitch, needed to be determined. As the gimbal laser bore sight error could not be determined, it introduced an uncertainty into the determination of the device mount response.

Figure 78 is an example of the position change of the laser dot that can occur if the gimbal laser is rolled. Note that the axis system shown in the figure is relative to the gimbal laser, the bore sight error is constant and that the example assumes that the ideal gimbal laser beam would shine perpendicular to the target surface.

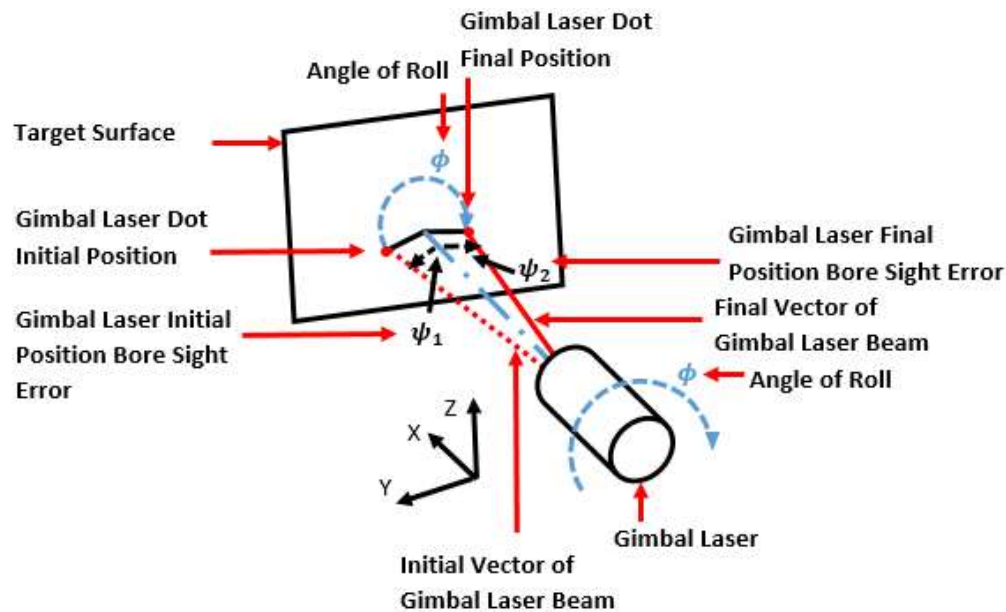


Figure 78. An example of the effect of the gimbal laser bore sight error, in combination with device mount roll. Note that the initial and final bore sight errors are the same, that the co-ordinate system is with respect to the gimbal laser and that this example assumes that the ideal gimbal laser beam would shine perpendicular to the target surface.

The determination of the uncertainty the bore sight error introduces into the determined response is the same as the determination of the uncertainty the reference laser bore sight error in section D.1.3. Therefore, the uncertainty, random error and the sensitivity index used to determine the random error can be found in equations (96), (96) and (98) respectively.

$$u_{\text{Response_Bore_Sight}} = 1.96 s_{\text{Response_Bore_Sight}} \quad (96)$$

$$s_{\text{Response_Bore_Sight}} = \theta_{\text{Disp_BoreSight}} 1 \text{ mRad} \quad (97)$$

$$\theta_{\text{Disp_Bore_Sight}} = \frac{\overline{\partial \text{Displacement_Difference}}}{\partial \psi_{\text{Response_Bore_Sight}}} \quad (98)$$

D.2.4 Camera Synchronization

Although possible to synchronise the two cameras with software developed by iSpeed, it was not possible to obtain the specific software package that would have facilitated this function. Instead, the cameras' triggers were connected to the same external trigger button.

The Olympus high speed cameras have a built in function called Burst Record On Command, BROCC, which is used to record a predetermined number of images after the camera trigger. This feature does not rely on button de-bouncing, but is triggered by the first trigger voltage edge detected. In combination with the high camera processor speed, the time delay between the trigger being received and the first image being stored has been quoted to be in the tens of nanoseconds.

For the highest frame rate of 10 000fps and a large time delay to the first stored image of 100 nanoseconds, the amount of time lost is 0.1% of the period between images being stored (C. Robinson 2017, personal communication, 25th August). Therefore, based on this it was decided that it would be safe to assume that both the cameras started recording at the exact same time and that the cameras started recording the moment a voltage edge, lower than 1.1V, was detected. Therefore, this time difference was small enough to be negligible for the experiments.

D.2.5 Response Uncertainty Summation

To determine the uncertainty of the determined response the root sum square method needed to be used, see equation (18), which resulted in equation (99). Note that the actuation uncertainty also had an effect on the response as both the measurement and actuation errors filtered through to the gimbal actuation and response measurement.

$$u_{\text{Response}} = \sqrt{u_{\text{Response_Assumption}}^2 + u_{\text{Response_Reprojection}}^2 + u_{\text{Response_Camera_Distance}}^2 + u_{\text{Response_Bore_Sight}}^2 + u_{\text{Actuation}}^2} \quad (99)$$

D.3 Monte Carlo Error Simulations Analysis

The Monte Carlo simulations were used to run through all the combinations of actuations, support frame pose errors, actuation plate pose errors, reference laser bore sight errors, device mount responses, device mount errors and gimbal laser bore sight errors.

One of the chief goals of the Monte Carlo simulations was to provide an indication of the effects of the assumed reference laser dot and gimbal laser dot displacement profiles. In addition, the simulations were to help gain insight into how the proposed experiments can be changed to improve accuracy.

A single swing was simulated where the device mount pose, gimbal laser bore sight error, gimbal pose, actuation plate pose, reference laser bore sight error, support frame pose, distance to target error, upswing error, downswing error, gimbal rotation errors, shaker peak-to-peak displacement and shaker stroke variance were randomly selected.

Using linear algebra, the positions of the reference laser and gimbal laser were determined on a target surface for both peak swing positions, relative to the centre of rotation of the reference laser. This was then used to test how well the assumption of the reference laser and gimbal laser displacements would approximate the true input and true gimbal angular error.

The pitching actuations and rolling actuations were simulated, with 10 million iterations for each simulation being executed. The list of the parameter ranges used can be found in Table 9.

The reference laser dot displacement profile assumption, for both the reference and gimbal laser, proved to be more robust than expected, thus validating the use of the reference laser to determine the disturbance input angle.

The results also indicated that determining the disturbance input and gimbal response from the stationary initial conditions was highly sensitive to pose errors, but did not allow for reliable, or accurate, determinations of these pose errors. Determining the disturbance input and gimbal response from the laser dots' peak-to-peak displacement, on the other hand, proved to be more reliable and therefore this method was used to determine the disturbance input and gimbal responses.

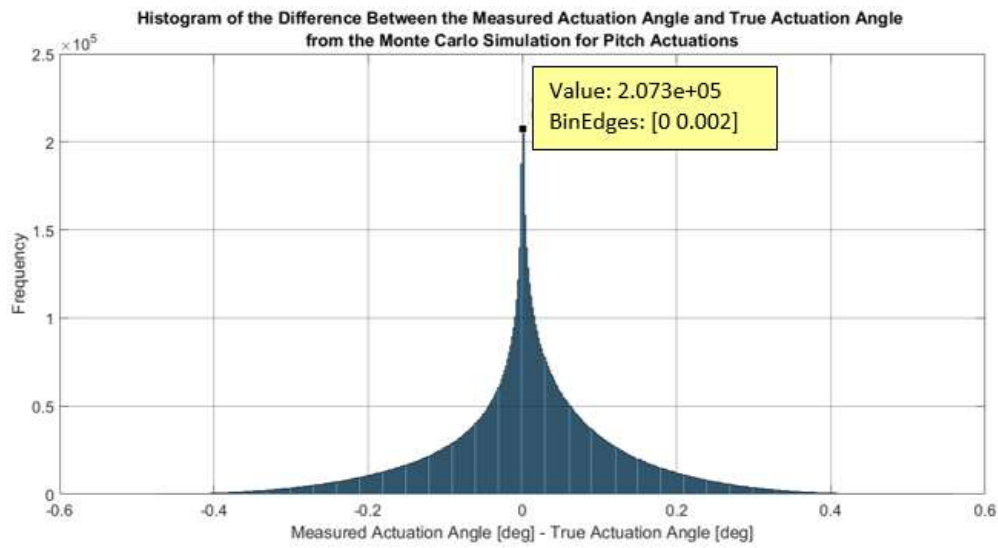


Figure 79. Histogram of the difference between the measured and true actuation angle from the Monte Carlo simulations for pitch actuations. This histogram serves as an indication of how the right-angle triangle assumption performs when assuming the system is operating ideally. It must be stressed that input variables were allowed to range from -10° to 10° , thus indicating a low sensitivity to relatively large variations.

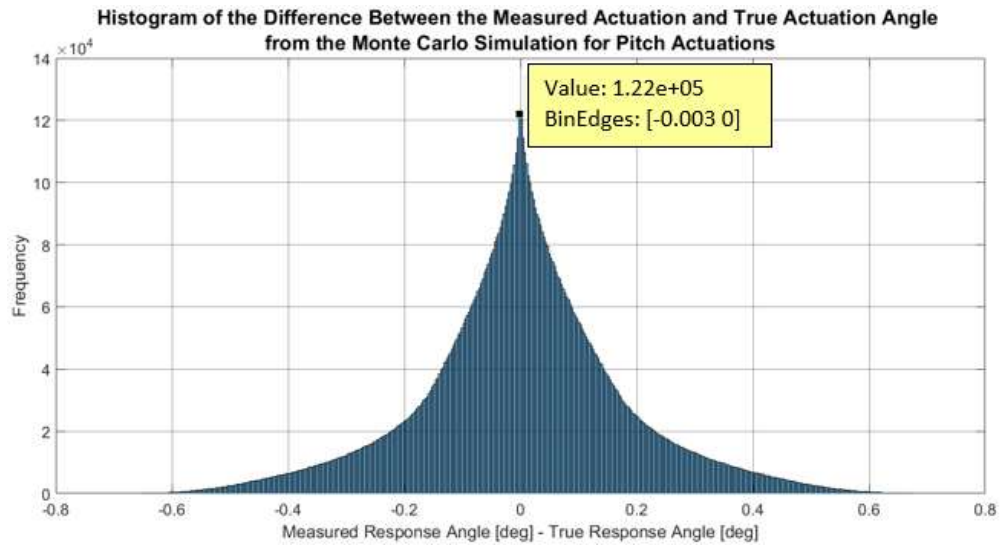


Figure 80. Histogram of the difference between the measured and true gimbal response angle from the Monte Carlo simulations for pitch actuations. This histogram serves as an indication of how the right-angle triangle assumption performs when assuming the system is operating ideally. It must be stressed that the input variables were allowed to range from -10° to 10° , thus indicating a low sensitivity to relatively large variations.

Table 9. Monte Carlo input variable ranges 1

Monte Carlo Random Input Variable Ranges		
Variable	Range Type	Range
Shaker Peak-to-Peak Stroke	Distance [mm]	0.0001 mm – 8 mm
Shaker Up Stroke Deviation	Distance as a fraction of the chosen ideal stroke [mm]	$\pm 1/4$ of Up Stroke
Shaker Down Stroke Deviation	Distance as a fraction of the chosen ideal stroke [mm]	$\pm 1/4$ of Down Stroke
Reference Laser Distance to Target Surface	Distance	± 1 mm
Reference Laser Bore Sight Error Direction	A combination of the yaw, pitch and roll.	1-6
Reference Laser Direction	Random selection from Aircraft Euler angle set	1-6
Support Frame Orientation	Random selection from Aircraft Euler angle set	1-6
Actuation Plate Orientation	Random selection from Aircraft Euler angle set	1-6
Reference Laser Bore Sight Error Direction Angles	Random Range for yaw, pitch and roll in degrees	Iterative combination of yaw, pitch and roll until final angle magnitude = 3 mrad
Reference Laser Direction Angles	Random Range for yaw, pitch and roll in degrees	Iterative combination of yaw, pitch and roll until final angle magnitude = 1 °
Support Frame Orientation Angles	Random Range for yaw, pitch and roll in degrees	± 10 ° Each
Actuation Plate Orientation Angles	Random Range for yaw, pitch and roll in degrees	± 10 ° Each

Table 10. Monte Carlo input variable ranges 2

Monte Carlo Random Input Variable Ranges		
Variable	Range Type	Range
Gimbal Orientation	Random selection from Aircraft Euler angle set	1-6
Gimbal Response Errors	Random Range for yaw, pitch and roll in degrees	$\pm 10^\circ$ Each
Gimbal Laser Bore Sight Error Direction	Random selection from Aircraft Euler angle set	1-6
Gimbal Laser Direction	Random selection from Aircraft Euler angle set	1-6
Gimbal Laser Bore Sight Error Direction Angles	Random Range for yaw, pitch and roll in degrees	Iterative combination of yaw, pitch and roll until final angle magnitude = 2 mrad
Gimbal Laser Direction Angles	Random Range for yaw, pitch and roll in degrees	Iterative combination of yaw, pitch and roll until final angle magnitude = 1°

E. Support Structure Natural Frequency Tests

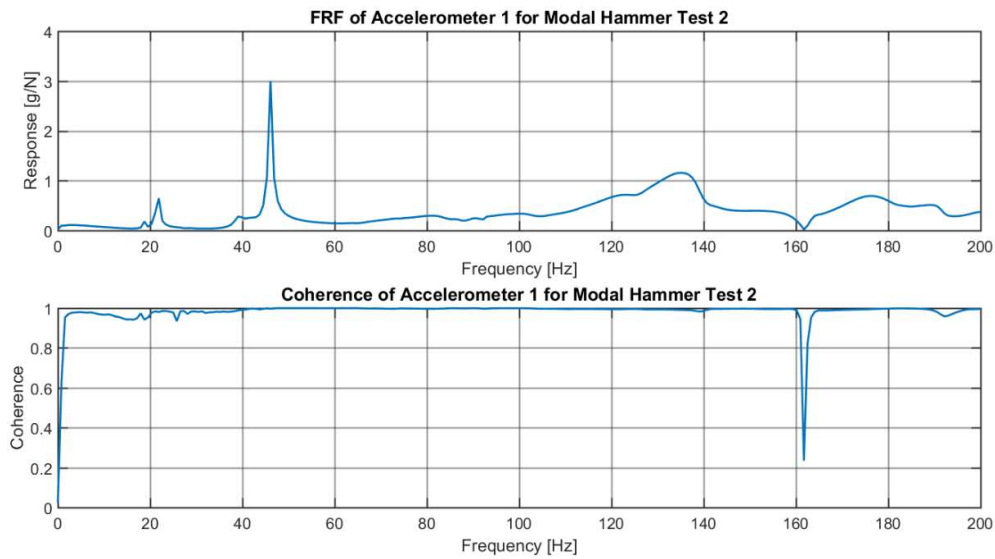


Figure 81. The FRF of the upper beam of the support frame for the second modal hammer test. The actuation plate was hit horizontally, near accelerometer 5 in the horizontal, positive z-axis direction of the mounted accelerometers. Reliable resonances at 18.8 Hz, 21.9 Hz, 46.1 Hz and 135.2 Hz were observed.

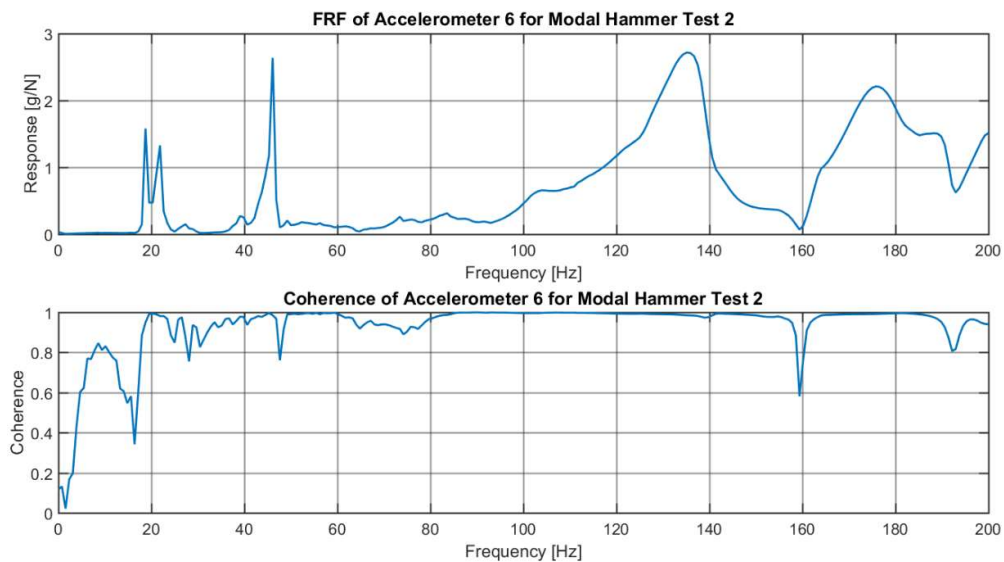


Figure 82. The FRF for the actuation plate for the second modal hammer test. The actuation plate was hit horizontally, near accelerometer 5 in the horizontal, positive z-axis direction of the accelerometers. Resonances were observed at 18.8 Hz, 21.9 Hz, 46.1 Hz, 135.2 Hz and 175.8 Hz.

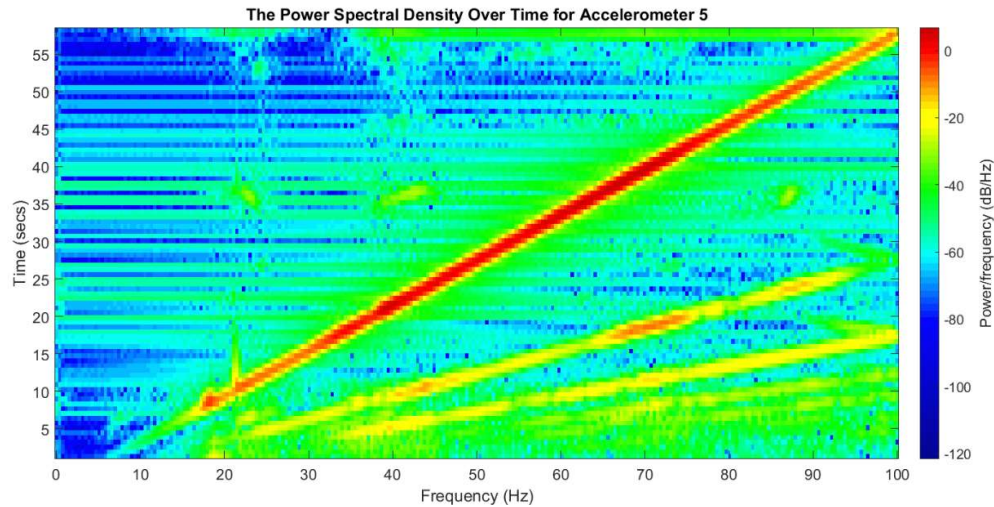


Figure 83. The power spectral density over time for accelerometer 5 on the actuator plate. A 1 Hz to 100 Hz, over 60 seconds, sinusoidal frequency sweep with the main support frame mounted shaker, was used to excite the system. The gimbal was off and taped to prevent any component, or cable, oscillations. The graph shows the range of frequencies that were measured, on the x-axis, for each step in time, the left y-axis. Thus, the figure shows that as the shaker input, the largest diagonal red line, increases with time, certain resonances and their harmonics, the smaller radial lines, are induced in the structure. The figure also shows that a near consistent 20 Hz and 40 Hz component is being measured throughout the sweep.

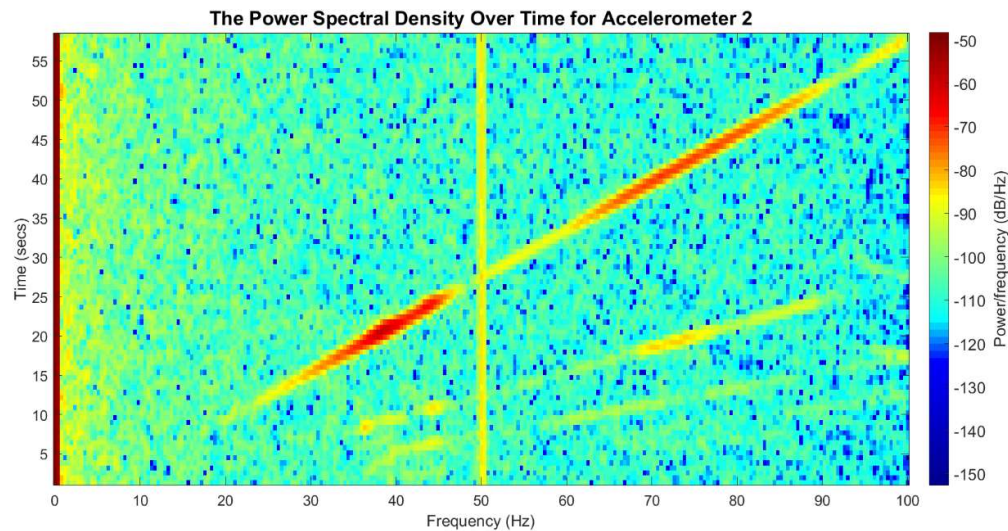


Figure 84. The power spectral density over time for accelerometer 2 on the actuator plate. A 1 Hz to 100 Hz, over 60 seconds, sinusoidal frequency sweep with the main support frame mounted shaker, was used to excite the system. The gimbal was off and taped to prevent any component, or cable, oscillations. The graph shows the range of frequencies that were measured, on the x-axis, for each step in time, the left y-axis. Thus, the figure shows that as the shaker input, the largest diagonal red line, increases with time, certain resonances and their harmonics, the smaller radial lines, are induced in the structure. The figure also shows that a near consistent 20 Hz and 40 Hz component is being measured throughout the sweep.

As seen below, as the gimbal caused the actuation plate to roll and twist in phase, but with differing magnitudes. The displacement of the upper beam of the support frame was also clearly visible.

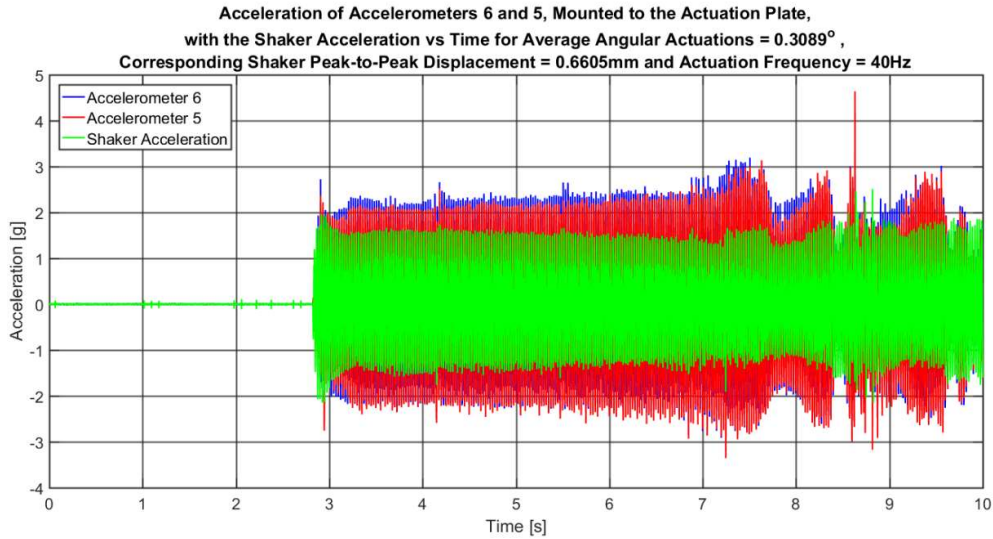


Figure 85. The acceleration vs time plots of accelerometers 4, 5 and 6. Accelerometer 4 was mounted above the shaker, while accelerometers 5 and 6 were mounted at the bottom of the actuation plate, measuring acceleration in the positive y-axis direction of the gimbal. The test was at 40 Hz for the largest shaker displacement amplitude. The magnitude of these accelerations indicate a significant horizontal acceleration and therefore displacement of the actuation plate end taking place.

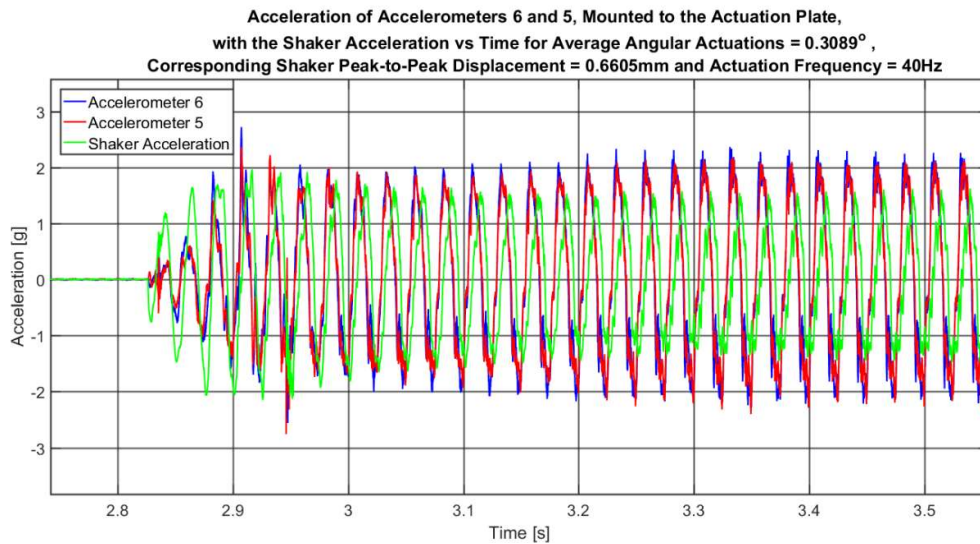


Figure 86. The zoomed acceleration vs time plots of accelerometers 4, 5 and 6. The test was at 40 Hz for the largest shaker displacement amplitude. It is clear from the figure that the accelerations measured at positions 5 and 6 are slightly out of phase, but remain so throughout the test.

F. Gimbal Pitch Response Gain Plots for Pitch Actuations

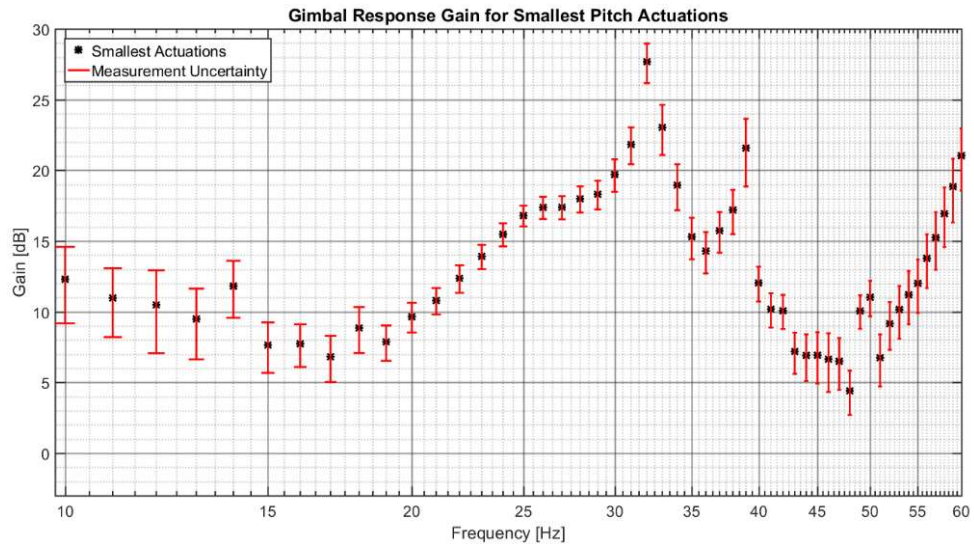


Figure 87. The response gain, with corresponding uncertainties, for the smallest pitch actuations. Large uncertainty bounds indicate small displacements of the gimbal laser dot and reference laser dot. The three different actuations show correlation for the frequency ranges 10 Hz to 31 Hz and 51 Hz to 60 Hz.

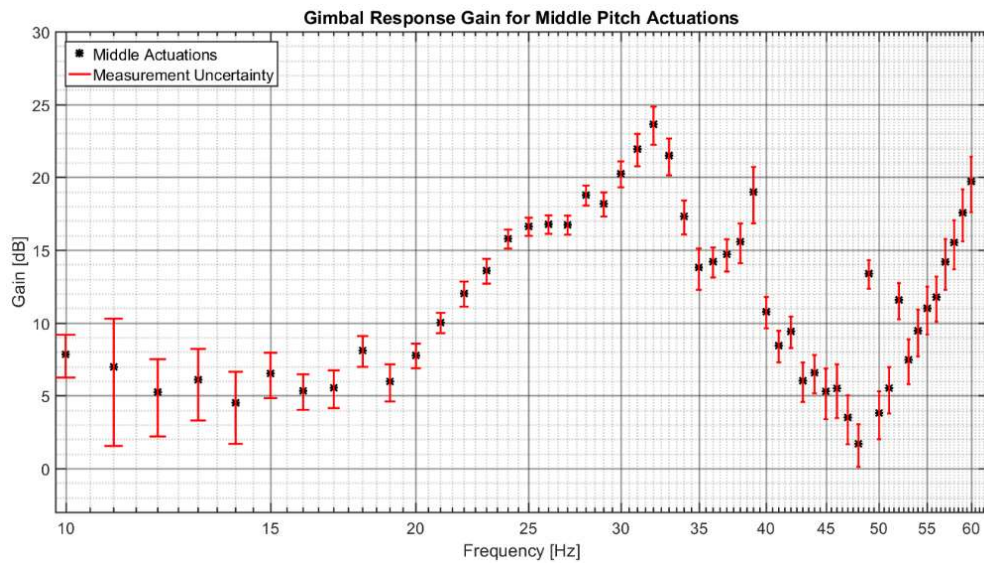


Figure 88. The response gain, with corresponding uncertainties, for the middle pitch actuations. Large uncertainty bounds indicate small displacements of the gimbal laser dot and reference laser dot. The three different actuations show correlation for the frequency ranges 10 Hz to 31 Hz and 51 Hz to 60 Hz.

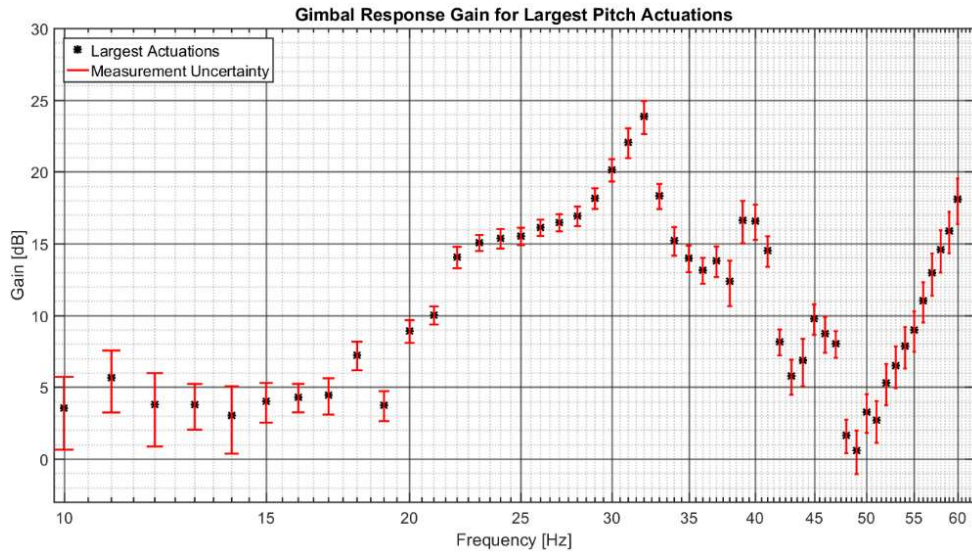


Figure 89. The response gain, with corresponding uncertainties, for the largest pitch actuations. Large uncertainty bounds indicate small displacements of the gimbal laser dot and reference laser dot. The three different actuations show correlation for the frequency ranges 10 Hz to 31 Hz and 51 Hz to 60 Hz.

G. Gimbal Pitch Response Gain Plots for Roll Actuations

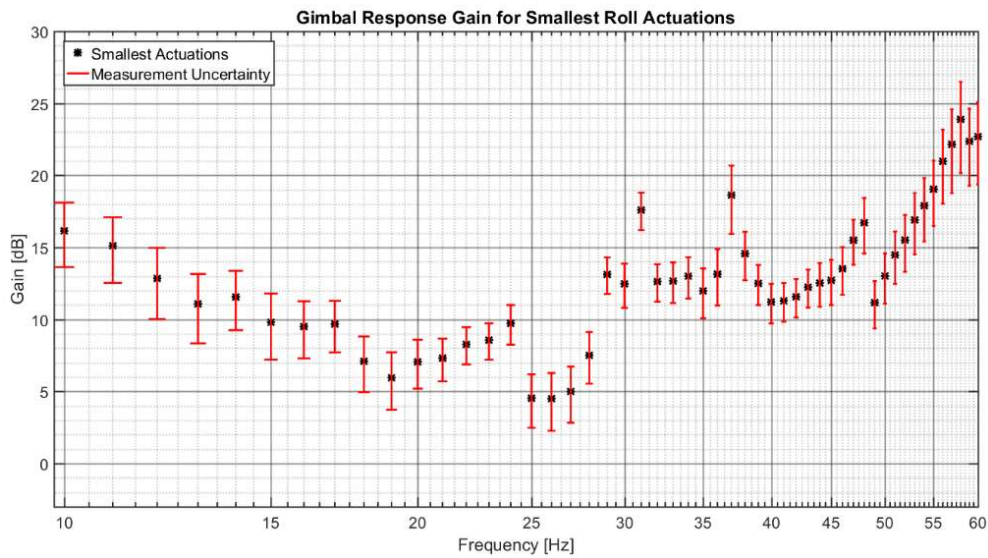


Figure 90. The response gain, with corresponding uncertainties, for the smallest roll actuations. Large uncertainty bounds indicate small displacements of the gimbal laser dot and reference laser dot.

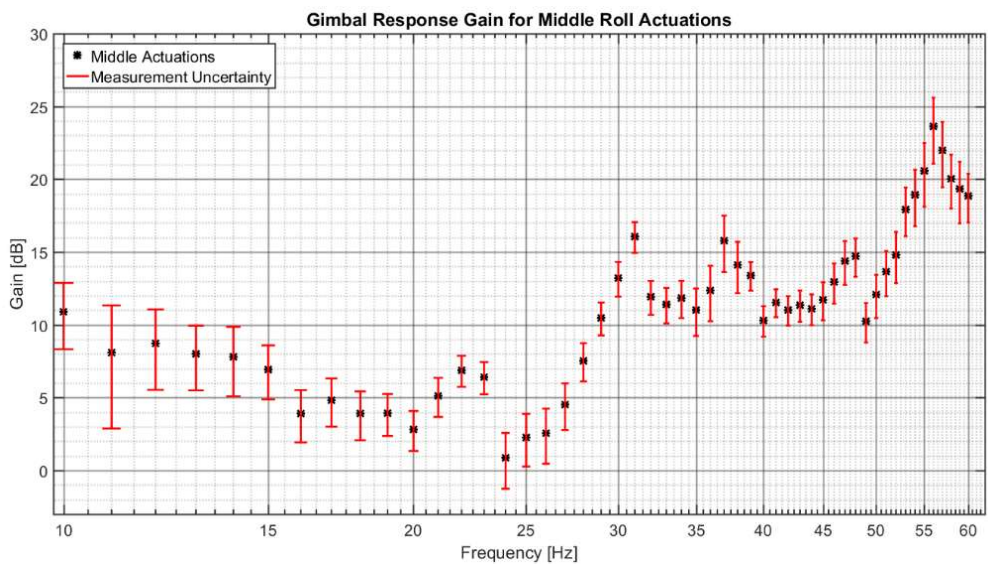


Figure 91. The response gain, with corresponding uncertainties, for the middle roll actuations.

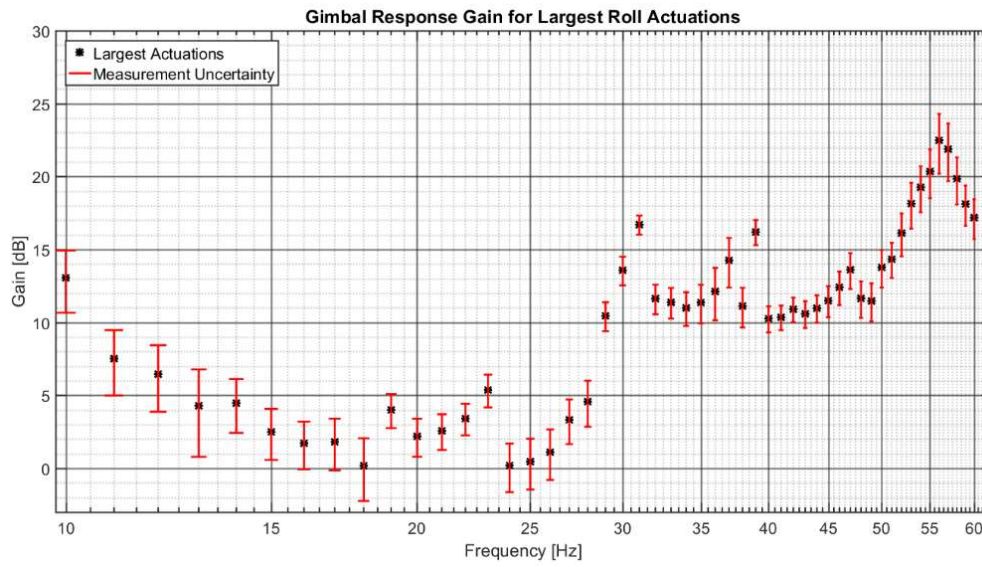


Figure 92. The response gain, with corresponding uncertainties, for the largest roll actuations.

8 References

- Abengoa Solar, 2016. *www.abengoasolar.com*. [Online] Available at: www.abengoasolar.com/export/sites/abengoasolar/pdf/Khi-Solar-One-factsheet.pdf [Accessed 25th July 2018].
- Agilent Technologies, 2000. *The Fundamentals of Signal Analysis Application Note 243*. s.l.:Agilent Technologies.
- Bajd, T., Mihelj, M. & Munih, M., 2013. Chapter 2 - Rotation and Orientation. In: 2nd, ed. *Introduction to Robotics*. s.l.:s.n., p. 83.
- Basecam Electronics, 2017. *SimpleBGC 32bit 3-Axis Software User Manual*. -: BASECAM ELECTRONICS.
- BaseCam, 2014. *BaseCam SimpleBGC 32-bit*. [Online] Available at: <https://www.basecamelectronics.com/simplebgc32bit/> [Accessed 1st March 2016].
- Botha, M., 2017. *Protocol for Multicopter Flight Tests*, Cape Town: The University of Stellenbosch .
- Brown, S. & Vranesic, Z., 2009. *Fundamentals of Digital Logic with VHDL Design*. 3rd ed. New York: McGraw - Hill.
- Bruel & Kjaer, 2014. *Vibration Excitor Type 4809*. s.l.:Bruel & Kjaer Sound and Vibration Measurement A/S.
- Chapman, S. J., 2012. *DC Machinery Fundamentals*. 5th ed. New York: McGraw-Hil.
- Chong, K. K. et al., 2009. Integration of an On-Axis General Sun-Tracking Formula in the Algorithm of Open-Loop Sun-Tracking System. *Sensors*, 9(10), pp. 7849-7865.
- Coetzee, J. S., 2017. *Obstacle Avoidance with a Multicopter in a Dynamic Two-Dimensional Environment*. 1st ed. Cape Town: Stellenbosch University.
- Ellison, S. L. R. & Williams, A., 2012. *EURACHEM / CITAC Guide CG 4 - Quantifying Uncertainty in Analytical Measurement*, s.l.: EURACHEM.
- EMAX, 2018. *EMAX MT3506 KV650 Brushless Mutil-Axis Motor For RC Models - clockwise*. [Online] Available at: https://www.banggood.com/EMAX-MT-3506-KV650-Brushless-Mutil-Axis-Motor-For-RC-Models-p-941144.html?ID=49005&cur_warehouse=CN [Accessed 6th Nov 2018].
- Fedkin, M. & Dutton, J. A., 2012. *Central Tower CSP Technology*. [Online] Available at: <https://www.e-education.psu.edu/eme812/node/649> [Accessed 19th July 2018].

Figliola, R. S. & Beasley, D. E., 2011. *Theory and Design for Mechanical Measurements*. 5th ed. Hoboken: John Wiley & Sons Inc..

Franklin, G. F., Powell, D. J. & Naeni, A. E., 2010. *Feed Control of Dynamic Systems*. 6th ed. s.l.:Prentice Hall.

FSMultirotors, 2014. *DIY AP Quadcopter ~ 8lbs Lift*. [Online] Available at: <https://www.flitetest.com/articles/diy-ap-quadcopter-8lbs-lift> [Accessed 6th July 2018].

Harris, A., Sluss Jr., J. J. & Refai, H. H., 2005. *Alignment and tracking of a free-space optical communications link to a UAV*. Washington, IEEE , pp. 1-9.

Inman, D. J., 2014. *Engineering Vibration*. Fourth ed. s.l.:Pearson Education.

iX Cameras, 2016. *iX Cameras SPECIFICATIONS*. [Online] Available at: <https://www.ix-cameras.com/3-Series/> [Accessed 27 11 2018].

Jia, R. et al., 2017. System Performance of an Inertially Stabilized Gimbal Platform with Friction, Resonance, and Vibration Effects. *Journal of Nonlinear Dynamics*, Volume 2017, p. 20.

Johansson, J., 2012. *Modelling and control of an advanced camera gimbal*. [Online] Available at: www.diva-portal.org/smash/get/diva2:575341/FULLTEXT01.pdf [Accessed 8th November 2016].

Kleyner, A. & O'Connor, P. D. T., 2012. *Practical reliability Engineering*. 5th ed. West Sussex: John Wiley & Sons, LTd.

Laser Components (UK), 2017. *FLEXPOINT Laser Modules LR Series*. Chelmsford Essex: Laser Components.

Lock, J. C., 2016. *Pose Error Estimation of a Quadcopter in the Outdoors*. 1st ed. Cape Town: Stellenbosch University.

LucasVB, 2018. *Gyroscope*. [Online] Available at: <https://en.wikipedia.org/wiki/Gyroscope> [Accessed 11th July 2018].

Mäkilä, P. M., 2006. LTI approximation of nonlinear systems via signal distribution theory. *Automatica*, 42(6), pp. 917-928.

Mathworks, 2014. *undistortImage*. [Online] Available at: <https://www.mathworks.com/help/vision/ref/undistortimage.html> [Accessed 22nd August 2018].

MathWorks, 2016. *What is Camera Calibration?*. [Online] Available at: <https://www.mathworks.com/help/vision/ug/camera-calibration.html> [Accessed 4th July 2016].

MathWorks, 2018. *cameraIntrinsics class*. [Online] Available at: <https://www.mathworks.com/help/vision/ref/cameraintrinsics->

[class.html](#)

[Accessed 7th July 2018].

Minnaar, N. J., 2017. *State Estimation in Unmanned Aerial Vehicles: Theoretical Approaches for Increasing Accuracy*. 1st ed. Cape Town: Stellenbosch University.

National Instruments, 2016. *Understanding FFTs and Windowing*. [Online] Available at: <http://www.ni.com/white-paper/4844/en/> [Accessed 22 October 2018].

Optical Surfaces, 2018. *Highly Stable Gimbal Mirror Mounts*. [Online] Available at: <https://www.optisurf.com/index.php/highly-stable-gimbal-mirror-mounts/> [Accessed 23rd June 2018].

Pintelon, R., Louarroudi, E. & Lataire, J., 2013. Detecting and Quantifying the Nonlinear and Time-Variant Effects in FRF Measurements Using Periodic Excitations. *Transactions on Instrumentation and Measurement*, 62(12), pp. 3361-3373.

Potgieter, F. J., 2016. *Navigational precision of an autonomous ground vehicle using multiple sensors*. 1st ed. Cape Town: Stellenbosch University.

RC Timer, 2017. *IMAGO/GoPro IMP 2Axis Brushless Gimbal All Multi-Rotor*. [Online] Available at: <http://rctimer.com/?product-1076.html> [Accessed 13th November 2018].

Siemens, 2015. *LMS Test.Xpress*. [Online] Available at: www.dta.com.tr/pdf/brosur/siemens_lms/Siemens-PLM-LMS-Test-Xpress_brosur.pdf [Accessed 6th September 2018].

Song, L., Wu, W., Guo, J. & Li, X., 2013. *Research on sub-pixel location of the laser spot center*. Hangzhou, IEEE.

Texas Instruments, 2013. *Engineer It - Understanding basic sensored BLDC motor operation*. [Online] Available at: https://www.youtube.com/watch?v=0mQunSe2_FM [Accessed 11th July 2018].

Thorlabs, 2017. *Position Sensing Detectors*. [Online] Available at: https://www.thorlabs.com/newgrouppage9.cfm?objectgroup_id=4400 [Accessed 14th July 2018].

Van Breda, R. J., 2016. *Vector Field Histogram Star Obstacle Avoidance System for Multicopters*. 1st ed. Cape Town: Stellenbosch University.

